UNIVERSITY OF SOUTHAMPTON

Faculty of Engineering and the Environment
Institute of Sound and Vibration

Aeroacoustics of deep cavity flows

by

You Wei Ho

BEng

ORCiD: 0000-0003-4818-1755

A thesis for the degree of
Doctor of Philosophy

October 2023

University of Southampton

Abstract

Faculty of Engineering and the Environment
Institute of Sound and Vibration

Doctor of Philosophy

Aeroacoustics of deep cavity flows

by You Wei Ho

Flow-acoustic resonances occurring within deep cavities have been observed in various engineering applications. These resonances occur when specific operating conditions cause airflows over deep cavities to excite self-sustained oscillations that couple with least-damped acoustic modes to generate intense aerodynamic noises. Consequently, these flow-acoustic resonances can lead to extreme noise, violent unsteady structural loads and threaten the mechanical integrity of the system. Hence, it is important to understand the underlying physical mechanisms of the aerodynamic noise generation in deep cavity flows. This thesis uses high-resolution large-eddy simulations to investigate the flow-acoustic resonance in turbulent flows passing over deep cavities at low-subsonic flow speeds across three distinct inclination angles. Several theoretical methods, including Doak's momentum potential theory, modal and non-modal analyses, are employed to gain insights into the intricate noise generation and amplification mechanisms within orthogonal and inclined deep cavity flows. Accordingly, the work presented in this thesis is structured into two main parts. The first part of this thesis investigates the flow-acoustic resonance in orthogonal deep cavity flow at three different flow speeds. The subsequent analysis reveals strong evidence of efficient fluid-acoustic coupling between the shear layer oscillations and the nearby depthwise acoustic modes in all cases, and the optimum Mach number at which the pronounced acoustic response occurred is identified. Consequently, an improved frequency prediction model tailored explicitly for orthogonal deep cavity flows at low subsonic flow as a function of inflow boundary-layer property is proposed. The second part of this work investigates the flow-acoustic resonance in inclined and deep cavity flow across three distinct inclination angles. Notably, a marked contrast in aeroacoustic behaviour between inclined and orthogonal cavities is observed at the elevated flow speed, which do not follow the existing flow-acoustic resonance theories. Specifically, inclined cavities display a markedly enhanced resonance with the peak frequency being significantly lower in comparison to the orthogonal cavity configuration. It is postulated that the amplified flow-acoustic resonances in inclined cavities are linked to a low-frequency extension of the first hydrodynamic mode through enhanced shear layer undulations when the acoustic particle displacement is comparable to the momentum thickness. Experimental evidence supports this hypothesis. The elucidation of this hypothesis holds potential in advancing our understanding and mitigation of flow-acoustic resonance in inclined and deep cavity flows.

Contents

List of Figures

List of Tables

Declaration of Authorship

I, You Wei Ho, declare that the thesis entitled *Aeroacoustics of deep cavity flows* and the work presented in the thesis are both my own, and have been generated by me as the result of my own original research.

I confirm that:

1. This work was done wholly or mainly while in candidature for a research degree at this University;
2. Where any part of this thesis has previously been submitted for a degree or any other qualification at this University or any other institution, this has been clearly stated;
3. Where I have consulted the published work of others, this is always clearly attributed;
4. Where I have quoted from the work of others, the source is always given. With the exception of such quotations, this thesis is entirely my own work;
5. I have acknowledged all main sources of help;
6. Where the thesis is based on work done by myself jointly with others, I have made clear exactly what was done by others and what I have contributed myself;
7. Parts of this work have been published or are under review for publication as:

   Y. W. Ho and J. W. Kim. A wall-resolved large-eddy simulation of deep cavity flow in acoustic resonance. *Journal of Fluid Mechanics*, 917, April 2021a

   Y. W. Ho and J. W. Kim. Wall-resolved large-eddy simulations of inclined deep cavity flows in acoustic resonance. In *28th AIAA/CEAS Aeroacoustics Conference*. American Institute of Aeronautics and Astronautics, June 2022

   Y. W. Ho and J. W. Kim. Flow-acoustic resonance in inclined and deep cavities. *Under review in Physical Review Fluids*

Signed:..... Date:.....

Acknowledgements

I would like to express my heartfelt gratitude to Professor Jae Wook Kim, whose unwavering support and invaluable guidance have been instrumental in shaping my academic journey. Without his constant encouragement, I would not have embarked on the challenging path of pursuing a doctoral degree in aeroacoustics, and for this, I am sincerely indebted. The privilege of working under his tutelage has been a source of immense joy and fulfilment during my time in Southampton. I would also like to extend my gratitude to Dr. Long Wu for his insightful discussions and unwavering support throughout my doctoral studies. His contributions have been invaluable in shaping the direction of my research. Furthermore, I thank the anonymous reviewers for their thoughtful feedback, which has contributed to my research in many helpful ways. I would also like to thank Dr. Christoph Richter at Rolls-Royce for his technical comments and suggestions. In addition, I acknowledge the generous financial support in the form of a studentship provided by Rolls-Royce through the Rolls-Royce University Technology Centre (UTC) for Propulsion Systems Noise in the Institute of Sound and Vibration at the University of Southampton. I acknowledge using the IRIDIS-5 High-Performance Computing Facility and associated support services at the University of Southampton in completing my doctoral studies. I appreciate the Engineering and Physical Sciences Research Council (EPSRC) granting the computational time on the UK supercomputing facility ARCHER-2 through the UK Turbulence Consortium (EP/R029326/1). The allocation of these resources has been paramount in conducting the numerical investigations presented in this dissertation. I am sincerely grateful for their support.

To my beloved parents.

Nomenclature

Roman characters	Description
a	Speed of sound
D	Depth of cavity
e	Internal energy
f	Frequency of oscillation
h	Channel half-height
j	Imaginary unit
J	Jacobian
k	Wavenumber
L	Length of cavity opening
M	Mach number
p	Pressure
Pr	Prandtl number
q	Heat
u_x	Streamwise velocity
u_y	Vertical velocity
Q	Q-criterion
r	Euclidean distance
Re	Reynolds number
S	Sponge zone forcing term
St	Strouhal number
t	Time
T	Period
u, v, w	Streamwise, vertical and spanwise velocities
x, y, z	Cartesian coordinates
Greek characters	**Description**
α	Inclination angle of the deep cavity
γ	Ratio of specific heats
χ	Integrated acoustic forcing
δ_{99}	Turbulent boundary layer thickness
Δ	Change in quantity
λ	Wavelength
ν	Dynamic viscosity (sponge zone coefficient)
ρ	Density
ξ, η, ζ	Body fitted coordinates
τ	Dynamic viscosity
Φ	Phase of Fourier Transform
σ	Magnification rate of response-forcing mode
θ	Momentum thickness

ν	Kinematic viscosity
D	Domain size

Superscript and subscript	**Description**
$\overline{(\cdot)}$	Time-averaged mean component
$(\cdot)'$	Fluctuating component
$(\cdot)^+$	Receptivity of perturbation
$(\cdot)^H$	Hermitian transpose
$\hat{(\cdot)}$	Modal perturbation of fluctuating component
$(\cdot)_\infty$	Free-stream quantity
$(\cdot)_A$	Acoustic component
$(\cdot)_c$	Coherent vortex component
$(\cdot)_H$	Hydrodynamic component
$(\cdot)_{x,y,z}$	Streamwise, vertical, spanwise components

Abbreviations	**Description**
ACARE	Advisory Council for Aviation Research in Europe
APE	Acoustic Perturbation Equations
CAA	Computational Aeroacoustics
CFD	Computational Fluid Dynamics
DNS	Direct Numerical Simulation
LES	Large Eddy Simulation
LNSE	Linearised Navier-Stokes Equations
NSE	Navier-Stokes Equations
SPL	Sound Pressure Level
TBL	Turbulent Boundary Layer

Chapter 1

Introduction

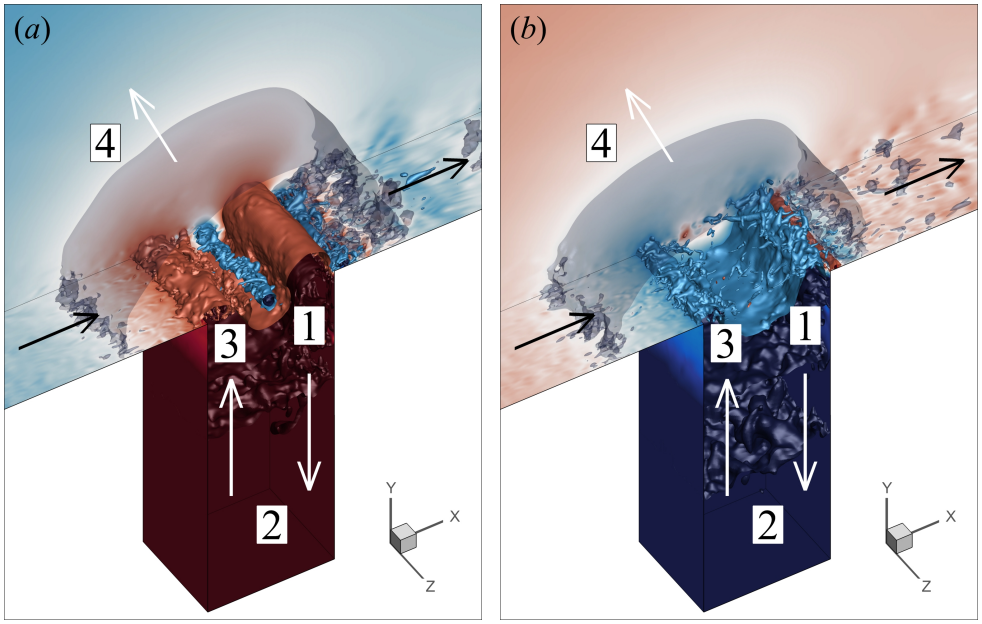

FIGURE 1.1: A simplified deep cavity geometry representing an orthogonal off-take duct with a closed duct valve. The panels (*a*-*b*) show the instant before and after the vortex impingements. The complex aeroacoustic process in deep cavity flows involves the noise generation arises from the vortex impingement on the downstream corner (1), acoustic reflections from the bottom wall (2), the fluid-acoustic coupling mechanisms (3), and the eventual noise propagation to the far-field (4), are visualised through the instantaneous pressure fields. The arrows in black indicate the flow direction from the inlet (left) to the outlet (right), whereas the arrows in white denote the direction of the acoustic propagation into and out of the off-take duct.

1.1 Research motivation

Air transport is one of the safest and fastest-growing modes of transportation worldwide. The UK and Europe have particularly witnessed a significant surge in air traffic in recent years, with the projections estimating an anticipated escalation to 445 million annual airline passengers by 2020 (Department of Transport, 2013). However, this growth has come at the cost of increased noise pollution, particularly around major airports and residential areas. The World Health Organisation (WHO) underscores the seriousness of this environmental concern, estimating that noise pollution could result in approximately 1.6 million DALYs (disability-adjusted life years) across Western Europe (World Health Organization, 2011). These adverse health implications encompass a spectrum of complications, ranging from sleep disorders and tinnitus to more severe conditions such as ischaemic heart diseases and cognitive impairments in children. In the year of 2000, the Advisory Council for Aviation Research and Innovation in Europe (ACARE) was formed. ACARE comprises a group of experts from industry and research institutions, led by Jean-Brice Dumont, EVP Airbus, and Co-Chairs from DLR and KLM. The mission of the council is to address the challenges and opportunities facing the aviation sector in Europe and to promote its sustainable development. Subsequently, ACARE introduced FlightPath 2050, providing a non-binding policy based on widely accepted expert opinion and forecast adopted by policymakers and legislation to guide the industry's efforts towards noise reduction. The policy includes an aspiring target of reducing perceived aircraft noise by 65% compared to the levels observed relative to the year 2000. Consequently, it is assumed that stringent regulations and noise limitations will be enforced in the foreseeable future to minimize noise sources during airplane certification. Therefore, the development of the situation has prompted manufacturers to design turbofan engines capable of operating under quieter conditions to meet the stringent requirements of airplane certification. Thus, the primary aim of mitigating noise generated by turbofan engines becomes of utmost importance and warrants immediate attention within the industry.

One of the primary sources of noise in a turbofan engine is associated with fan (Paruchuri, 2017) and jet noise (Proenca, 2018). These noise sources are considered the leading contributors to the overall turbofan engine noise. In addition to fan and jet noises, another source of concern is tonal noise generated by the off-take duct configuration situated within the bypass duct. The off-take duct plays an important role in redirecting cool air from the bypass duct to regulate the temperature of adjacent engine components. However, under certain operational conditions, particularly when the off-take duct valve temporarily closes in situations where cooling is unnecessary, it transforms into a deep cavity configuration with a substantial depth-to-length ratio (e.g., $D/L \gg 1$). In this specific operating state, the viscous turbulent flow passing over the cavity opening excites a self-sustained shear layer oscillation and coupled with the nearby least-damped acoustic mode of the deep cavity. This aeroacoustic oscillation leads to the generation of intense acoustic pressure fluctuations and is depicted schematically in figure 1.1. Consequently, aeroacoustic fluctuations from multiple off-take ducts can significantly contribute to the total noise level of the turbofan engine and can pose substantial risks to the structural integrity of nearby engine components. However, addressing the noise issue in this seemingly simplistic cavity configuration proves inherently challenging due to the intricate aeroacoustic phenomena involved in deep cavity flows. These complexities serve as the primary motivation for this research. Thus, this thesis aims to investigate the underlying physical mechanisms responsible for noise generation and amplification in inclined and deep cavity flows.

1.2 Aeroacoustics of deep cavity flows

Aeroacoustics is a branch of acoustics in the subject of fluid dynamics that studies noise generation and radiation resulting from either turbulent fluid motions or aerodynamic forces interacting with solid surfaces. In recent decades, there has been extensive research into the mechanisms behind sound generation in turbulent fluid flows, with the consensus being that the presence of unsteady fluid motions inevitably leads to sound production (Lighthill, 1952). Subsequently, several acoustic analogies have been proposed to take into account of sound generation by turbulent flows in the presence of solid surfaces (Curle, 1955; Williams and Hawkings, 1969). Despite recent progress in understanding the fundamental principles of sound generation, the intricate nature of fluid-acoustic interactions continues to present challenges in accurately predicting sound sources. These challenges arise from the fact that seemingly simple flow configurations can exhibit complex fluid flow characteristics, eluding straightforward analysis and prediction. A notable example of a seemingly simple flow configuration that can exhibit such complexities in flow behaviours is found in cavity flows. It is the central focus of this present thesis.

The investigation of cavity flows is a fundamental problem in aeroacoustics that has attracted significant scientific interest because it involves the self-sustained oscillation of shear layer instabilities through distinct feedback mechanisms. Previous studies have comprehensively reviewed the existing body of literature on cavity flows (Rockwell and Naudascher, 1978; Gloerfelt, 2009; Tonon et al., 2011; Morris, 2011). Essentially, self-sustained oscillation can be classified by the type of feedback that occurs into three main categories. The first classification pertains to an incompressible cavity flow with a feedback mechanism that is purely hydrodynamic in nature such that the pressure fluctuations induced from the downstream corner of the cavity travel upstream at an infinite speed via pseudo-sound. The second classification deals with the flow of a compressible fluid over a shallow cavity through Rossiter's feedback mechanism (Rossiter, 1964). At higher flow speeds or in deeper cavities, the acoustic perturbation generated by this feedback mechanism can further excite an acoustic mode of the cavity, leading to self-sustained resonances. Hence, a better understanding of these distinct flow types is essential for gaining insights into the underlying physical phenomena.

Self-sustained oscillations resulting from compressible cavity flows generate significant noise pollution and unwanted vibrations, leading to fatigue failures (Ziada and Lafon, 2014). These phenomena have been extensively studied over several decades and are classified as "fluid-resonant oscillations" by Rockwell and Naudascher (1978). Generally, this type of self-sustained oscillation can be further classified into two groups: self-sustained resonance in shallow cavities (Rowley et al., 2002) and those occurring in deep cavities (Tonon et al., 2011). In the case of shallow cavities, the self-sustained oscillations are governed by the horizontal feedback mechanism described by Rossiter (1964) and are particularly prominent in aeronautic applications involving high subsonic grazing flows. Specifically, the feedback process begins with small-amplitude Kelvin-Helmholtz instabilities in the shear layer impinging at the downstream edge of the cavity and generating acoustic waves that travel upstream and further excite instabilities in the shear layer. Consequently, this feedback loop results in vortex shedding near the upstream corner at the characteristic frequency predicted by Rossiter (1964). In contrast, deep cavities exhibit a completely different mechanism, where aeroacoustic instabilities couple with depthwise acoustic modes to excite self-sustained resonances at low subsonic grazing flows.

Particularly, these self-sustained resonances stemming from aeroacoustic instabilities in deep cavity flows generate high-intensity pressure waves with discrete frequencies, resulting in detrimental effects such as noise pollution and structural fatigue in various engineering applications, including safety valves (Coffman and Bernstein, 1980; Galbally et al., 2015), closed side-branches in gas transport systems (Bruggeman et al., 1989; Ziada, 2010), turbo-machineries (Ziada et al., 2002; Aleksentsev et al., 2016), and riverine environments (Perrot-Minot et al., 2020). These oscillations emerge as a consequence of the intricate feedback mechanism between the hydrodynamic and resonant acoustic fields (Peters, 1993a). Of particular significance is the role played by the acoustic resonance as the primary upstream feedback mechanism for amplifying the system oscillations and inducing flow tone lock-ins (Yang et al., 2009). In turn, the stronger acoustic field organizes and modulates the shear layer separation and impingement. Therefore, the shear layer oscillations and the acoustic mode occur at the same frequency in a lock-in state over a range of flow velocities. As mentioned, this phenomenon distinguishes itself from shallow cavity oscillations, where the commonly assumed Rossiter feedback mechanism primarily enables the upstream acoustic feedback (Rossiter, 1964; Rowley and Williams, 2006).

The aeroacoustics of deep cavity flows have received considerable attention in scientific literature. Studies such as that by (Karamcheti, 1955; Plumblee et al., 1962; Rossiter, 1964; East, 1966) have offered substantial evidence of generating pronounced acoustic responses near depthwise acoustic modes inherent to these flows. This "fluid resonant oscillation" emerges from the interaction between the excitation of the shear layer oscillation and the reinforcement provided by the acoustic resonance. To elucidate the underpinnings of this process, it begins with initial shear layer instabilities near the upstream separation corner giving rise to the generation of acoustic standing waves within the cavity upon interaction with the downstream corner. The ensuing resonant acoustic field induces velocity perturbations, which, in turn, amplify the instabilities within the shear layer, thus closing the feedback loop. In particular, this feedback loop proves consequential in deep cavity systems due to their susceptibility to depthwise acoustic modes that exhibit minimal radiation losses (Koch, 2005; Duan et al., 2007; Tinar and Rockwell, 2014b). As a result, the induced velocity perturbations by the resonance may further intensify the shear layer instabilities, ultimately leading to the formation of highly coherent vortex structures in deep cavity flows as documented by Tam (1978); Tonon et al. (2011); Ziada and Lafon (2014); Tinar and Rockwell (2014a).

The acoustic modes in deep cavity flows can be separated into two distinct categories: the nearly-trapped (localised) modes (Koch, 2005) and the non-trapped (global) modes (Duan et al., 2007; Hein and Koch, 2008). As mentioned, these depthwise acoustic modes in deep cavities play a crucial role in reinforcing the shear layer instabilities and can be further assumed as nearly trapped or localised acoustic modes (Tonon et al., 2011). This assumption is primarily based on the observation that the predominant acoustic energy generated by the aeroacoustic oscillation accumulates in the form of a depthwise standing wave in the interior of the cavity, unaffected by boundary conditions beyond the cavity, thereby displaying negligible radiation losses. Consequently, the nearly-trapped mode generates a maximum acoustic velocity at the branch opening, which maximises the acoustic power production of the convecting vortices in a direction normal to the acoustic velocity oscillation, according to Howe's energy corollary (Howe, 2002). Therefore, these unique features of minimised radiation losses and efficient sound power production render deep cavity systems highly susceptible to flow-acoustic resonances. Conventionally, in quiescent flow, the frequency and mode shape of acoustic resonances are determined by computing the eigenmodes of the Helmholtz equation. However, recent numerical investigations have uncovered evidence indicating a notable influence of mean flow on the nearly-trapped mode in shallow cavities (Aly and Ziada, 2012). Consequently, whether the effect of mean flow on acoustic resonances observed in shallow cavity configurations applies to deep cavity configurations remains an open area for further exploration.

Typically, self-sustained resonances in deep cavities existed within distinct ranges of the Strouhal number, each relating to various hydrodynamic modes of the flow field. These unique hydrodynamic modes are characterised by the number of convecting vortex structures across the cavity opening that satisfy the requisite streamwise phase criterion (Rowley et al., 2002; Tuna and Rockwell, 2014; Ho and Kim, 2021b). It is commonly observed that self-sustained resonances, triggered by the first hydrodynamic mode, lead to pronounced acoustic responses at a Strouhal number around $St \approx 0.4$ (Tonon et al., 2011). In addition, weaker self-sustained resonances can be excited by higher hydrodynamic modes (Yang et al., 2009), at Strouhal numbers exceeding $St \approx 0.8$ (Tonon et al., 2011). Presently, it remains unclear why the sound source is most effective when operating at the first hydrodynamic mode.

Recent studies on closed side branches have identified an additional oscillation mode at a lower Strouhal number of $St \approx 0.27$. This oscillation mode is associated with the magnitude of acoustic responses exceeding the dynamic pressure of the flow (Peters, 1993a; Ziada, 1994; Dequand et al., 2003; Bravo et al., 2005; Yang et al., 2009). Within this flow regime, the resonant acoustic field wields substantial influence over the coherence and trajectory of the resulting vortex structure (Bruggeman, 1987; Kriesels et al., 1995; Dequand et al., 2003). As a result of these complex dynamics, the amplification of instabilities and shear layer oscillations transition into highly non-linear states, posing substantial challenges in accurately describing the fluid resonant mechanism (Peters, 1993a). It is worth mentioning that Rowley et al. (2002) reported an oscillation of the wake mode which bears a striking resemblance to the oscillation observed in deeper cavities that exhibit higher levels of acoustic forcing (Kriesels et al., 1995), despite the author opposing conclusion that the wake mode exists purely hydrodynamic in nature.

Bruggeman (1987) observed a similar aeroacoustic behaviour from flow-induced oscillations in closed side branches and suggested that it may depend on the ratio of the acoustic particle velocity associated with the depthwise standing-wave to the mean flow velocity. He proposed three different levels of acoustic pulsation, with each level describing an increase in the influence of the acoustic resonance on the receptivity of the separated shear layer near the upstream corner. The level of pulsation is expressed by the ratio of $|u_a|/U_b$, where $|u_a|$ is the amplitude of the acoustic particle velocity at the cavity opening, and U_b is the centerline velocity in the main channel. At low pulsation levels (e.g. $|u_a|/U_b \leqslant O(10^{-3})$), the acoustic perturbation is insufficient to trigger the formation of coherent vortices from the separated shear layer near the upstream corner. Consequently, the streamwise growth of the hydrodynamic perturbation in the shear layer can be described by the linearised theory of an inviscid quasi-parallel free shear layer (Michalke, 1972). At higher pulsation levels (e.g. $|u_a|/U_b \geqslant O(10^{-1})$), the shear layer undergoes roll-up into discrete vortices, and the amplitude of oscillations is determined by the non-linearities (Peters, 1993b).

Bruggeman et al. (1989) proposed an alternative feedback mechanism for the fluid-resonant oscillation based on Vortex Sound Theory (Howe, 2003). This mechanism involves the following process: acoustic forcing from the resonance on the shear layer at the upstream corner; formation of coherent vortices due to instabilities in the separated shear layer; transfer of energy from the local flow to the acoustic field through the interaction of convective vorticity and the acoustic resonance; and net energy transfer to the acoustic field determining the amplitude and phase of the feedback at the upstream corner. Based on this concept, the acoustic resonance in the deep cavity is crucial in destabilizing the shear layer and reinforcing the vortex coalescences. Therefore, this alternative feedback mechanism, based on the energy transfer between the vortical (hydrodynamic) and potential (acoustic) fields, offers an attractive explanation for the ”lock-on” effect observed in deep cavity experiments (East, 1966; Yang et al., 2009).

Recently, modal analysis techniques, such as global linear stability analyses, have gained prominence as valuable tools for studying asymptotic long-time flow instabilities and gaining insight into the underlying mechanisms of instability in fluid-flow systems (Theofilis, 2011; Schmid and Brandt, 2014). Specifically, direct global modes resulting from this approach have proven particularly effective in exploring the three-dimensional instability observed in both shallow cavity flows (Theofilis, 2000; Bres and Colonius, 2008; Yamouni et al., 2013b; Meseguer-Garrido et al., 2014; Citro et al., 2015; Liu et al., 2016; Sun et al., 2017) and deep cavity flows (Boujo et al., 2018). Furthermore, the combination of direct global modes and adjoint eigenvectors has proved valuable in identifying the structural sensitivity and locating the origin of instability, also known as "wavemaker" regions, within the flow (Chomaz, 2005; Giannetti and Luchini, 2007; Schmid and Brandt, 2014). Understanding these regions may be useful for understanding the underlying physical mechanisms of self-sustained resonance in deep cavity flows. In addition, non-modal analyses, such as resolvent analyses (Trefethen et al., 1993) based around turbulent mean flows (McKeon and Sharma, 2010) have become an essential approach for investigating the optimum forcing, response and their associated amplification in shallow cavity flows (Sun et al., 2017; Liu et al., 2021) and deep cavity flows (Boujo et al., 2018). However, there remains to be a notable gap in the literature concerning its use as an acoustic input-output analysis based on the linear operator of acoustic perturbation equations (APEs) to investigate acoustic energy amplification from harmonic forcing, such as Lamb vectors, to the harmonic acoustic response. This presents a promising and unexplored area for research that warrants further investigation and exploration.

To date, the majority of existing experimental studies have focused on the canonical problem of a single deep cavity or a similar configuration such as those found in closed side branches within piping systems (Ziada and Shine, 1999b; Forestier et al., 2003; Oshkai et al., 2005, 2008; Hassan et al., 2007; Yang et al., 2009; Velikorodny et al., 2010; Ziada and Lafon, 2014; Wang et al., 2018; Bourquard et al., 2021; Hanna and Mohany, 2023). Concurrently, numerical investigations in this domain have been actively pursued (Larchevêque et al., 2003; Thornber and Drikakis, 2008; Salt et al., 2014; Sampath and Sinhamahapatra, 2016; Chen and Adams, 2017; Pedergnana et al., 2021). However, it is important to emphasis that the existing numerical investigation on deep cavity flows with a fully turbulent inflow condition remains limited. Furthermore, despite significant progress in understanding the aeroacoustics of deep cavity flows, most of the existing investigations thus far have primarily focused on orthogonal cavity geometries. Consequently, our understanding of the corresponding noise generation and feedback mechanisms inherent to inclined and deep cavities remains limited. Thus, it is important to conduct further studies utilising high-fidelity numerical simulations to bridge these knowledge gaps.

1.3 Research aims and objectives

Flow-acoustic resonance arising from turbulent flow passing through deep cavities are recognized as a result of the interplay between hydrodynamic instabilities and the least-damped acoustic modes of the deep cavities. However, the current understanding of the noise generation and feedback mechanisms inherent to inclined and deep cavity turbulent flows still needs to be improved. As a result, the primary aim of this thesis will address the existing gaps as highlighted in the literature. Accordingly, this dissertation is structured around five main research objectives:

1. Investigate the nose generation and fluid-acoustic coupling mechanisms of self-sustained resonances in orthogonal and inclined deep cavity flows.
2. Investigate the effect of flow speed on the excited acoustic and hydrodynamics modes in orthogonal and inclined deep cavity flows.
3. Explore the noise amplification mechanism in orthogonal and inclined deep cavity flows using acoustic input-output analysis.
4. Identify the stability, receptivity and sensitivity of the orthogonal and inclined deep cavity systems.
5. Propose cost-effective frequency prediction for self-sustained resonance in inclined and deep cavity flows.

1.4 Original contributions

This works investigates the aeroacoustics of orthogonal and inclined deep cavity flows grazed by fully turbulent boundary layer generated from precursor simulations using wall-resolved high-fidelity computational aeroacoustics (CAA) approach based on full 3-D compressible Navier-Stokes equations. In addition, several postprocessing techniques including Doak's momentum potential theory, biglobal linear stability, receptivity and sensitivity analyses, and acoustic input-output analysis are utilised to accomplish the aforementioned research aims and objectives.

1.5 Thesis Outline

The work of this dissertation has yielded two journal papers and one conference paper, one of which is still under review. Therefore, this document will primarily follow the chronological order of these works. Chapter 2 introduces the numerical methods and postprocessing techniques employed. Chapter 3 investigate the self-sustained resonance in an orthogonal and deep cavity at three different flow speeds. Chapter 4, investigate the effect of inclination angles on the aeroacoustics of deep cavity flows. Lastly, Chapter 5 summarizes the main findings of this thesis and presents several avenues for extending this work.

Chapter 2

Computational Methodology

This chapter introduces numerical methods employed to solve the three-dimensional compressible Navier-Stokes equations. Furthermore, postprocessing techniques including linear stability analysis based on linearised Navier-Stokes equations and acoustic intput-output analysis based on acoustic perturbation equations are introduced in this chapter. The primary focus of the present work involves utilizing the complete 3-D compressible Navier-Stokes equations, which incorporate a source term for sponge layers and are expressed in a conservative form, subsequently transformed onto a generalised coordinate system. To establish a nondimensional framework, the governing equations are normalized based on freestream parameters. The nondimensionalisation approach facilitate the subsequent analysis without relying on specific unit systems.

2.1 Governing equations and numerical methods

This thesis employs in-house codes for performing large eddy simulation (LES) based on high-order accurate compact finite difference schemes. Notably, these schemes have been previously utilised to provide high-fidelity numerical investigations, as documented in Pérez-Torró and Kim (2017); Turner and Kim (2017, 2019); Gelot and Kim (2020); Turner and Kim (2020); Degregori and Kim (2021); Ho and Kim (2021b); Castro et al. (2021). In this work, the full 3-D compressible Navier-Stokes equations (with a source term for sponge layers included) are used, which can be expressed in a conservative form, transformed onto a generalised coordinate system as:

$$\frac{\partial}{\partial t}\left(\frac{Q}{J}\right)+\frac{\partial}{\partial \xi_i}\left(\frac{E_j-Re_\infty^{-1}M_\infty F_j}{J}\frac{\partial \xi_i}{\partial x_j}\right)=-\frac{a_\infty}{L}\frac{S}{J}, \tag{2.1}$$

where the indices $i=1,2,3$ and $j=1,2,3$ denote the three dimensions. The vectors of the conservative variables, inviscid and viscous fluxes, are given by:

$$\left.\begin{aligned} Q&=[\rho,\rho u,\rho v,\rho w,\rho e_\mathrm{t}]^T,\\ E_j&=[\rho u_j,(\rho u u_j+\delta_{1j}p),(\rho v u_j+\delta_{2j}p),(\rho w u_j+\delta_{3j}p),(\rho e_\mathrm{t}+p)u_j]^T,\\ F_j&=[0,\tau_{1j},\tau_{2j},\tau_{3j},u_i\tau_{ji}+q_j]^T, \end{aligned}\right\} \tag{2.2}$$

with the stress tensor and heat flux vector written as:

$$\tau_{ij}=\mu\left(\frac{\partial u_i}{\partial x_j}+\frac{\partial u_j}{\partial x_i}-\frac{2}{3}\delta_{ij}\frac{\partial u_i}{\partial x_i}\right),\quad q_j=\frac{\mu}{(\gamma-1)Pr}\frac{\partial T}{\partial x_j}, \tag{2.3}$$

where $\xi_i=\{\xi,\eta,\zeta\}$ are the generalised coordinates, $x_j=\{x,y,z\}$ are the Cartesian coordinates, δ_{ij} is the Kronecker delta, $u_j=\{u,v,w\}$, $e_\mathrm{t}=p/[(\gamma-1)\rho]+u_ju_j/2$ and $\gamma=1.4$ for air. The

local dynamic viscosity μ is calculated by using Sutherland's law (White, 1991). In the current set-up, ξ, η and ζ are aligned in the streamwise, vertical and spanwise directions, respectively. The Jacobian determinant of the coordinate transformation (from Cartesian to the generalised) is given by $J^{-1} = |\partial(x,y,z)/\partial(\xi,\eta,\zeta)|$ (Kim and Morris, 2002). The extra source term S on the right-hand side of (2.1) is non-zero within the sponge layer only, which is described in Kim et al. (2010a,b). In this paper, the freestream Mach and Reynolds numbers are defined as $M_\infty = U_\infty/a_\infty$ and $Re_\infty = \rho_\infty U_\infty L/\mu_\infty$ where $a_\infty = \sqrt{\gamma p_\infty/\rho_\infty}$ is the ambient speed of sound and $U_\infty = \sqrt{u_\infty^2 + v_\infty^2 + w_\infty^2}$ is the speed of the freestream mean flow. The governing equations are non-dimensionalised based on the streamwise cavity opening length $L = 38$ mm for length scales, the ambient speed of sound a_∞ for velocities, L/a_∞ for time scales and $\rho_\infty a_\infty^2$ for pressure, unless otherwise notified. Temperature, density and dynamic viscosity are normalised by their respective ambient values: T_∞, ρ_∞ and μ_∞.

The governing equations given above are solved by using high-order accurate numerical methods specifically developed for aeroacoustic simulation on structured grids. The flux derivatives in space are calculated based on fourth-order pentadiagonal compact finite difference schemes with seven-point stencils Kim (2007). Explicit time advancing of the numerical solution is carried out by using the classical fourth-order Runge-Kutta scheme with the CFL number of 0.95. Numerical stability is maintained by implementing sixth-order pentadiagonal compact filters for which the cutoff wavenumber (normalised by the grid spacing) is set to 0.85π. In addition to the sponge layers used, characteristics-based non-reflecting boundary conditions based on Kim and Lee (2000) are applied at the inflow and outflow boundaries to prevent any outgoing waves from returning to the computational domain. Periodic conditions are used across the spanwise boundary planes unless otherwise stated. Slip (no penetration) and no-slip wall boundary conditions based on Kim and Lee (2004) are applied at the top and bottom channel walls respectively. The computation is parallelised via domain decomposition and message passing interface (MPI) approaches. The compact finite difference schemes and filters used are implicit in space due to the inversion of pentadiagonal matrices involved, which requires a precise and efficient technique for the parallelisation to avoid numerical artefacts that may appear at the subdomain boundaries. A recent parallelisation approach based on quasi-disjoint matrix systems (Kim, 2013) offering super-linear scalability is used in the present paper. For further elaboration and complete algorithmic details of the in-house codes, readers are referred to Turner (2019). To maintain brevity in this theis, these details will not be reiterated here.

2.2 Doak's Momentum Potential Theory

The pressure fluctuations around the cavity can be characterised into two main regions: local hydrodynamic fluctuation near the cavity opening; and acoustic fluctuation around the cavity. Therefore, it is essential to decompose these pressure fields into the hydrodynamic and acoustic components to facilitate the investigations. To achieve this, we employ the momentum potential theory (MPT) developed by Doak (1989). Specifically in Doak's MPT, the momentum-density, ρu is separated into rotational and irrotational components through a Helmholtz decomposition. The Helmholtz decomposition of ρu may be written as:

$$\rho u = B - \nabla\psi, \quad \nabla \cdot B = 0, \tag{2.4}$$

where B and $\nabla\psi$ are the solenoidal and irrotational components of ρu, respectively. Substituting (2.4) into the continuity equation yields a Poisson equation for the irrotational component, with

a source term dependent on density fluctuations,

$$\nabla^2\psi = \frac{\partial\rho}{\partial t}. \tag{2.5}$$

For a single phase continuum fluid, ψ is separated into acoustic component (irrotational and isentropic, denoted ψ_A) and entropic component (irrotational and isobaric, ψ_E) components, governed by the exact equations:

$$\psi = \psi_A + \psi_E, \quad \nabla^2\psi_A = \frac{1}{c^2}\frac{\partial\rho}{\partial t}, \quad \nabla^2\psi_E = \frac{\partial\rho}{\partial E}\frac{\partial E}{\partial t}. \tag{2.6}$$

Considering the low Mach number in this study, the entropy (thermal) contribution is assumed to be relatively small compared to the acoustic contribution, and therefore ψ_E is not included in the subsequent calculation. Then, the momentum equation in terms of the hydrodynamic and acoustic components is obtained by substituting (2.4) into the momentum equation, expressed as:

$$\frac{\partial}{\partial t}(B-\nabla\psi) + \nabla\cdot\left[\frac{(B-\nabla\psi)(B-\nabla\psi)}{\rho} - \tau_{ij}\right] + \nabla p = 0. \tag{2.7}$$

By taking the divergence of (4.2), the Poisson equation for the hydrodynamic pressure fluctuation, p'_H:

$$\nabla^2 p'_H = S_H + \tilde{S_H}, \tag{2.8}$$

and the Poisson equation for the acoustic pressure fluctuation, p'_A:

$$\nabla^2 p'_A = S_A + \tilde{S_A}, \tag{2.9}$$

are derived. Accordingly, the hydrodynamic and acoustic pressure fluctuations are obtained by solving the Poisson equations in (4.3) and (4.4), respectively. The numerical implementation is described extensively in Unnikrishnan and Gaitonde (2016) and the evaluations of the linear (S_H and S_A) and the non-linear source terms ($\tilde{S_H}$ and $\tilde{S_A}$) are detailed in Unnikrishnan and Gaitonde (2020), which are not repeated here for brevity.

2.3 Biglobal linear stability and sensitivity analyses

Linear stability analysis is performed with respect to a turbulent mean flow field to uncover the compressible global instabilities of the asymptotic time evolution of a given infinitesimal perturbation. Firstly, the instantaneous conservative variables are represented by the column vector, $\mathbf{Q} = [\rho, \rho u, \rho v, \rho w, \rho e_t]^T$, and are separated using Reynolds decomposition into turbulent mean state $\overline{\mathbf{Q}}(x,y)$ and perturbation $\mathbf{Q}'(x,y,z,t)$ as:

$$Q(x,y,z,t) = \overline{Q}(x,y) + Q'(x,y,z,t). \tag{2.10}$$

In the present work, the turbulent mean state, $\overline{\mathbf{Q}}$ are obtained by temporal averaging time solutions from the 3-D LES. By substituting (2.10) into the Navier-Stokes equations (2.1) and the equation of state, the governing equations are linearised about the mean state and only the linear terms of $\mathbf{Q}'$ were retained, which yielded the following set of linearised compressible Navier-Stokes equations:

$$\frac{\partial}{\partial t}\left(\frac{Q'}{J}\right) + \frac{\partial}{\partial\xi_i}\left(\frac{E'_j - Re_\infty^{-1}M_\infty F'_j}{J}\frac{\partial\xi_i}{\partial x_j}\right) = -\frac{a_\infty}{L}\frac{S'}{J}, \tag{2.11}$$

along with the linearised equation of state:

$$p' = \frac{\rho'\bar{T} + \bar{\rho}T'}{\gamma}. \tag{2.12}$$

The transformation of the linearised Navier-Stokes equations in (2.11) to a generalised eigenvalue problem is achieved by introducing the modal perturbation of the form, such as:

$$Q'(x,y,z,t) = \hat{Q}(x,y)\exp i(\beta z - \omega t) + \text{complex conjugate}. \tag{2.13}$$

The possibility of performing this transformation is granted by the time-invariant characteristics of the linear dynamical system being examined. Thus, the modal perturbation leads to a generalised direct eigenvalue problem represented by:

$$L(\bar{Q};\beta)\hat{Q} = \omega A\hat{Q}. \tag{2.14}$$

Here, $\omega = \omega_r + \omega_i$ represents a complex eigenvalue, with the real part of the eigenvalue, ω_r, determines the stationary or oscillatory characteristics, while the imaginary part indicates either instability growth ($\omega_i > 0$) or decay ($\omega_i < 0$), at the spanwise wave-number specified by β. Accordingly, the respective instability mode shape is recovered from the complex eigenvectors, expressed as $\hat{Q}(x,y) = \hat{Q}_r(x,y) + i\hat{Q}_i(x,y)$. In the discrete adjoint framework, the adjoint eigenmode can be derived from the conjugate transpose of the generalised eigenvalue problem as denoted in (2.14), represented as:

$$L^+(\bar{Q};\beta)\hat{Q}^+ = \omega^* A^+\hat{Q}^+. \tag{2.15}$$

The resulting adjoint eigenvector, denoted as $\hat{Q}^+$, provides valuable information about the receptivity region of the field quantities, as discussed extensively in the works of Schmid (2007); Luchini and Bottaro (2014). Additionally, the structural sensitivity of the eigenvalues, often referred to as the "wave-maker" region, can be determined by examining the spatially dependent product of direct and adjoint modes, as described by Giannetti and Luchini (2007):

$$S = \frac{\delta\omega}{\delta L} = \frac{(\hat{Q}^+)^H(\hat{Q})}{(\hat{Q}^+)^H A(\hat{Q})}, \tag{2.16}$$

where δL represents a perturbation introduced by additional feedback between the direct variables present in the linearised Navier-Stokes equations. Thus, the structural sensitivity, S, locate the region within the flow where a localised feedback results in the most significant drift in the eigenvalue. In the paper, non-slip and non-penetrating boundary conditions (e.g., zero velocity perturbation and wall-normal pressure gradient) are enforced along the viscous and slip wall boundary conditions (e.g., zero wall-normal velocity perturbation) in the case of a slip wall. Furthermore, non-reflecting characteristic boundary conditions based on Thompson (1987, 1990) and damping sponge regions are used in combination to minimise artificial numerical reflections. In addition, the isothermal condition is preserved for all wall boundaries. The approximation of spatial derivatives was achieved using a standard second-order finite difference scheme. The eigenvalues and eigenvectors of the linear operator were retrieved via the Krylov-Schur algorithm (Stewart, 2002). All eigenmodes presented in this paper achieved convergence within a tolerance level of $||\omega A\hat{Q} - L\hat{Q}|| \leq O(10^{-14})$.

2.4 Acoustic input-output analysis

Recently, acoustic perturbation equations (APEs) proposed by Ewert and Schröder (2003) have demonstrated their efficacy as a hybrid approach for predicting acoustic propagation within cavity flows. This hybrid approach is achieved by utilising acoustic sources directly obtained from the fluid simulations, as documented in recent studies conducted by Aly and Ziada (2012); Arya and De (2021). In the scope of this research, we employed APEs as a linear operator to probe the acoustic input-output behaviour of cavity systems based around on the time-averaged mean flow states. In particular, we incorporated the "APE-4 formulation" into our analysis, which is expressed as follows:

$$\frac{\partial p'}{\partial t} + \bar{c}^2 \cdot \left(\bar{\rho}\hat{u} + \bar{u}\frac{\hat{p}}{\bar{c}^2} \right) = \bar{c}^2 q_c, \tag{2.17}$$

$$\frac{\partial u'}{\partial t} + \nabla\left(\bar{u}\cdot\hat{u}\right) + \nabla\left(\frac{\hat{p}}{\bar{\rho}}\right) = q_m, \tag{2.18}$$

where the noise sources are given by:

$$q_c = -\nabla\cdot\left(\rho' u'\right)' + \frac{\bar{\rho}}{C_p}\frac{Ds'}{Dt}, \tag{2.19}$$

$$q_m = -\left(\omega\times u\right)' + T'\nabla\hat{s} - s'\nabla\hat{T} - \left(\nabla\frac{u'^2}{2}\right)' + \left(\frac{\nabla\cdot\hat{\tau}}{\rho}\right)'. \tag{2.20}$$

The variables marked with a prime symbol denote fluctuating quantities, whereas those with an overbar represent time-averaged values. Among the source terms, those encapsulating two primed quantities are generally smaller than their counterparts and consequently, their contribution to the overall sources is considered negligible and thus omitted. In addition, considering the high Reynolds number and relatively low Mach number flow discussed in this paper, the contributions of viscosity and entropy to the sources are ignored. Consequently, the Lamb vector, defined as $(\omega\times u)'$, is considered as the dominant source term. Applying these simplifications, equations (2.17) and (2.18) are rewritten into a compact form, such as:

$$\frac{\partial q'}{\partial t} = L(\bar{q}) + f', \tag{2.21}$$

where $L(\bar{q})$ denotes the linear operator about the mean flow state $\bar{q} = [\bar{p}, \bar{u}, \bar{v}, \bar{w}]^T$ and f' represents the forcing input comprised of the Lamb vector. Similarly, modal perturbation (2.13) is imposed to (2.21) to form an acoustic input–output dynamics such as:

$$\hat{q}_\omega = [-i\omega I - L(\bar{q})]^{-1}\hat{f}_\omega = R(\bar{q};\omega)\hat{f}_\omega. \tag{2.22}$$

Specifically, the input-output operator $R(\bar{q};\omega)$ relates the input forcing, $\hat{f}_\omega$, to the output fields as acoustic quantities, $\hat{q}_\omega$, in the frequency space. Accordingly, the discretised input-output operator is solved using singular value decomposition to determine the directions that span the forcing input and the state output vectors, such as:

$$R_{\bar{q},\omega} = U\Sigma V^*, \tag{2.23}$$

where $U = [\hat{U}_1, \hat{U}_2, \hat{U}_3, \dots]$ and $V = [\hat{V}_1, \hat{V}_2, \hat{V}_3, \dots]$ give the leading optimum sets of response and the corresponding forcing mode vectors. The amplification gains of the leading optimum

sets are determined by the corresponding singular values $\Sigma = \mathrm{diag}(\sigma_1, \sigma_2, \sigma_3, \dots)$ that are arranged in descending order. Accordingly, the superscript in (2.23) indicates the Hermitian transpose. Assuming deep cavity oscillations can be characterised by the first leading singular value, which is plausible due to the presence of predominantly acoustic resonance, as demonstrated later in the sections, then the leading optimum forcing-response set is sufficient to describes the location of optimum forcing and the resultant acoustic response. Understanding of the result is immensely useful in gaining insights of the noise generation mechanism in deep cavity flows and subsequently, the application in flow controls. These finding will be discussed in detail. Similarly, the analysis of acoustic modes in inclined and deep cavities, which may be influenced by the mean flow field, is achieved by assuming modal perturbation (2.13), presented in the homogeneous form of (2.22):

$$-i\omega\hat{\rho} + \bar{c}^2 \cdot \left(\bar{\rho}\hat{u} + \bar{u}\frac{\hat{\rho}}{\bar{c}^2}\right) = 0, \tag{2.24}$$

$$-i\omega\hat{u} + \nabla(\bar{u}\cdot\hat{u}) + \nabla\left(\frac{\hat{\rho}}{\bar{\rho}}\right) = 0, \tag{2.25}$$

which can be rewritten in the form of a generalised eigenvalue problem to be solved by using the same procedures outlined in subsection 2.3. Within this context, the real part of each complex eigenvalue indicates the physical frequency, while its imaginary counterpart determines the degree of radiation loss associated with the acoustic mode.

2.5 Definition of variables for statistical analysis

Data processing and analysis are performed upon the completion of the simulation. The main property required in this study is the power spectral density (PSD) function of the pressure fluctuations around the cavity. To facilitate the following discussions, we defined the pressure fluctuations here as:

$$p'(x,t) = p(x,t) - \overline{p}(x), \tag{2.26}$$

where $\overline{p}(x)$ is the time-averaged pressure field. Following the definitions used in Goldstein (1976), the PSD functions of the pressure fluctuations (based on frequency and one-sided) are then calculated by:

$$S_{pp}(x,f) = \lim_{T\to\infty} \frac{\hat{p}(x,f,T)\hat{p}^*(x,f,T)}{T}, \tag{2.27}$$

where $\hat{p}$ is an approximate Fourier transform of p, respectively, based on the following definition:

$$\hat{p}(x,f,T) = \int_{-T}^{T} p'(x,t)e^{-2\pi i f t}\,\mathrm{d}t, \tag{2.28}$$

and, '$*$' denotes a complex conjugate. Similarly, the magnitude and the respective phase of the single-sided Fourier transform pressure field are calculated by

$$|p(x,f,T)| = 2\sqrt{\hat{p}(x,f,T)\hat{p}^*(x,f,T)}, \tag{2.29}$$

$$\Phi_p(x,f,T) = \arctan\left\{\frac{\mathrm{Im}[\hat{p}(x,f,T)]}{\mathrm{Re}[\hat{p}(x,f,T)]}\right\}. \tag{2.30}$$

In the above equations, T represents the half-length of the time signals used for the approximate Fourier transform. The same procedures and notation are used for other field quantities later in this paper.

2.6 Description of problem and the computational set-up

The present thesis investigates orthogonal and inclined deep cavity sections enclosed within a channel with a fixed channel height of $2h$. The deep cavity under investigation has a constant length of $L/h = 0.608$ and a constant depth of $D/h = 1.6$. Additionally, three different inclination angles are considered. The study further examines three distinct Mach numbers, namely $M_\infty = (0.1, 0.2, 0.3)$, and corresponding Reynolds numbers based on the cavity opening length of $L = 0.038$ m. The Reynolds numbers are set to $Re_\infty = (87,297,174,594,261,891)$. For this thesis, the Mach numbers are calculated based on the ambient speed of sound ($a_\infty = 340.2$ m/s) and the reference temperature ($T_\infty = 288$ K) for air. Accordingly, separate precursor channel simulations are conducted to generate the necessary turbulent inflow data for the subsequent cavity simulations at the three different Mach numbers considered in this study.

2.7 Simulation set-up and discretisation of the problem

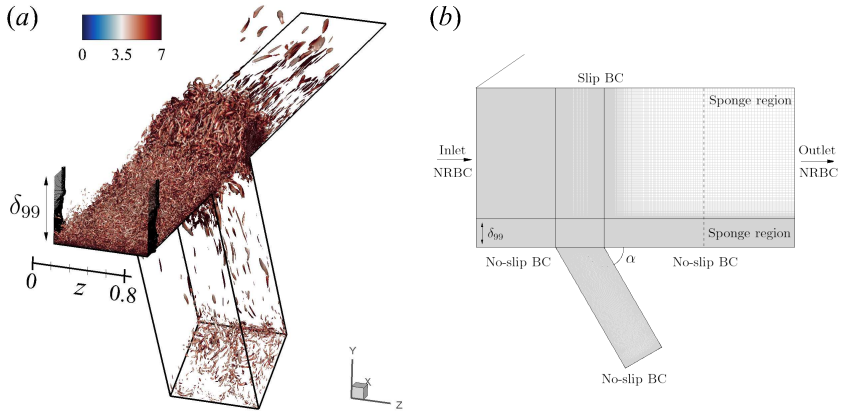

FIGURE 2.1: Visualisations of the current computational domain of the inclined and deep cavity configuration enclosed in a channel. Plotted here are: (a) the instantaneous non-dimensional Q-criterion iso-surfaces ($Q = 5$) coloured by the non-dimensional vorticity magnitude ($|\omega_i|$), showing the three-dimensional vortices in the turbulent boundary layer; and, (b) a spanwise view of the computational domain used in the current numerical investigation.

The inclined and deep cavity geometry and the computational domain used in this work are shown in figure 2.1. The domain of investigation is composed of $x/L \in [-1.64, 4.93]$ in the streamwise direction, $y/L \in [-2.63, 3.29]$ in the vertical direction and $z/L \in [0, 0.822]$ in the spanwise direction. The entire computational domain, the inner region (physical domain) where meaningful simulation data are obtained, and the sponge layer zone are defined as:

$$\left.\begin{aligned} \mathscr{D}_\infty &= \{x \,|\, x/L \in [-1.644, 4.934], y/L \in [-2.632, 3.289], z/L \in [0, 0.822]\}, \\ \mathscr{D}_{\text{physical}} &= \{x \,|\, x/L \in [-1.644, 3.289], y/L \in [-2.632, 3.289], z/L \in [0, 0.822]\}, \\ \mathscr{D}_{\text{sponge}} &= \mathscr{D}_\infty - \mathscr{D}_{\text{physical}}. \end{aligned}\right\} \tag{2.31}$$

The physical domain $\mathscr{D}_\infty$ consists of an inclined and deep cavity with an aspect ratio of $D/L = 2.632$ enclosed in a straight rectangular channel with a channel half-height of $h/L = 1.644$. The inlet is located at $x/L = -1.664$ upstream of the cavity, where the turbulent inflow data is injected. The outflow boundary is placed at a relatively remote location downstream from the cavity, which allows a sufficient distance for the vortices to dissipate. In the current study, a precursor simulation is employed to generate the prerequisite turbulent inflow data for the cavity

simulation. For $M_\infty = 0.1$ and $M_\infty = 0.2$, the precursor simulation domain size ($L_x \times L_y \times L_z$) was set to $4\delta_{99} \times 1\delta_{99} \times 2\delta_{99}$ with $360 \times 120 \times 180$ grid points in the streamwise, vertical and spanwise directions, respectively. For $M_\infty = 0.3$, the precursor simulation domain size ($L_x \times L_y \times L_z$) was set to $4\delta_{99} \times 1\delta_{99} \times 2\delta_{99}$ with $480 \times 240 \times 480$ grid points in the streamwise, vertical and spanwise directions, respectively. The initial boundary layer thickness δ_{99} was determined analytically based on Na and Lu (1973), and the channel flow was initialised with the turbulent mean flow profile according to Spalding (1961). Periodic boundary conditions were applied in the streamwise and spanwise directions, and an implicit pressure gradient was applied to maintain the desired mass flow rate. The precursor simulation was completed when the mean flow profile was converged, and the obtained instantaneous flow solutions were injected into the cavity simulation through the inlet plane. Figure 2.2, figure 2.3, and figure 2.4 shows a close agreement of the time-averaged turbulent velocity profile and the Reynolds stresses between the current half-channel LES and the full-channel DNS results conducted from $Re_\tau \approx 1600$ to $Re_\tau \approx 3900$. The turbulent inflow information for the current cavity simulation is listed in table 2.1.

Re_∞	Re_τ	M_∞	δ_{99}/L	δ^*/L	θ/L	H
87,297	≈ 1600	0.1	0.451	0.0462	0.0367	1.26
174,594	≈ 2600	0.2	0.429	0.0431	0.0345	1.25
261,891	≈ 3900	0.3	0.388	0.0370	0.0300	1.23

TABLE 2.1: Boundary layer parameters for current inclined and deep cavity simulations.

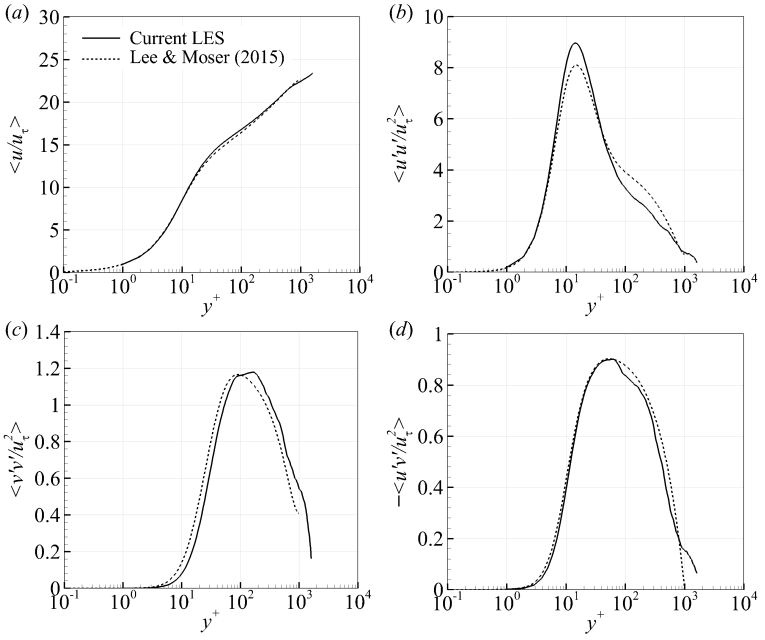

FIGURE 2.2: (*a*) Time-averaged turbulent boundary layer profile; and, (*b*, *c*, *d*) Reynolds stresses obtained from the current precursor half-channel LES ($Re_\tau \approx 1600$) compared to the full-channel DNS ($Re_\tau \approx 1000$) by Lee and Moser (2015).

For $M_\infty = 0.1$ and $M_\infty = 0.2$, the channel region is discretised by $720 \times 270 \times 180$ grid points in the streamwise, vertical and spanwise directions, respectively. A total of $180 \times 180 \times 180$ grid points are used in the streamwise, vertical and spanwise directions, respectively, in the cavity region. Finally, for the $M_\infty = 0.3$ case, the channel region was discretised with a total

of $960 \times 350 \times 480$ grid points in the streamwise, vertical, and spanwise directions. Within the cavity region, $240 \times 240 \times 480$ grid points were employed in the streamwise, vertical, and spanwise directions. In all cases considered here, the mesh in the wall-normal direction is refined close to the viscous wall $y^+ \approx 1$ to ensure a sufficiently high level of near-wall grid resolution is maintained throughout the viscous wall surfaces.

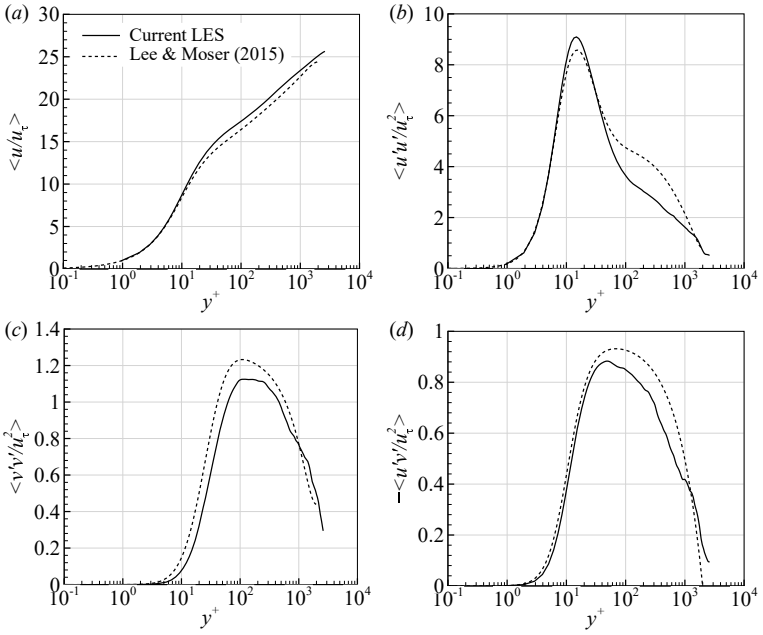

FIGURE 2.3: (*a*) Time-averaged turbulent boundary layer profile; and, (*b*, *c*, *d*) Reynolds stresses obtained from the current precursor half-channel LES ($Re_\tau \approx 2600$) compared to the full-channel DNS ($Re_\tau \approx 2000$) by Lee and Moser (2015).

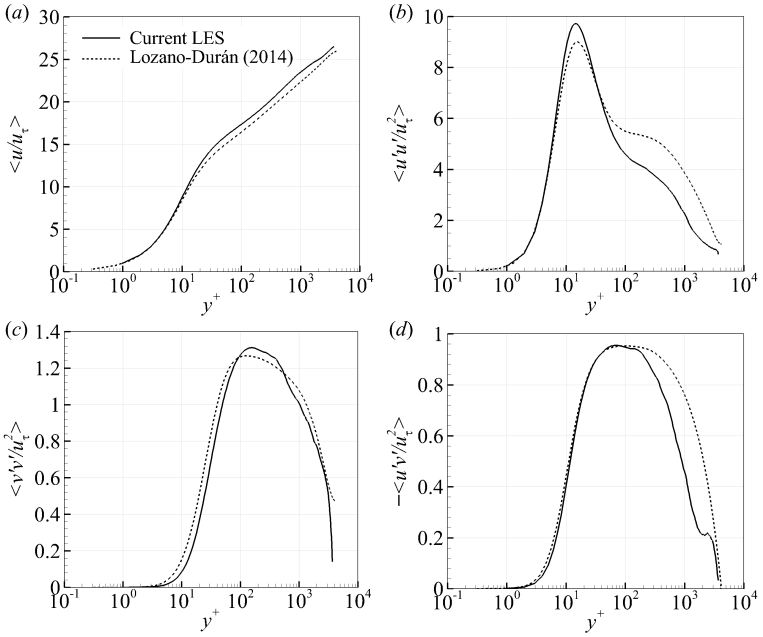

FIGURE 2.4: (*a*) Time-averaged velocity profile of the turbulent boundary layer; and (*b–d*) Reynolds stresses obtained from the current precursor half-channel LES ($Re_\tau \approx 3900$), compared with the full-channel DNS ($Re_\tau \approx 4200$) by Lozano-Durán and Jiménez (2014)

.

Chapter 3

The noise generation mechanisms of orthogonal and deep cavity flows

The aeroacoustic source mechanism of an orthogonal and deep cavity, which has an aspect ratio of $D/L = 2.632$ and is subjected to a turbulent boundary layer of $\theta/L = 0.0345$ at a Mach number of 0.2, is investigated by using a high-order accurate large-eddy simulation. The primary aim of this study is to provide an improved understanding of the fluid–acoustic coupling mechanism that triggers a self-sustained acoustic resonance in a deep cavity. Various analysis methods, which include Doak's momentum potential theory that allows for the separation of hydrodynamic and acoustic components, are used to provide highly detailed investigations and findings. The vortex dynamics near the cavity opening region is investigated as the potential primary source of noise generation. In addition, the noise generation mechanism is quantitatively explained by the onset of the separation region near the downstream corner that ensues from the synchronised shear layer–wall interaction. The current work extensively focuses on the fluid–acoustic coupling mechanism, and it is found that the acoustic resonance favourably modulates the hydrodynamic fluctuation near the upstream corner of the cavity. Furthermore, the current study also suggests that non-linear interactions between fundamental acoustic resonance and higher harmonics are plausible. Based on the discussions provided in this paper, a semi-empirical model to predict the critical free stream velocity at which a strong fluid–acoustic coupling occurs as a function of cavity geometry and inflow boundary-layer property is proposed. Finally, effect of flow speed on hydrodynamic and acoustic modes in the orthogonal and deep cavity is investigated.

3.1 Pressure fluctuations and oscillation frequencies

The self-sustained oscillation in deep cavities is often described as a fluid-resonant oscillation, in which the shear layer oscillation couples with a depthwise acoustic mode of the cavity. When this happens, a distinct large-scale vortical structure will be reinforced by the acoustic resonance, and its interaction with the downstream corner promotes a maximum conversion of local flow energy into acoustic energy. This process is captured in the current computational results. The iso-contour of the pressure fluctuation illustrated in 3.1(a) shows a low-pressure region caused by the concentrated vorticity (not shown) near the cavity opening, and the wall-pressure contours indicate the predominance of compressive acoustic waves inside the cavity before the vortex impingement. Furthermore, a noticeable low-pressure region near the top surface of the downstream wall that ensues from the separated flow is observed and will be scrutinised later in 3.2. Subsequently, figure 3.1(b) shows the instant when the vortical structure induces a sufficient

downwash velocity to reattach the flow downstream. The reattachment of the flow causes the separation region to disappear. A rapid alteration of the pressure fluctuation in the cavity follows afterwards to signify subsequent rarefaction wave emissions.

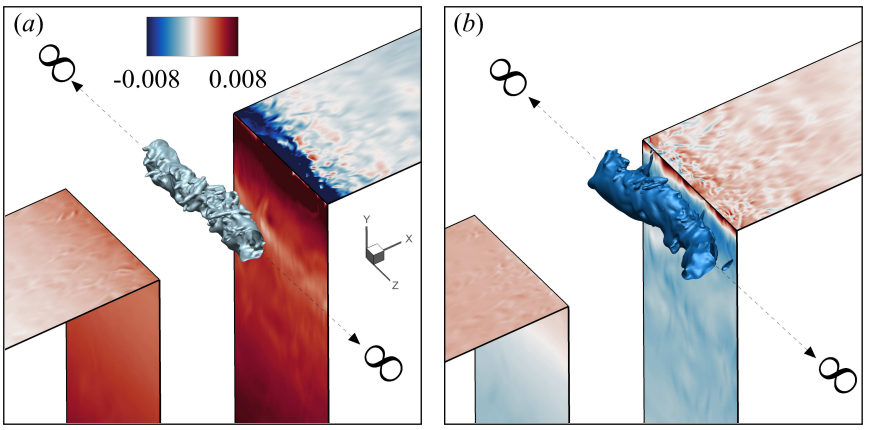

FIGURE 3.1: A large-scale vortical structure identified using iso-contour of instantaneous pressure fluctuation. Note that the flow is from left to right. The convection of the large-scale vortical structure and the associated change in wall-pressure fluctuation; (*a*) prior to the impingement; and, (*b*) after the impingement on the downstream corner, illustrate the aerodynamic noise emissions.

In this section, the focus is placed on the acoustic waves that manifest as the pressure fluctuates in the cavity. To realise this, the simulation is performed for 608000 time steps to attain a non-dimensional time of 100 for the wall-pressure at the cavity base to reach a steady-periodic state. Figure 3.2(*a*) shows the time signals of the wall-pressure fluctuation measured on the cavity base at three different streamwise positions, which converge to a similar solution after approximately $ta_\infty/L = 100$. Subsequently, Fourier transform is carried out on an additional non-dimensional time of approximately 540 samples (every 0.325 time unit) of the computational data over a total duration of non-dimensional time of 175, which corresponds to approximately 13 periods of the fundamental frequency. The resulting time signals are approximately periodic in time and any steady component is removed prior to the Fourier transform. Different windowing functions were attempted and the results show the comparable spectrum composition.

Figure 3.2(*b*) shows the respective PSD of the wall-pressure signals where a fundamental frequency peak was observed at $fL/a_\infty = 0.077$ and the rest were superseded by higher harmonics. The invariance of the spanwise-averaged wall-pressure fluctuation with respect to different streamwise locations on the cavity base can be understood by the fact that the wavelength of the acoustic field is much longer than the streamwise characteristic length of the cavity (i.e. $\lambda_a >> L$). Therefore, the cavity is assumed to be acoustically compact and the acoustic waves in the cavity can be modelled by a one-dimensional depthwise standing wave. This is a reasonable approximation in deep cavity configurations as the depth is usually longer than that in the streamwise direction. The pressure fluctuations around the cavity are characterised into two main regions, which are a local hydrodynamic fluctuation near the cavity opening and an acoustic fluctuation around the cavity. Therefore, it is essential to decompose these pressure fields into the hydrodynamic and acoustic components to facilitate the investigations. To achieve this, we employed the momentum potential theory (MPT) developed by Doak (1989). Essentially, in Doak's MPT, the momentum density ρu is separated into rotational and irrotational components through a Helmholtz decomposition. Subsequently, the hydrodynamic and acoustic pressure fluctuations are obtained by solving the Poisson equations in (4.3) and (4.4), respectively. The numerical implementation is described extensively in Unnikrishnan and Gaitonde (2016) and the

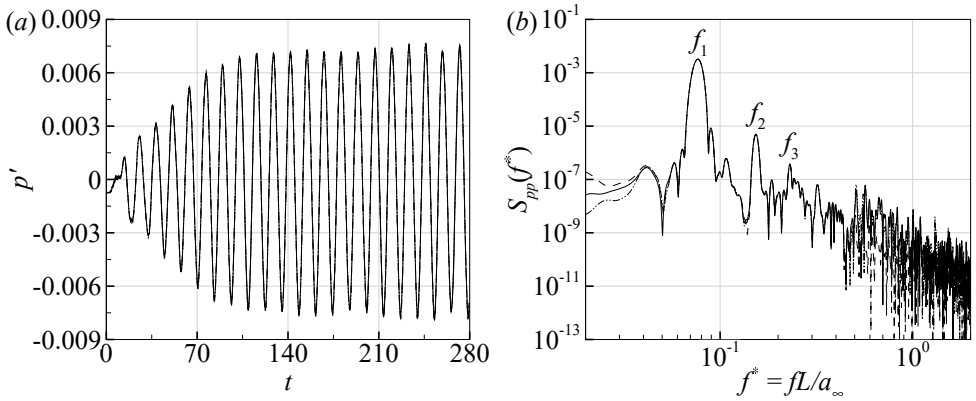

FIGURE 3.2: (*a*) Spanwise averaged of wall-pressure fluctuation time signals; and, (*b*) the corresponding PSD obtained at three different streamwise locations on the cavity base surface at $x/L = 0$ (——), $x/L = 0.5$ (- - -); and, $x/L = 1.0$ (-···-). The fundamental frequency is denoted by f_1, and the higher harmonics are represented by $f_2 = 2f_1$ and $f_3 = 3f_1$, respectively.

evaluations of the linear (S_H and S_A) and the non-linear source terms ($\tilde{S_H}$ and $\tilde{S_A}$) are detailed in Unnikrishnan and Gaitonde (2020), which are not repeated here for brevity.

Accordingly, the MPT is performed to decompose the pressure fields around the cavity into the hydrodynamic and acoustic components. Figure 3.3 shows snapshots of the spanwise-averaged instantaneous pressure fluctuation around the cavity region captured at four points in time separated by $T/4$ between two adjacent points, where $T = 1/f_1$ is the period of the oscillation at the fundamental frequency. Some discussions on the results shown in figure 3.3 can be made in relation to the acoustic pressure averaged over the bottom surface of the cavity, which is determined as:

$$\chi(t) = \frac{1}{A_b}\int_{A_b} p'_A(x_b,t)\mathrm{d}A, \tag{3.1}$$

where $y_b = -2.632L$ and $A_b = L_z L$ are the vertical coordinate and surface area of the cavity base, respectively. Figure 3.3(*a*) shows the beginning of the oscillation cycle of χ, where a large-scale vortex (represented by the low-pressure region) is located near the downstream corner, as shown in figure 3.3(*e*). At this instant, a complete destructive interference between the reflected compressive and the incident rarefaction acoustic waves results in a pressure equilibrium (e.g. $\chi = 0$) in the cavity. Subsequently, downward deflection of the shear layer and the formation of discrete low-pressure spots near the upstream corner are observed. The former event marks the beginning of the constructive interference of rarefaction acoustic waves in the cavity and the latter event signifies the formation of small-scale vortices near the upstream corner.

The interaction of the prior large-scale vortex with the downstream corner intensifies as the distinct low-pressure region is located closer to the downstream wall. This generates additional rarefaction waves, which constructively interfere with those reflected from the cavity base. Consequently, the wall-pressure fluctuation reduces until a minimum χ is exerted on the cavity base, as shown in figure 3.3(*b*). Concurrently, the coalescence of newly formed vortices into organised structures synchronises with the continual downward deflection of the shear layer near the upstream corner, as observed in figure 3.3(*f*). This is followed by the emergence of a local high-pressure region near the downstream wall caused by the impeded shear layer that signifies the inception of stagnated flows.

As the flow field is severely retarded by the downstream corner, a highly stagnated region is established, and this is accompanied by an increase in pressure fluctuation near the downstream wall, as shown in figure 3.3(*g*). Similarly, the shear layer–wall interaction also amplifies the

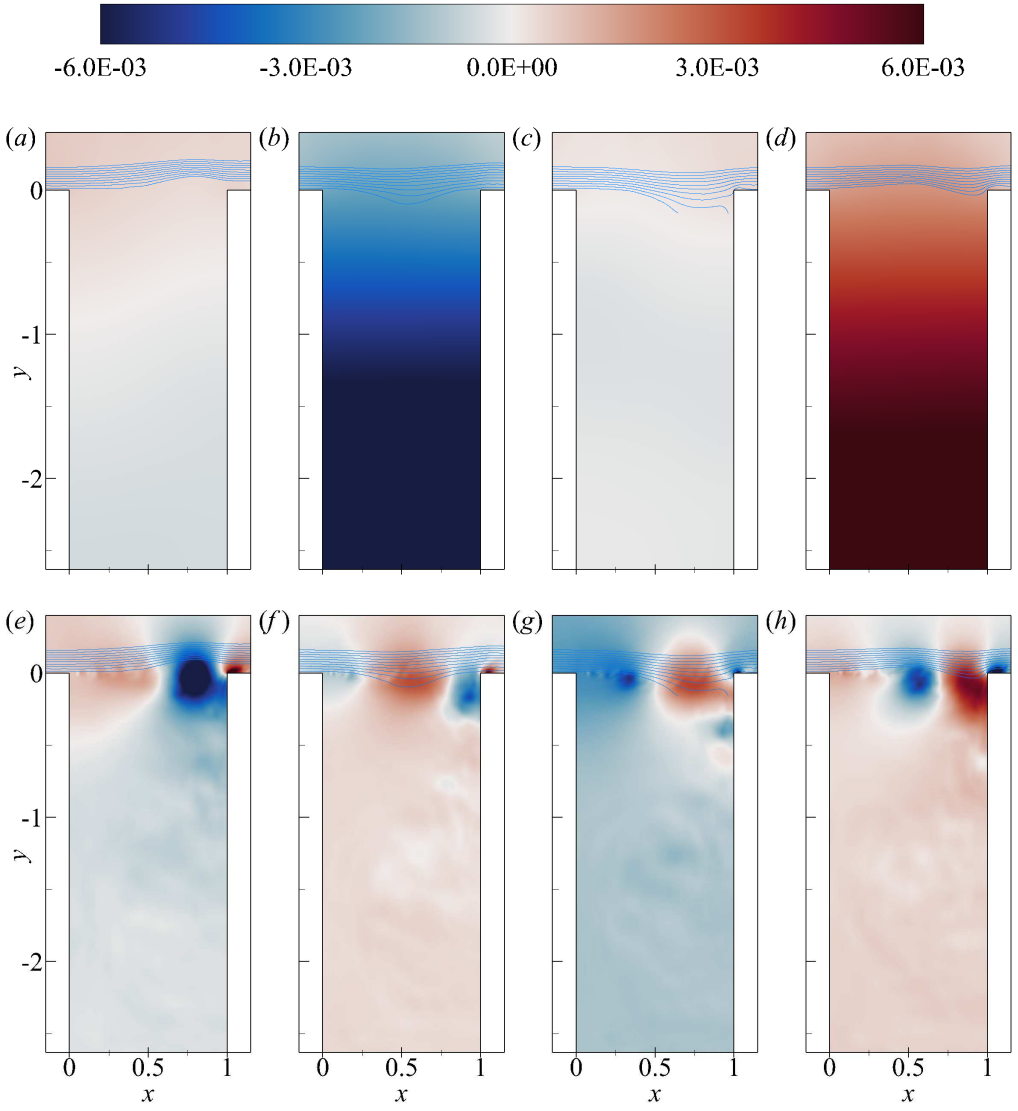

FIGURE 3.3: Snapshots of the spanwise averaged instantaneous pressure fluctuations around the cavity with superimposed streamlines to signify the shear layer undulations across the cavity opening with a time interval of $T/4$ between two successive plots from (a) to (d) for the acoustic component, p'_A; and, from (e) to (h) for the hydrodynamic component, p'_H, where T is the period of the oscillation cycle of χ.

low-pressure region at the top surface of the downstream wall owing to flow separation. At this moment, a complete destructive interference between the incident compressive acoustic waves and the rarefaction waves reflected from the cavity base is observed, as shown in figure 3.3(c). Subsequently, this is followed by the successive constructive interference in the cavity accompanied by an increase in the wall-pressure fluctuation. The newly-formed vortices near the upstream corner undergo a series of amalgamations into a large-scale vortex is represented by the distinct low-pressure region shown in figure 3.3(g).

Figure 3.3(d) shows the instant when the averaged acoustic wall pressure χ acting on the cavity base is a maximum, owing to the complete constructive interference of compressive acoustic waves. At this time, the shear layer slowly detaches from the downstream corner, which alleviates the high-pressure region from the flow stagnation. Simultaneously, the arrival of the newly-formed large-scale vortex induces sufficient downwash velocity to reattach the flow near

the downstream corner, which causes the low-pressure region that stems from the separation bubble to disappear, as shown in figure 3.3(*h*). Accordingly, a complete destructive interference occurs when the large-scale vortex impinges onto the downstream corner to complete a single oscillation cycle of χ.

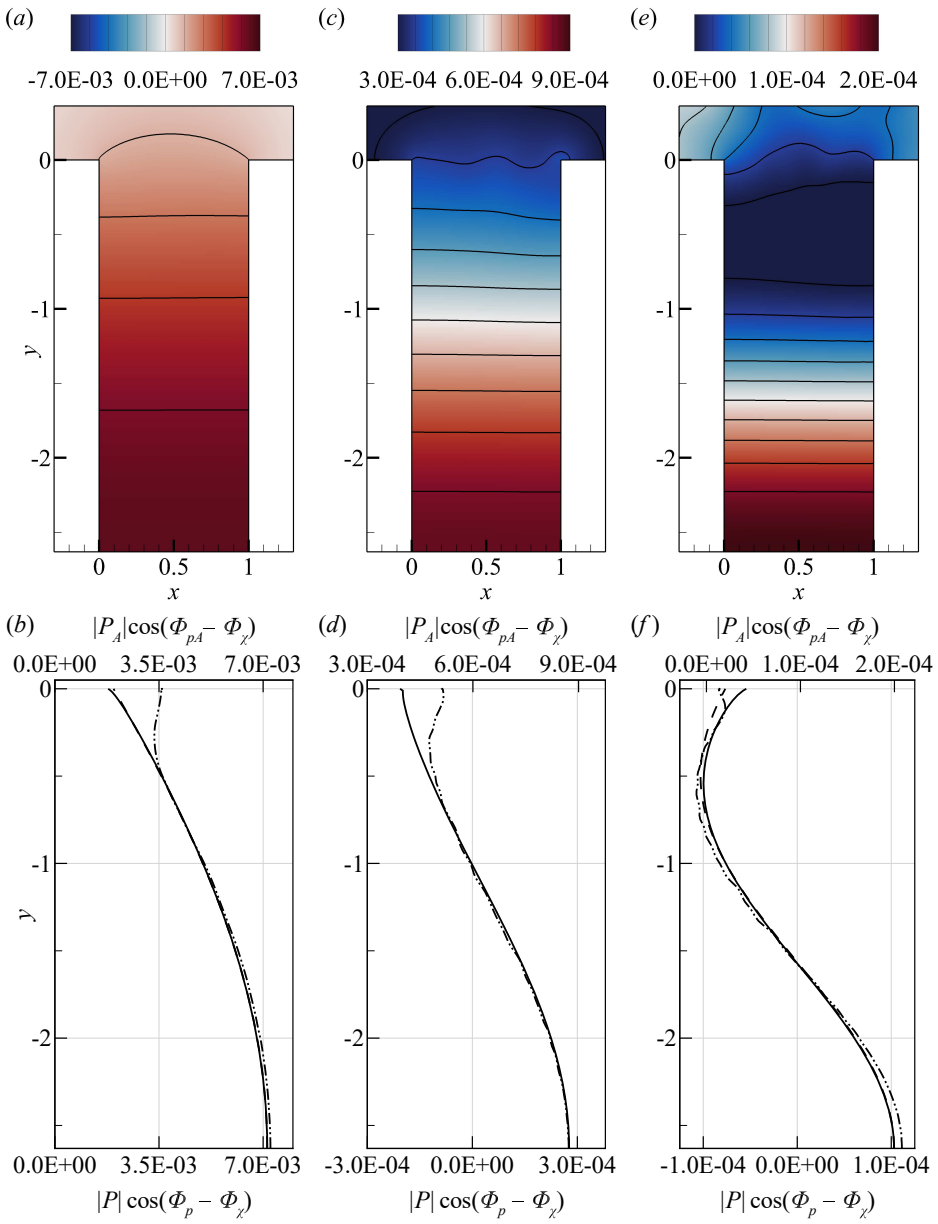

FIGURE 3.4: Contour plots of spatial variation of the acoustic pressure fluctuation calculated by $|P_A|\cos(\Phi_{p_A}(x,f)-\Phi_\chi(x,f))$, and the distribution of the acoustic wall-pressure fluctuation (——), curve-fitted cosine function (- - -) and the total wall-pressure fluctuation (-···-) in the depthwise direction along the upstream wall (e.g. $x/L=0$) at (*a*, *b*) $f=f_1$; (*c*, *d*) $f=f_2$; and, (*e*, *f*) $f=f_3$. Note that $\Phi_\chi(x,f)$ represents the phase of the Fourier transform of χ defined in (4.1).

Subsequently, the Fourier transform is performed to investigate the pressure fields associated with the hydrodynamic and acoustic components around the cavity at the tonal frequencies. The spatial distribution of the Fourier transformed acoustic pressure fluctuation is shown in figure 3.4. Notably, the acoustic wall-pressure fluctuation p_A along the upstream wall shows that the amplitude increases along with the cavity depth, and the mode shape bears a close resemblance

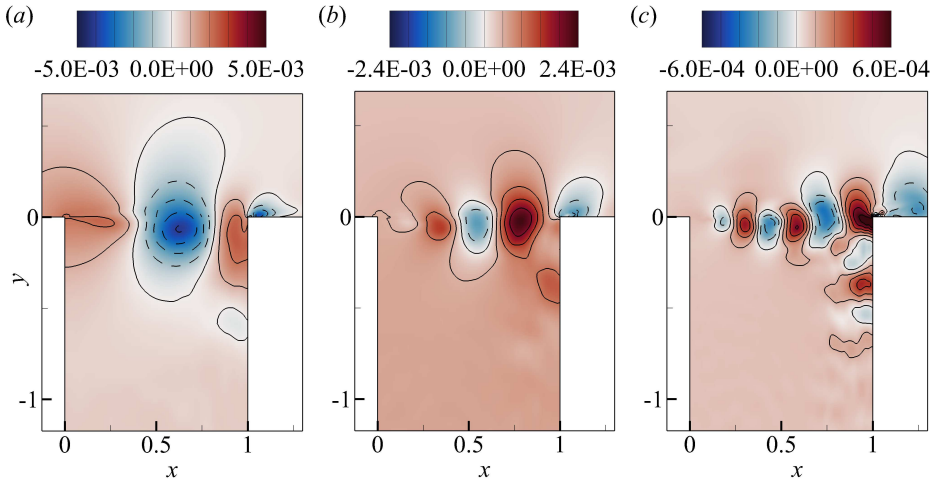

FIGURE 3.5: Spatial variation of the hydrodynamic pressure fluctuation near the cavity opening region, calculated by $|P_H|\cos(\Phi_{p_H}(x,f) - \Phi_{p_H}(x_0,f))$ at (a) $f = f_1$; (b) $f = f_2$; and, (c) $f = f_3$, where $\Phi_{p_H}(x_0,f)$ refers to the phase information at the upstream corner.

to a one-quarter acoustic standing wave at the fundamental frequency. In addition, a curve-fitted cosine function reveals the wavelength of the standing wave is in close agreement with the depth of the cavity. Thus, this result confirmed that the fundamental frequency peak is the consequence of the first depthwise acoustic resonance in the current cavity configuration. Furthermore, the transition to a higher acoustic mode is also apparent at higher harmonics, despite the magnitudes being significantly weaker, as revealed in figure 3.4(d, e). This may be attributed to the fact that smaller vortices that arise from the pairing process at the increased passage frequency, as shown in figure 3.5(b, c), are generally weaker than a single large-scale vortex (Ziada, 1994; Bravo et al., 2005). In addition, highly damped oscillations outside of the cavity resonant frequency range may weaken the overall fluid–acoustic coupling mechanism (Koch, 2005).

In short, these spectral results reveal that the current cavity configuration facilitates an efficient conversion of the hydrodynamic energy to acoustic energy at the resonant frequency. Therefore, the possibility of a fluid–acoustic coupling between the shear layer and the standing wave remains an interesting point to study. Before investigating this in more detail, it may be helpful first to discuss the hydrodynamic field near the cavity opening in Section 3.2, followed by the subsequent interaction with the acoustic resonance later in Section 3.3.

3.2 Hydrodynamic field and the associated noise generation mechanism

In this section, the hydrodynamic field across the cavity opening will be discussed in detail. The previous discussion has indicated that the location of the large-scale vortex plays a primary role in the acoustic wave emission process. Therefore, an accurate assessment of the position and the actual path travelled by the vortical structure, which are functions of time, is important in this investigation. Generally, the location of the vortical structure can be extracted by using the pressure minima technique. Figure 3.5 shows the real part of the Fourier transformed hydrodynamic pressure fluctuation around the cavity opening region at the tonal frequencies, and the number of vortices (e.g. low-pressure region) increases following the passage frequencies. Furthermore, the streamwise amplification of the hydrodynamic pressure arising from the coherent vortex formation at the tonal frequencies is observed in figure 3.6. However, an accurate quantification

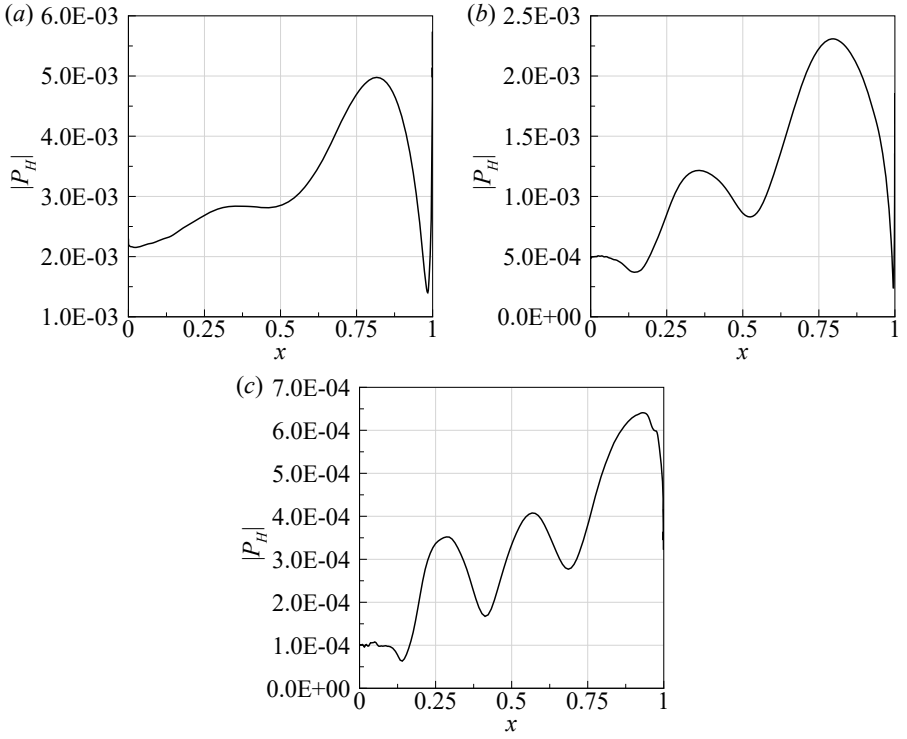

FIGURE 3.6: Streamwise variation of the magnitude of Fourier transformed hydrodynamic pressure fluctuation, $|P_H(x,f)|$ along the cavity opening (e.g. $y/L = 0$) at (*a*) $f = f_1$, (*b*) $f = f_2$ and (*c*) $f = f_3$.

of the hydrodynamic mode based on the number of discrete low-pressure spots is difficult to justify owing to the possible influence from the separation region near the downstream corner. To overcome this, the location of the vortical structure is identified by the equivalent Q-criterion. According to Bradshaw (1981), this is given by:

$$Q = \varepsilon_{ij}\varepsilon_{ji} - \frac{1}{2}\omega_i^2 \approx -\nabla^2 p_H/\rho_\infty = \tilde{Q}, \tag{3.2}$$

where $\varepsilon_{ij} = \frac{1}{2}(\partial u_i/\partial x_j + \partial u_j/\partial x_i)$ is the rate of strain, ω_i is the vorticity of the velocity field and $\nabla^2 p_H$ is the Laplacian of the hydrodynamic pressure field. The advantage of this formulation has two folds, firstly (4.7) provides a link between the velocity gradient field and the hydrodynamic pressure field to better locate the position of the vortex. Second, the strain-rate and vorticity fields provide physical interpretations of the velocity field, which are useful in qualifying the following noise generation mechanism.

Figure 3.7 shows an oscillation cycle of χ similar to that of figure 3.3, with particular attention given to the vortex dynamics near the cavity opening region. Plotted is the Q-criterion, where Q is calculated from (4.7), and superimposed are streamlines to signify the shear layer oscillation near the cavity opening. The instant when the large-scale vortex impinges on the downstream corner is shown in figure 3.7(*a*). Note that the large-scale vortex core location prior to the impingement is slightly below the cavity opening line (e.g. $y/L < 0$). Consequently, the interaction of the vorticity field with the front surface of the downstream wall necessitates an imaginary mirror image of an opposite vorticity field to satisfy the no-slip boundary condition at the wall. The presence of near-wall vorticity translates into a low hydrodynamic pressure field because $\nabla^2 p_H > 0$. This induces rarefaction acoustic waves that destructively interfere with the reflected compressive acoustic waves in the cavity. Simultaneously, the separated shear layer emanated

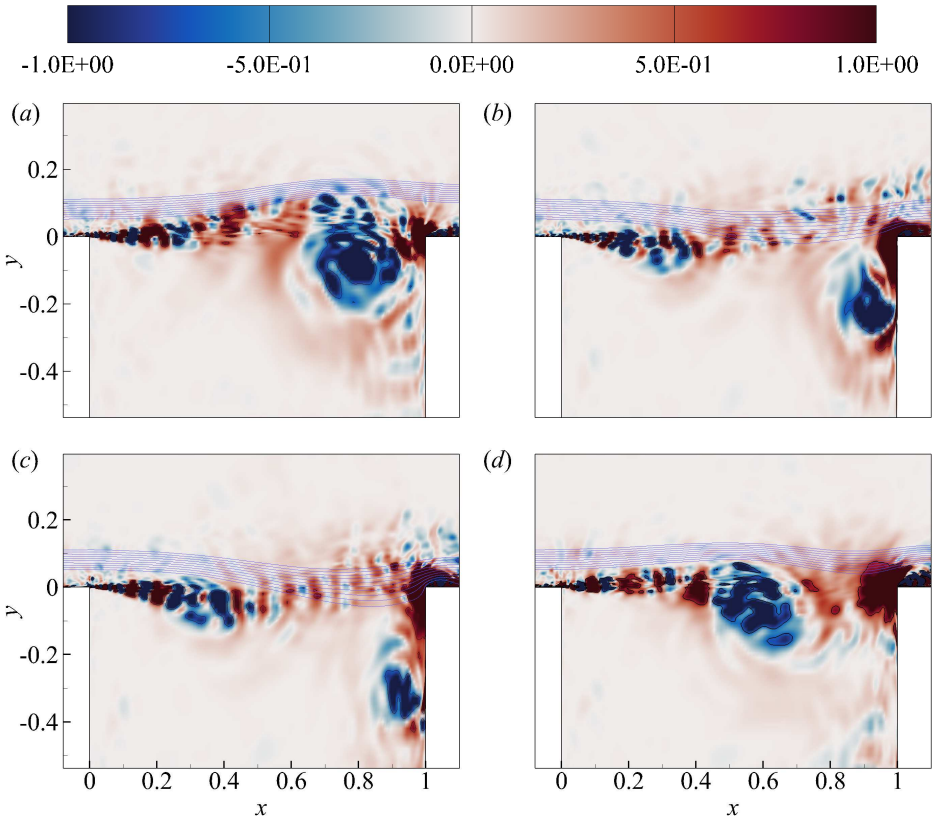

FIGURE 3.7: The vortex dynamics near the cavity opening region. Plotted is the contour of the Q-criterion, Q calculated from (4.7) and the superimposed streamlines to signify the gross deflection of the shear layer. For the corresponding pressure fields, see figure 3.3.

from the upstream corner develops small-scale vortices caused by the Kelvin–Helmholtz instabilities before the coalescence into coherent vortices under the influence of acoustic forcing.

As the large-scale vortex fully impinges on the front surface of the downstream wall, the vorticity field acting on the wall is amplified, and this necessitates an imaginary mirror image of a stronger opposite vorticity field to counteract the imposed vorticity field. As a result, additional rarefaction acoustic waves are generated, which interfere constructively with the acoustic waves reflected from the cavity base. This is followed by a downward deflection of the shear layer near the downstream corner, which leads to the formation of a secondary vortex as the large-scale vortex is stretched and swept down into the cavity, as shown in figure 3.7(b). The formation of the separated boundary layer induces a compressive pressure field (e.g., $\nabla^2 p_H < 0$) on the front surface of the downstream wall, similar to the vortex–ring/wall interaction reported by Naguib and Koochesfahani (2004). Also, the shear layer–wall interaction forms a region of a high-strain-rate field (e.g. $Q > 0$) on the downstream wall owing to stagnated flow, and a high vorticity field (e.g. $Q < 0$) on the top surface of the downstream wall that ensues from the flow separation. These concurrent events mark the beginning of emission of the overall compressive acoustic waves.

As the shear layer is further displaced downward near the downstream corner, as shown in figure 3.7(c), the strain rate intensifies in response to a higher degree of flow stagnation, which corresponds to further emissions of compressive acoustic waves. Similarly, a large amplitude low-pressure region is formed near the edge of the top surface of the downstream corner owing to excessive flow separation. At the same time, the newly formed vortices near the upstream

corner begin to form a large-scale vortical structure (represented by $Q < 0$) through additional vortex pairings, which is visually similar to the 'collective interaction' according to Ho and Nosseir (1981).

As the shear layer slowly detaches from the downstream corner, the high-strain-rate region caused by the stagnated flow is gradually alleviated, and the high vorticity region reduces as the flow reattaches. Further development of the vortical structure stemming from the additional vortex pairings is observed, as shown in figure 3.7(d). This is followed by the impingement of the newly formed large-scale vortex on the downstream front surface of the wall, as shown in figure 3.7(a). As a result, a low-pressure region is exerted onto the downstream wall, and the separation region disappears completely when the flow is fully reattached. This type of vortex–corner interaction, where the vortical structure impinges directly onto the downstream wall, is known to produce an intense pressure fluctuation similar to a dipole source (Tang and Rockwell, 1983).

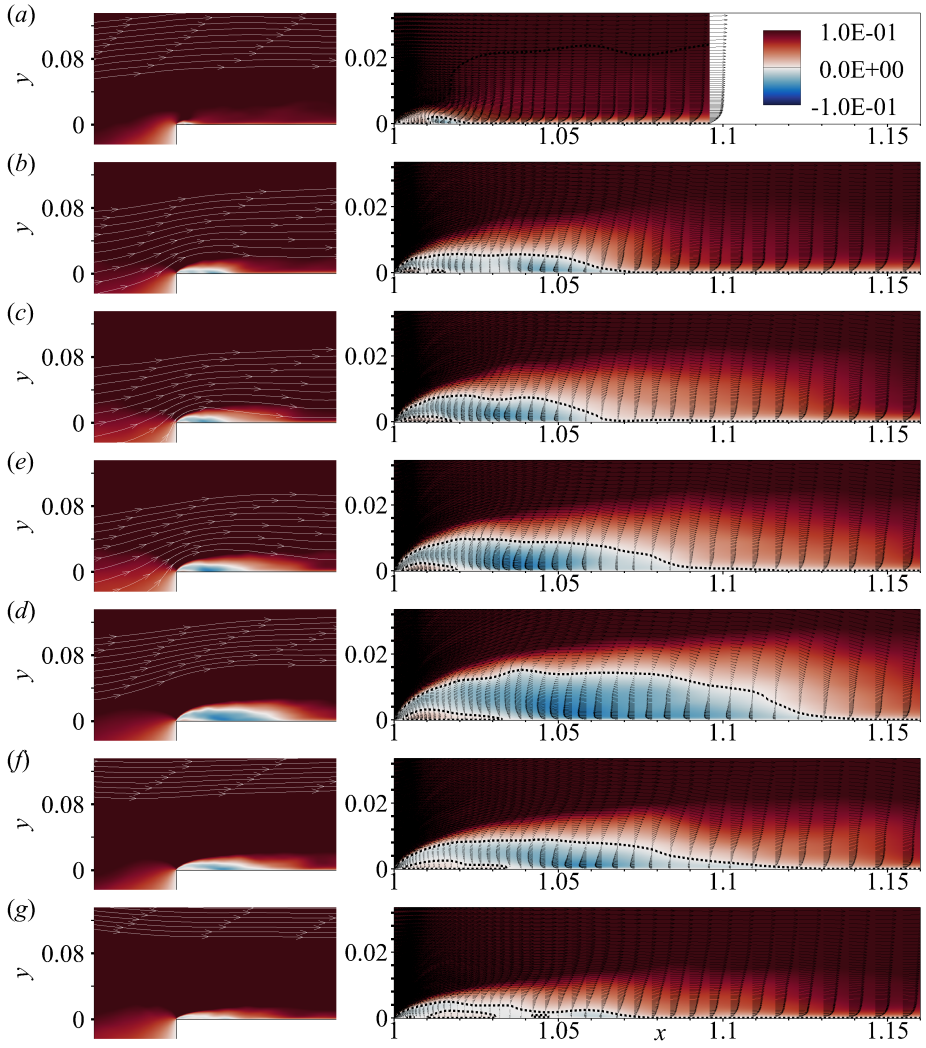

FIGURE 3.8: Distribution of spanwise averaged instantaneous streamwise velocity in and around the separation bubble near the top surface of the downstream wall at the indicated time instants in figure 3.9. The contours (left) are superimposed with streamlines to visualise the deflection of the shear layer; and (right) are superimposed with instantaneous velocity vectors and the dashed lines are used to indicate the surfaces of separation bubble by iso-lines at which the streamwise velocity is zero (e.g. $u = 0$).

In the current investigation, the separation bubble formation is synchronized with the acoustic pressure fluctuation in the cavity and is dependent upon the vertical displacement of the shear layer near the downstream corner. To illustrate this, a few representative parameters are first introduced. The upper and lower surfaces of the separation bubble are defined by the iso-lines of zero streamwise velocity (e.g. $u = 0$). Then, the area of the separation bubble region (A_{SB}) is defined by integrating the wall-normal distance along these iso-lines in the streamwise direction. Accordingly, the similarity in time variation of A_{SB} and the averaged wall-pressure fluctuation χ are shown in figure 3.9. From figure 3.8, the periodic pulsation of the separation bubble around the downstream corner of the cavity indicates there is a significant change in flow momentum (both vertically and horizontally), which results in a strong periodic wall-pressure fluctuation that translates into sound emissions. Therefore, it is speculated that the onset of the separation bubble as a consequence of the shear layer undulation could be used as an indication of the acoustic emission process.

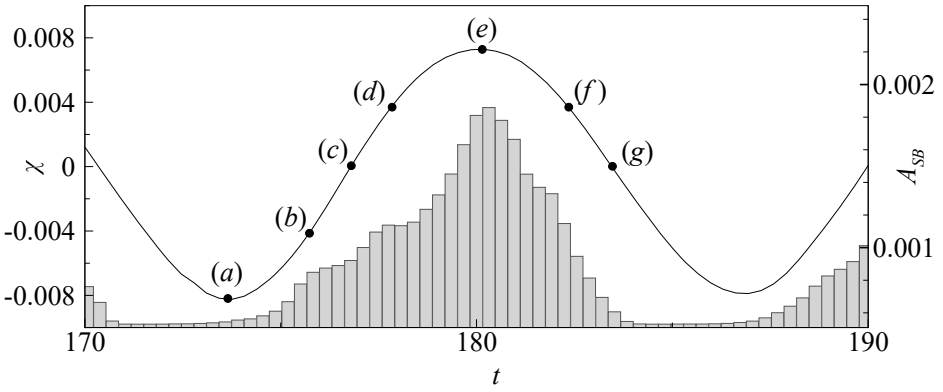

FIGURE 3.9: Time variation of the separation bubble area, A_{SB} (shown by the histogram) caused by flow separation/reattachment near the top surface of the downstream corner. Plotted also is the averaged acoustic wall-pressure fluctuation exerted on the cavity base, χ (——) to signify the following flow events: the minimum point (a) indicates the beginning of the downward deflection of the shear layer, leading to the formation of low-pressure region ensued from the flow separation at the top surface of the downstream corner. The equilibrium point (g) indicates the disappearance of separation region due to the reattached flow by the arrival of the large-scale vortex near the downstream corner.

From the discussion above, it is clear that the interaction of the large-scale vortex (vorticity field) with the downstream corner mainly contributes to the rarefaction (low-pressure) acoustic waves inside the cavity. In contrast, the stagnation (strain-rate field) and separation flow caused by the undulation of the shear layer near the downstream corner are jointly responsible for compressive (high-pressure) acoustic wave emission inside the cavity. Therefore, it may be possible to describe the aerodynamic noise generation owing to the unsteady loading near the downstream corner in terms of a surface source according to Curle (1955). Another possible explanation of the noise generation mechanism can be attributed to the shear layer deflection across the cavity opening (Elder, 1980). Specifically, Dai et al. (2015) suggested that the shear layer oscillation couples with the cavity acoustic mode through an explicit force-balance relationship between the two sides (i.e., cavity opening and the cavity base). Accordingly, figure 3.10(a, b) shows the space–time contour plots of the rate of change of decomposed vertical momentum density across the cavity opening (e.g. $y/L = 0$), where the solenoidal component B_y induced by the large-scale vortex is highly localized in space compared with the uniformly distributed irrotational component $\nabla\psi_A$. By integrating the vertical momentum density rate $d(\rho v)/dt$ across the cavity opening in the streamwise direction, the total mass flow rate $\dot{m}$ is separated into the

solenoidal and irrotational components by:

$$\frac{dm_A}{dt}(t) = -\frac{1}{dt}\int_0^L \nabla\psi_A(x, y=0)\,dx, \tag{3.3a}$$

$$\frac{dm_H}{dt}(t) = \frac{1}{dt}\int_0^L B_y(x, y=0)\,dx. \tag{3.3b}$$

From figure 3.10(c), it is apparent that the rate of change of the acoustical mass flow rate across

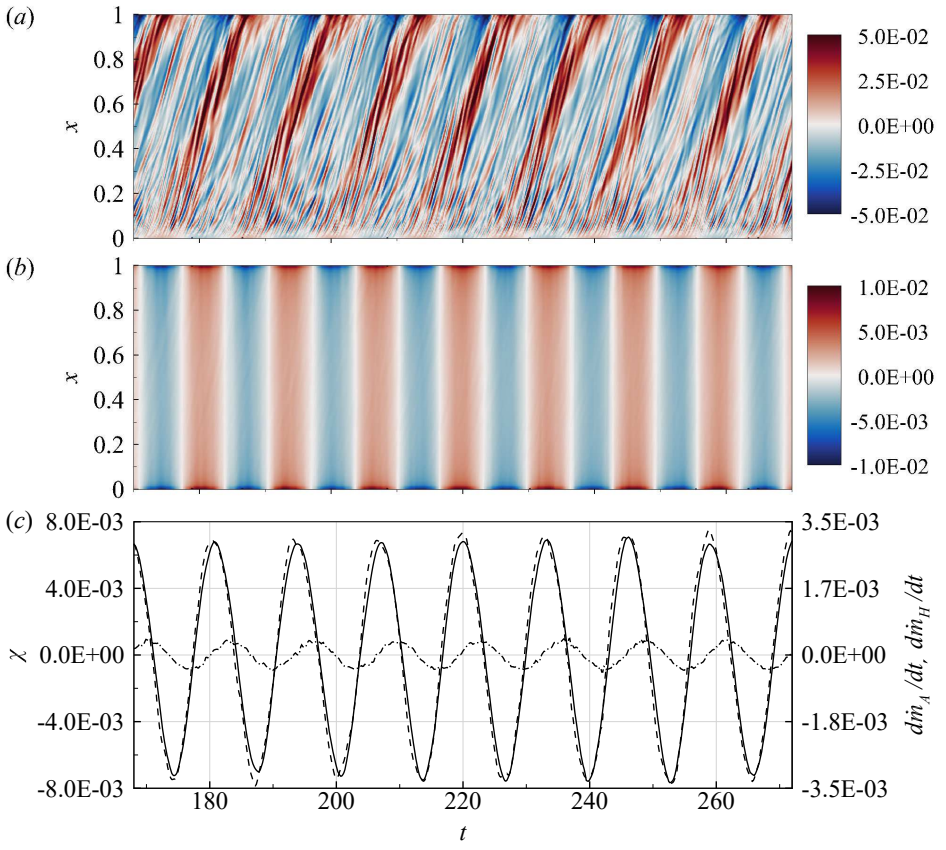

FIGURE 3.10: Space-time contour plots of (a) the solenoidal (hydrodynamic) component; (b) the irrotational (acoustic) component of the rate of change of vertical momentum-density, $\partial(\rho v)/\partial t$ across the cavity opening (e.g. $y/L = 0$); and, (c) the force-balance relationship between the averaged acoustic wall-pressure fluctuation at the cavity base, $\chi(t)$ (——), rate of change of acoustical mass flow rate, $dm_A(t)/dt$ (- - -) and hydrodynamic mass flow rate, $dm_H(t)/dt$ (-···-) across the cavity opening.

the cavity opening is proportional to the acoustic force exerted on the cavity base, that is:

$$\frac{dm_A}{dt}(t) \propto \chi(t). \tag{3.4}$$

A similar relationship was inferred for shallow cavity flows by Rowley et al. (2002). Furthermore, the present result shows that the force exerted across the cavity opening is predominantly associated with the acoustic component, which may be useful in explaining the synchronized oscillation of the shear layer with the acoustic field in the cavity.

3.3 Fluid-acoustic coupling mechanism

In Section 3.1, it is evident that the fundamental resonant frequency with a mode shape similar to a one-quarter wave is presented in the cavity. Therefore, one needs to determine whether an effective coupling mechanism exists between the shear layer and the acoustic resonance to facilitate this formation. As mentioned, past investigations have indicated the acoustic resonance has a deterministic role on shear layer oscillation, particularly near the receptivity of the shear layer (e.g., upstream corner). Therefore, a better understanding of the phase relationship between the region of maximum receptivity of the shear layer and the acoustic resonance is crucial in this investigation. One plausible way to achieve this is to invoke the one-dimensional plane wave approximation, whereby the standing wave induces acoustic particle velocity primarily in the vertical direction. This approximation is justified for the current cavity configuration based on our previous observation in Section 3.1, where the acoustic pressure field bears a close resemblance to a one-quarter vertical standing wave. Accordingly, the Fourier transform is performed on the space–time vertical velocity fluctuation across the cavity opening, and the respective magnitude $|V(x,f)|$ and phase $\Phi_v(x,f)$ at the tonal frequencies are plotted in figure 3.11.

At the resonant frequency, the streamwise amplification follows an almost linear fashion to reach up to $x/L \approx 0.55$ before reducing to a local minimum and rising to a concentrated peak near the downstream corner, as shown in figure 3.11(a). The former reduction is caused by the nonlinear saturation mechanism, which prevents the unbounded growth of the vortex strength. The latter is caused by the intensified strain-rate field generated by the shear layer–wall interaction discussed in Section 3.2. In addition, the cosine of the phase difference $\cos[\Phi_v(x,f_1) - \Phi_\chi(x,f_1)]$, as shown in figure 3.11(a), reveals a region of frequency modulation where the velocity fluctuation near the upstream corner remains highly synchronized with the averaged acoustic wall-pressure fluctuation at the cavity base χ. This demonstrates the important point that the vertical velocity oscillation in the separated shear layer is highly controlled by the depthwise acoustic resonance. Subsequently, the modulated shear layer oscillation and the subsequent amalgamation of vortices at the resonance state are manifested through the linear amplification regime.

At the first harmonic frequency, an exponential streamwise amplification of the vertical velocity fluctuation is observed near the upstream region (e.g. $x/L < 0.15$). It is then followed by the transition to a linear amplification rate up to $x/L \approx 0.6$ before the onset of nonlinear saturation, as shown in figure 3.11(c). The former exponential amplification rate can be explained by the lack of acoustic reinforcement owing to the out-of-phase relationship (e.g. $\cos[\Phi_v(x,f_2) - \Phi_\chi(x,f_2)] < 0$) near the upstream region (e.g. $x/L < 0.15$), as shown in figure 3.11(d). Therefore, the formation of coherent vortices is retarded and results in a free shear layer oscillation that may be described by the linear theory (Michalke, 1972). The transition to a linear amplification begins when the vertical velocity fluctuation is in-phase (e.g. $\cos[\Phi_v(x,f_2) - \Phi_\chi(x,f_2)] > 0$) near $x/L \approx 0.15$. In this linear amplification regime, the hydrodynamic instabilities are amplified and evolve into coherent vortex structures in response to the synchronized acoustic forcing. Subsequently, this is followed by an onset of the nonlinear saturation before rising to a concentrated velocity peak near the downstream corner caused by the intensified strain-rate field.

At the second harmonic frequency, the exponential streamwise amplification near the upstream region is replaced by a primary linear amplification, as shown in figure 3.11(e), which implies an acoustic reinforcement based on the evidence provided above. This is apparent in figure 3.11(f) where the vertical velocity fluctuation near the upstream region is highly in-phase with χ at both the resonant frequency (e.g. $\cos[\Phi_v(x,f_3) - \Phi_\chi(x,f_1)] > 0$) and the second harmonic frequency (e.g. $\cos[\Phi_v(x,f_3) - \Phi_\chi(x,f_3)] > 0$). Similarly, it is also noticeable that the

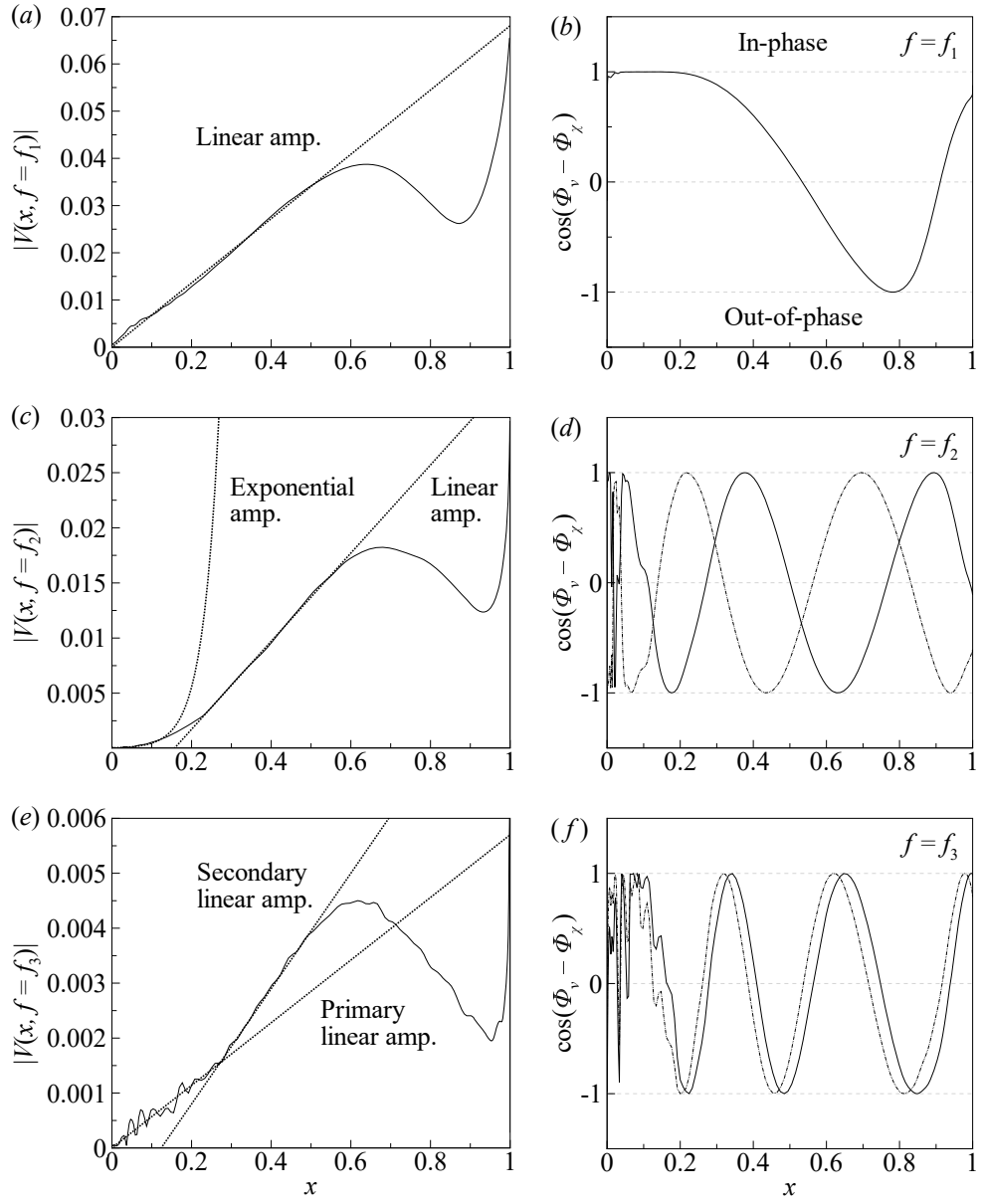

FIGURE 3.11: Streamwise variation of magnitude and phase of the Fourier transformed vertical velocity fluctuation, $V(x,f)$ across the cavity opening (e.g. $y/L = 0$) at (a, b) $f = f_1$; (c, d) $f = f_2$; and, (e,f) $f = f_3$. In plots (a, c, e), the magnitude $|V(x,f)|$ is represented by (——) and the regression lines (·····) are used to indicate the amplification rate(s). In plots (b, d, f), the cosine of the phase difference, $\cos[\Phi_v(x,f) - \Phi_\chi(x,f_1)]$ is shown by (——), while the dashed line (- - -) is used to denote $\cos[\Phi_v(x,f) - \Phi_\chi(x,f_2)]$ in (d) and $\cos[\Phi_v(x,f) - \Phi_\chi(x,f_3)]$ in (f), respectively.

transition to a secondary linear amplification occurs when the vertical velocity fluctuation begins to oscillate in synchrony with the acoustic field near $x/L \approx 0.25$. As a result, this additional reinforcement translates into a larger linear amplification. Accordingly, the vertical velocity fluctuation is amplified further before being suppressed by the nonlinear saturation followed by a concentrated velocity peak caused by the intensified strain-rate field.

Additionally, it is worth investigating how the acoustic forcing magnitude in terms of the acoustic particle velocity varies at each tonal frequency. Based on the mode shapes of the standing waves observed in figure 3.4, the induced acoustic particle velocity at the cavity opening can be approximated by the isentropic Euler equations according to Rienstra (2015) and is given by:

$$\frac{dv_A}{dt} = -\frac{\nabla p_A}{\rho}, \tag{3.5}$$

where v_A represents the induced acoustic particle velocity and p_A is the decomposed acoustic pressure field. By considering a sinusoidal fluctuation of the acoustic pressure and incompressibility, we obtain:

$$v_A = \frac{\nabla p_A}{2\pi f}, \tag{3.6}$$

an estimated acoustic particle velocity magnitude of approximately $|v_A|/U_\infty \approx 3.7 \times 10^{-2}$ for the fundamental frequency, $|v_A|/U_\infty \approx 7.8 \times 10^{-4}$ for the first harmonic frequency, and $|v_A|/U_\infty \approx 3.7 \times 10^{-4}$ for the second harmonic frequency. At the fundamental resonant frequency, the acoustic particle velocity magnitude corresponds to a "moderate pulsation level" category, in which the nonlinear effects reinforce a concentration of the vorticity shed at the upstream corner into a large-scale vortex (Bruggeman et al., 1991), which aligns with figure 3.7. Coincidentally, the Strouhal number based on momentum thickness $St_\theta = f_1\theta/U_\infty = 0.0148$ is close to the subharmonic of the most-amplified frequency of a turbulent free shear layer $St_\theta = f\theta/U_\infty = 0.024$ Ho and Huang (1982). This may allow an enhanced vortex to merge in the forced shear layer through the "collective interaction mechanism", according to Ho and Huang (1982). At higher harmonics, the values of the acoustic particle velocity magnitude correspond to "low pulsation levels", in which the linear theory is applicable to explain the exponential amplification of the free shear layer perturbation at the first harmonic frequency observed in figure 3.11(*c*), with the exception of the second harmonic frequency shown in figure 3.11(*e*). Therefore, it is postulated that the transition from a free shear layer oscillation (e.g., exponential amplification) to the formation of coherent vortices (e.g., linear amplification) necessitates the condition of a favourable phase relationship between the hydrodynamic and acoustic particle velocity fluctuations (e.g. $\cos[\Phi_v(x,f) - \Phi_\chi(x,f)] > 0$).

3.4 Convection speed of coherent vortical structures

As discussed earlier, the streamwise phase variation of the hydrodynamic pressure fluctuation is not a reliable measurement of the hydrodynamic mode due to the influence from the separation region near the downstream corner. Therefore, inspired by the reasoning in Section 3.2, the Q-criterion, where Q is calculated from (3.8), is used. Accordingly, the Fourier transform is performed and the respective magnitudes $|Q(x,f)|$ are plotted in figure 3.12. The frequency-space contour in figure 3.12(*a*) shows that the concentrations of the Q-criterion near the upstream corner are mostly energetic near the fundamental frequency and much weaker at higher harmonics. Additionally, figure 3.12(*b–d*) depict the propagation pathways of coherent vortical structures across the cavity opening at the tonal frequencies, where the elevations are slightly below the

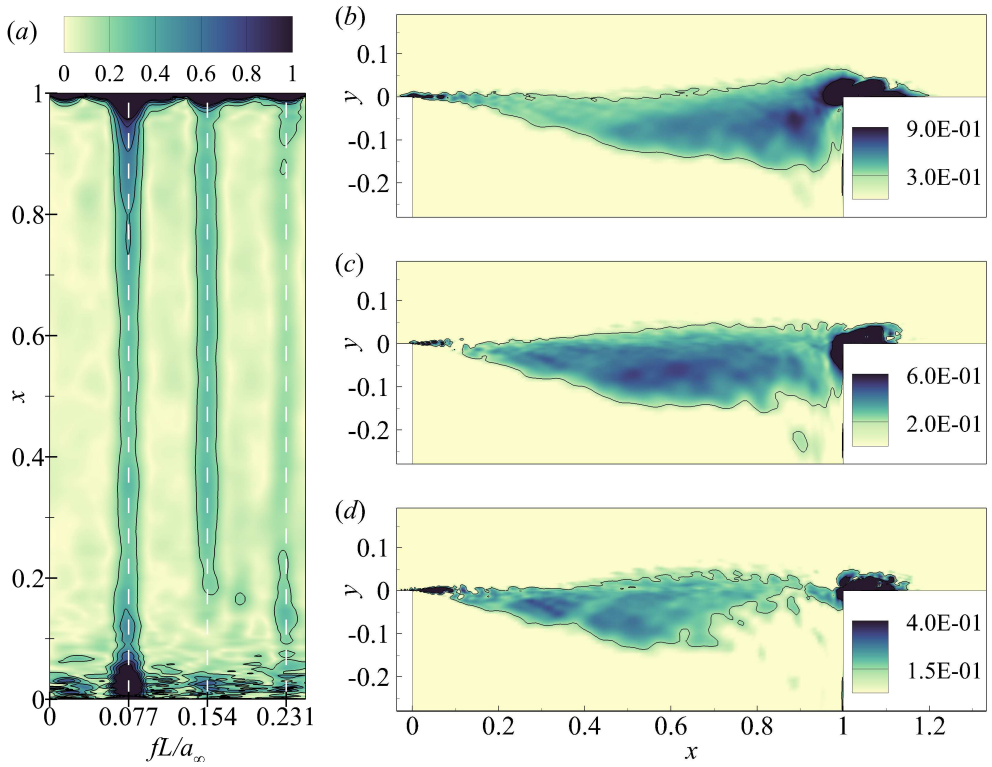

FIGURE 3.12: (*a*) Contour plot of the space-frequency variation the Fourier transformed Q-criterion magnitude, $|Q(x,f)|$ across the cavity opening (e.g. $y/L = 0$), and the respective spatial variation of $|Q(x,f)|$ at (*a*) $f = f_1$; (*b*) $f = f_2$; and, (*c*) $f = f_3$.

cavity opening line. To account for the variation in elevation, the phase measurement is performed along a line in the streamwise direction where the elevation is determined by the location of maximum magnitude. Figure 3.13(*a*) shows the streamwise phase variation of $\Phi_Q(x,f_1)$ and the respective $\Phi_{\tilde{Q}}(x,f_1)$ across the cavity opening. It is evident that Q remains highly in-phase with χ near the upstream corner before completing an approximate single oscillation cycle. This result confirms two important points. First, the formation of small-scale vortices is highly in-phase with the acoustic forcing near the upstream region, suggesting strong evidence of frequency modulation by the acoustic resonance in the cavity (e.g. $\cos[\Phi_Q(x,f_1) - \Phi_\chi(x,f_1)] = 1$). Second, the phase criterion $\Delta\Phi_Q(x,f_1) = 2\pi$ needs to be satisfied for a self-sustained oscillation of the first hydrodynamic mode, in accordance with (Rockwell and Naudascher, 1979; Knisely and Rockwell, 1982; Rockwell, 1983; Tuna and Rockwell, 2014). Similar descriptions are also applicable to the higher harmonics, as shown in figure 3.13(*b*, *c*). Based on the linear dispersion relation, the phase variation corresponds to an average vortex convection speed ratio of $k = U_c/U_\infty = 0.386$ at each tonal frequency. This value is close to the suggested values for deep cavities, such as $k = 0.3$ by Graf and Durgin (1993), $k = 0.38$ by Ma et al. (2009), and $k = 0.4$ by (Nelson et al., 1983; Bruggeman, 1987; Bruggeman et al., 1991).

3.5 Prediction of the critical freestream velocity

The primary aim of this investigation is to devise a semi-empirical model to predict the critical free stream velocity at which the incoming turbulent boundary layer couples with a depthwise acoustic resonance in deep cavities. The motivation is driven by the fact that the physical mechanism, which involves the depthwise resonance of deeper cavities with high aspect ratios

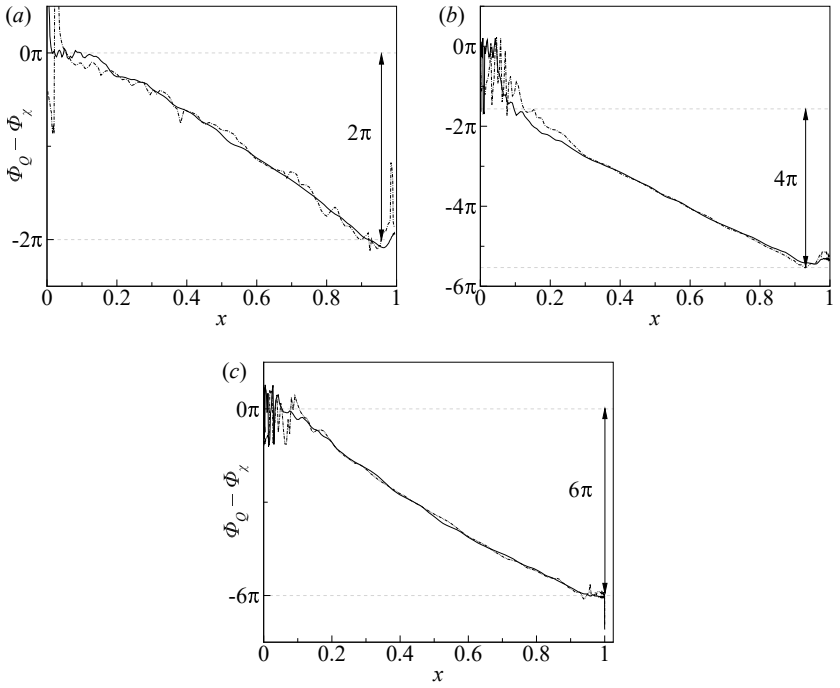

FIGURE 3.13: Streamwise phase variation of the Q-criterion, $\Phi_Q(x,f)$ (——) and the respective Laplacian of hydrodynamic pressure field, $\Phi_{\tilde{Q}}(x,f)$ (- - -) at (*a*) $f = f_1$; (*b*) $f = f_2$; and, (*c*) $f = f_3$. Note here that the phase, $\Phi_Q(x,f)$ and $\Phi_{\tilde{Q}}(x,f)$ are both calculated based on the phase reference of $\bar{\Phi}_\chi(x,f)$.

$(D/L \gg 1)$, is still relatively under-examined. Therefore, in this section, a brief review of past attempts on the development of prediction models for cavity flows will be discussed. Based on the observations outlined in this paper, a prediction model of the critical free stream velocity that incorporates the cavity depth is proposed.

The physical mechanism that describes the self-sustained oscillation was first introduced by the feedback mechanism, according to Rossiter (1964). Rossiter observed that shallow cavities (with L/D ranging between 1 and 4) tend to generate aerodynamic tonal noises and then proposed an empirical formula to explain the feedback process. In terms of the Helmholtz number, it is given by:

$$\frac{f_n L}{a_\infty} = \frac{n-\alpha}{\frac{a_\infty}{U_c}+1}, \tag{3.7}$$

where n is the hydrodynamic mode. The empirical constant α is proposed to account for an additional emission delay and the ratio $\kappa = U_c/U_\infty$ is proposed to simplify the model by assuming a constant vortex convection velocity across the cavity opening. Thus, the physical interpretation of Rossiter's feedback mechanism contained in (3.7) can be described as the summation of time duration for the downstream propagation of a vortex at a constant convection velocity, and the subsequent upstream propagation of an acoustic wave at the speed of sound.

However, it is worth noting that the constants in Rossiter's formula (3.7) were determined empirically and justified heuristically. First, according to the authors' opinion, the empirical constant α is introduced without a strong justification. Second, the assumption that vortices propagate at a universal averaged speed ratio of $\kappa = 0.58$ deserves further scrutiny. In fact, as shown in Section 3.4, the averaged vortex convection velocity is estimated to be $\kappa = 0.386$, which is an underestimation of the value suggested by Rossiter (1964), and the use of $\alpha = 0$ seems to improve the prediction as demonstrated by several deep cavity investigations (Forestier

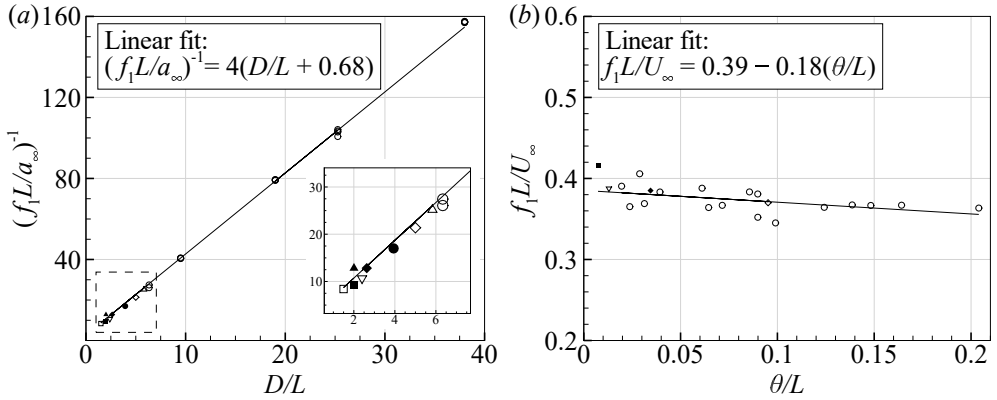

FIGURE 3.14: (*a*) Relationship between the period of fundamental resonant frequency and the aspect ratio of the cavities; and, (*b*) the relationship of Strouhal number with the momentum thickness of the approaching boundary layer. The symbols indicate the results from: (■) Ahuja and Mendoza (1995); (□) Block (1976); (▲) III et al. (1997); (△) Erickson and Durgin (1987); (▽) Forestier et al. (2003); (◆) Current LES; (◇) Hassan et al. (2007); (●) McGrath and Olinger (1996); (○) Yang et al. (2009). Note that some of the results were excluded in (*b*) due to the lack of boundary layer information.

et al., 2003; Larchevêque et al., 2003; Hassan et al., 2007; Ma et al., 2009). Therefore, it is speculated that the necessity for reducing α is likely to be caused by the overestimation of the vortex convection velocity. As such, the idea of the empirical constant α and the universal convection velocity ratio κ, which are dependent on neither geometric property nor the incoming flow characteristic, may be inadequate to explain the feedback mechanism associated with deep cavity flows.

In contrast to shallow cavities, however, the depthwise dimension of deeper cavities dictates the acoustic resonant frequency. East (1966) realized this with his experiments and proposed an empirical formula to predict the depthwise resonant frequency of deep cavities. By considering the depthwise characteristic length of the deep cavities, the formula is given by:

$$\frac{f_1 D}{a_\infty} = \frac{a}{[1 + b\,(D/L)^c]}, \tag{3.8}$$

where $a = 0.25$, $b = 0.65$ and $c = 0.75$ were determined empirically from his experiments. East (1966) highlighted that the fundamental frequency of deep cavities is highly sensitive to the aspect ratio of the cavity, which is not considered by Rossiter's formula. On the ground of this, the results from past investigations on deep rectangular cavities were gathered for comparison with the current numerical result to reconfirm this observation.

Accordingly, figure 3.14(*a*) shows that the majority of the resonant frequencies of deep cavities reside in the region close to the frequencies predicted by the classical one-quarter wave theory, with an acoustic pressure node at the cavity base and a pressure antinode near the cavity opening. This indicates that the resonant frequency of the deep cavity is primarily determined by the depth and less influenced by the streamwise characteristic length. Therefore, by a linear fit of the experiment and the current numerical results, the depthwise fundamental frequency, f_1, of deep cavities is found to be:

$$\frac{f_1 L}{a_\infty} = \frac{1}{D/L + \varepsilon_1}, \tag{3.9}$$

where $\varepsilon_1 = 0.68$, accounts for an end correction as obtained in figure 3.14(a). Subsequently, figure 3.14(b) shows the decrement of Strouhal number with the increased non-dimensional momentum thickness, which can be attributed to a reduced vortex convection speed owing to the thickened boundary layer thickness according to Yamouni et al. (2013a). By a linear fit of the experiment and the current numerical results, the relationship between the Strouhal number of the first hydrodynamic mode $f_1 L/U_\infty$ and the non-dimensional momentum thickness θ/L can be related by:

$$\frac{f_1 L}{U_\infty} = a_1 + b_1 \theta/L. \tag{3.10}$$

where $a_1 = 0.39$ and $b_1 = -0.18$ are obtained from figure 3.14(b). Accordingly, the conversion of the hydrodynamic energy to the acoustic counterpart will be maximum when Rossiter's feedback mechanism is in-phase with the depthwise acoustic resonance (East, 1966; Yang et al., 2009; Yamouni et al., 2013a). This criterion is met when the first hydrodynamic mode matches with a depthwise acoustic mode of the cavity. Therefore, a maximum oscillation will be produced when the (hydrodynamic) frequency predicted in (3.10) coincides with the (acoustic) frequency predicted in (3.9). Consequently, the critical turbulent free stream velocity at which the first hydrodynamic mode occurs concurrently with the first depthwise acoustic mode is obtained in non-dimensional form by dividing (3.9) with (3.10) as:

$$M_{\infty,cr} = \frac{1}{(4D/L + \varepsilon_1)(a_1 + b_1 \theta/L)}, \tag{3.11}$$

where the aspect ratio D/L and the upstream turbulent momentum thickness θ/L correspond to a single value of the critical free stream Mach number. Previous investigations on the deep cavity configuration have suggested that the first hydrodynamic mode often provides the most intense noise source (Erickson et al., 1986; Ziada and Shine, 1999a; Kriesels et al., 1995; Arthurs and Ziada, 2009). Appropriately, in situations where $\theta/L \leq 0.2$ is satisfied and the fundamental acoustic resonance is of interest, the prediction from (3.11) is of practical importance owing to the simplicity of the formula to predict the critical turbulent free stream velocity. This is particularly useful in minimizing the future occurrence of flow-induced resonance in the early development stage.

3.6 Effect of flow speed on hydrodynamic and acoustic modes

The analyses presented in previous sections have explored the aeroacoustic characteristics associated with a single large-scale vortical structure traversing through the opening of an orthogonal and deep cavity at a Mach number of $M_\infty = 0.2$. However, to further deepen our understanding, it is pertinent to investigate the transition to a higher hydrodynamic mode involving the presence of multiple convecting vortices at different flow velocities. Subsequently, the thesis aims to explore the intricate relationship between the vorticity-induced acoustic waves at different hydrodynamic modes and the acoustic mode within the cavity, and the possibility of a depthwise feedback process influencing this interaction. Consequently, this section focuses on elucidating the influence of flow speed on both the acoustic and hydrodynamic modes in orthogonal and deep cavity flows.

To achieve this study, two additional simulations were conducted, employing orthogonal and deep cavities with an identical geometric configuration, as illustrated in Figure 2.1. Preceding this, precursor channel simulations were performed to generate turbulent inflows at two distinct freestream velocities, namely $M_\infty = 0.1$ and $M_\infty = 0.3$, corresponding to Reynolds numbers of $Re_\infty = 87,297$ and $Re_\infty = 261,891$, respectively. Subsequently, the cavity simulations were

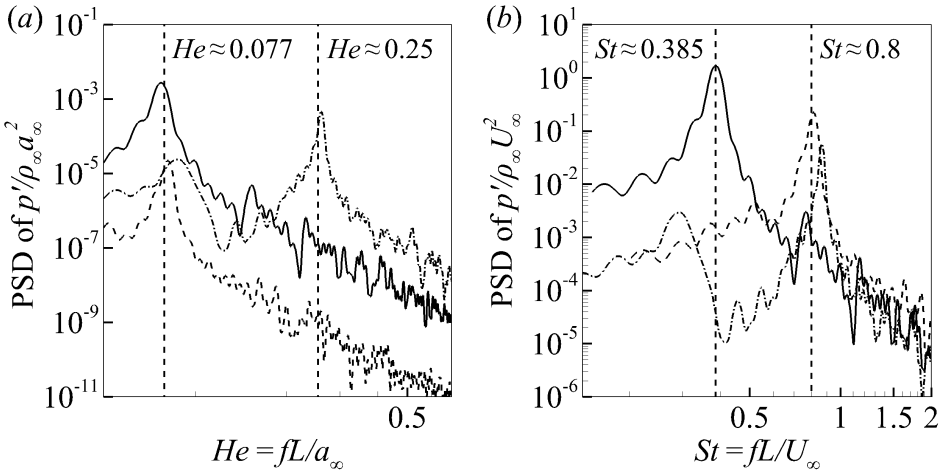

FIGURE 3.15: PSD of pressure fluctuation, p' measured on the base surface of the deep and orthogonal cavity (a), for different freestream velocity, $M_\infty = 0.1$ (- - -), $M_\infty = 0.2$ (——), and $M_\infty = 0.3$ (-···-). The measured quantities are normalised by their respective freestream velocity (b), for reasonable comparisons between cases of different flow speeds. The vertical dashed lines (- - -) indicate the tonal frequencies observed in the current cavity configurations.

carried out until a steady-periodic state of the wall pressure at the base of the cavity was attained. Following this, a Fourier transform was applied to the pressure time signal for a total non-dimensional time equivalent to approximately 13 periods of the fundamental frequency. Figure 3.15 depicts the spectra of wall pressure fluctuations measured at the base of the orthogonal and deep cavity for $M_\infty = 0.1$ and $M_\infty = 0.3$, which are then compared with the previous case of $M_\infty = 0.2$. The comparison yields several noteworthy observations.

Firstly, the pressure spectra comparison in Figure 3.15(a) demonstrates that the cavity flow at $M_\infty = 0.2$ produces the most pronounced acoustic response. The case of $M_\infty = 0.3$ follows this, while the weakest oscillation is observed in the case of $M_\infty = 0.1$. These observations suggest that the optimal acoustic response from the deep and orthogonal cavity is achieved at a flow speed of $M_\infty = 0.2$. Therefore, it is reasonable to assume that any deviation from this optimal flow speed of $M_\infty = 0.2$ attenuates the acoustic response of the orthogonal and deep cavity. Secondly, it is noteworthy that the peak Helmholtz frequencies are closely clustered around an approximate value of $fL/a_\infty \approx 0.08$, despite a decrease in flow speed from $M_\infty = 0.2$ to $M_\infty = 0.1$. Contrarily, a distinct change in oscillatory behaviour is observed when the flow speed increases to $M_\infty = 0.3$, wherein the peak frequency abruptly shifts to a higher harmonic at $fL/a_\infty \approx 0.254$, approximately three times larger than the former frequency. It is hypothesised that the increased in frequency is due to the heavily damped acoustic mode excited by the inherent instability or the broadband turbulence of the separated shear layer since it is linearly unstable to disturbances at Strouhal number smaller than $f\theta/L \leqslant 0.04$, according to Michalke (1972).

These observations demonstrate the occurrence of the ”lock-on” phenomenon, for which the peak frequency of the acoustic response synchronizes with the fundamental and second acoustic modes of the deep cavity, independent from the variation of flow speed. Similarly, figure 3.15(b) shows the pressure spectra with frequency here represented in Strouhal number. The presence of two distinct Strouhal numbers, namely $St \approx 0.385$ and $St \approx 0.8$, aids in identifying the hydrodynamic mode of the cavity oscillation. Specifically, the lower Strouhal number (e.g., $St \approx 0.385$) indicates excitation of the first hydrodynamic mode in the $M_\infty = 0.2$ case, aligning with the earlier discussions. Conversely, the second hydrodynamic mode, represented by a higher Strouhal number (e.g., $St \approx 0.8$), is excited in both the $M_\infty = 0.1$ and $M_\infty = 0.3$ cases, respectively.

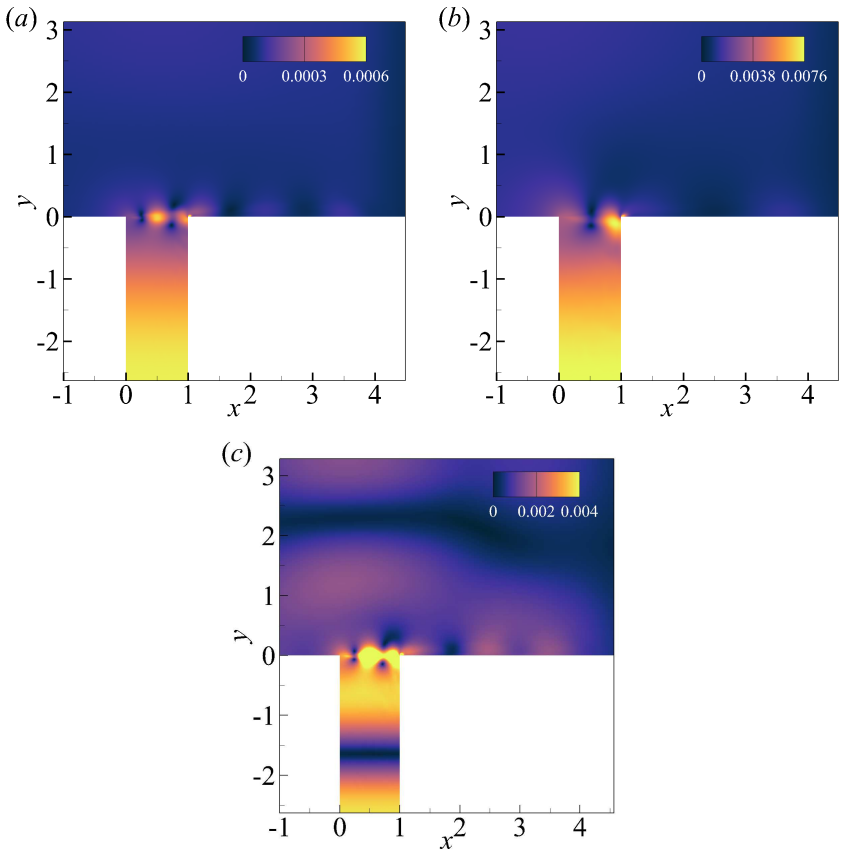

FIGURE 3.16: Contour plots of spatial variation of the magnitude of Fourier transformed pressure fluctuation, p', at three different Mach numbers: (a) $M_\infty = 0.1$; (b) $M_\infty = 0.2$; and (c) $M_\infty = 0.3$, at the respective peak frequency as shown in figure 3.15.

Figure 3.17 illustrates the comparative analysis of the magnitude and phase of the Fourier transformed pressure fluctuation across three distinct flow velocities at the tonal frequencies. Upon examining the pressure fluctuations within the cavity, it becomes evident that the first depthwise acoustic mode is sustained at flow speeds of $M_\infty = 0.1$ and $M_\infty = 0.2$, while the second depthwise acoustic mode persists at $M_\infty = 0.3$. Moreover, an examination of the phase variation of the pressure fluctuation, primarily associated with the hydrodynamic component in the proximity of the cavity opening region, reveals similarities between $M_\infty = 0.1$ and $M_\infty = 0.3$. In both instances, a shorter streamwise wavelength is observed compared to $M_\infty = 0.2$. A similar inference can also be drawn from the magnitude of the pressure fields, where the distance between the crest and trough resulting from interferences approximates the length of the oscillation wavelength. These preliminary observations suggest that the hydrodynamic mode in $M_\infty = 0.1$ and $M_\infty = 0.3$ exhibits a distinct, similar mode shape, despite the threefold increase in flow velocity from $M_\infty = 0.1$ to $M_\infty = 0.3$. Therefore, further investigation is warranted to elucidate the criterion for the onset of the corresponding mode. As a result, the subsequent analysis focuses on examining the characteristics of the hydrodynamic flow fields, with particular attention paid to the vortex dynamics near the cavity opening.

Accordingly, the Fourier transform is performed on the Q-Criterion, and the respective magnitudes for three different Mach numbers are plotted in Figure 3.20. As previously discussed, the spatial distribution of the magnitude and the streamwise phase variation of the coherent vortical structures bear close resemblance in $M_\infty = 0.1$ and $M_\infty = 0.3$ cases. In these instances, the spatial distribution of the magnitude of the Q-Criterion is primarily concentrated along the

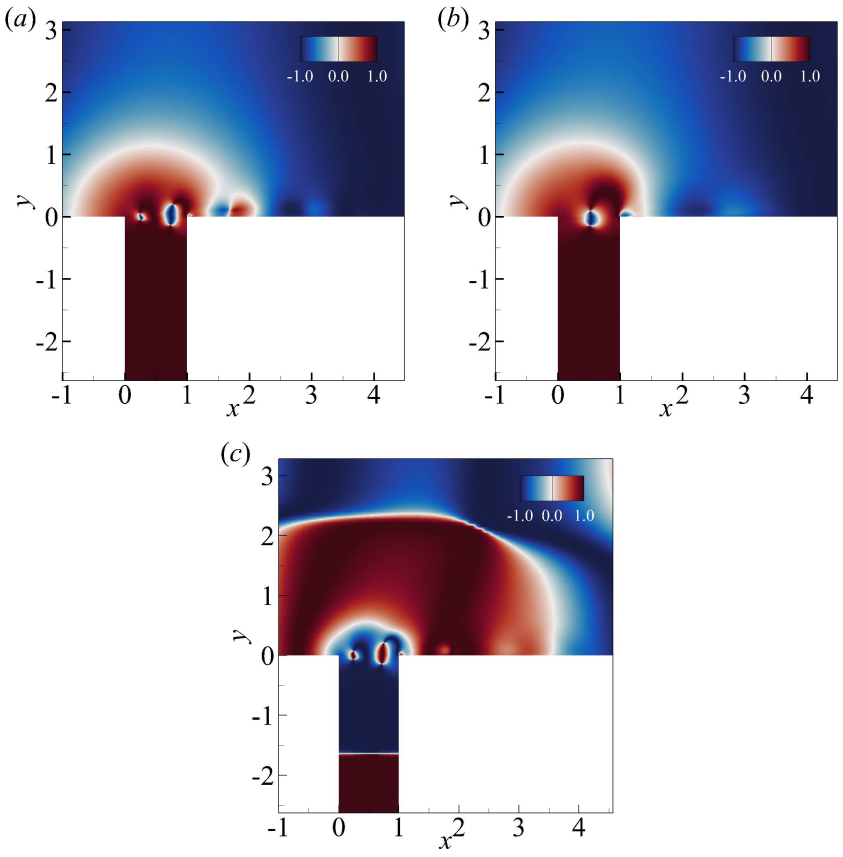

FIGURE 3.17: Contour plots of spatial variation of the cosine of the phase of Fourier transformed pressure fluctuation, p', at three different Mach numbers: (*a*) $M_\infty = 0.1$; (*b*) $M_\infty = 0.2$; and (*c*) $M_\infty = 0.3$, at the respective peak frequency as shown in figure 3.15. Note here that the phases $\Phi_{p'}$ are calculated based on the phase reference of Φ_χ.

cavity opening line (e.g., $y = 0$), indicating that the coherent vortices traverse the cavity opening region in a near-parallel fashion. Conversely, in the $M_\infty = 0.2$ case, a significant portion of the Q-Criterion's magnitude is distributed slightly below the cavity opening line ($y \leqslant 0$), implying a downward trajectory of the coherent vortex into the cavity, as depicted in Figure 3.7. These observations suggest that the first hydrodynamic mode follows a downward trajectory into the cavity, while the second hydrodynamic mode predominantly travels in parallel across the cavity opening.

To expand on this, the streamwise phase variation of Q-Criterion is examined across the cavity opening for each flow speed, and these results are presented in Figure 3.19. This study reveals that the phase variation of the coherent structures completes approximately two cycles of oscillation, that is $\Delta\Phi_Q(x, f_1) = 4\pi$ for $M_\infty = 0.1$ and $M_\infty = 0.3$, while only a single oscillation cycle is completed for $M_\infty = 0.2$ (e.g. $\Delta\Phi_Q(x, f_1) = 2\pi$). Hence, it is reconfirmed that the first hydrodynamic mode, characterized by a single vortex traversing the cavity opening, must satisfy the phase criterion for a complete oscillation cycle in $M_\infty = 0.2$. Conversely, a second hydrodynamic mode, characterized by two vortices traversing the cavity opening, must satisfy the phase criterion of two complete oscillation cycles in both $M_\infty = 0.1$ and $M_\infty = 0.3$ cases. The distinct vortex trajectories and their influence on the overall hydrodynamic behaviour are further discussed in the context of the averaged convection speed of the coherent vortical structures along the cavity opening, as calculated using the linear dispersion relation for three different flow speeds, with the results listed in Table 3.1.

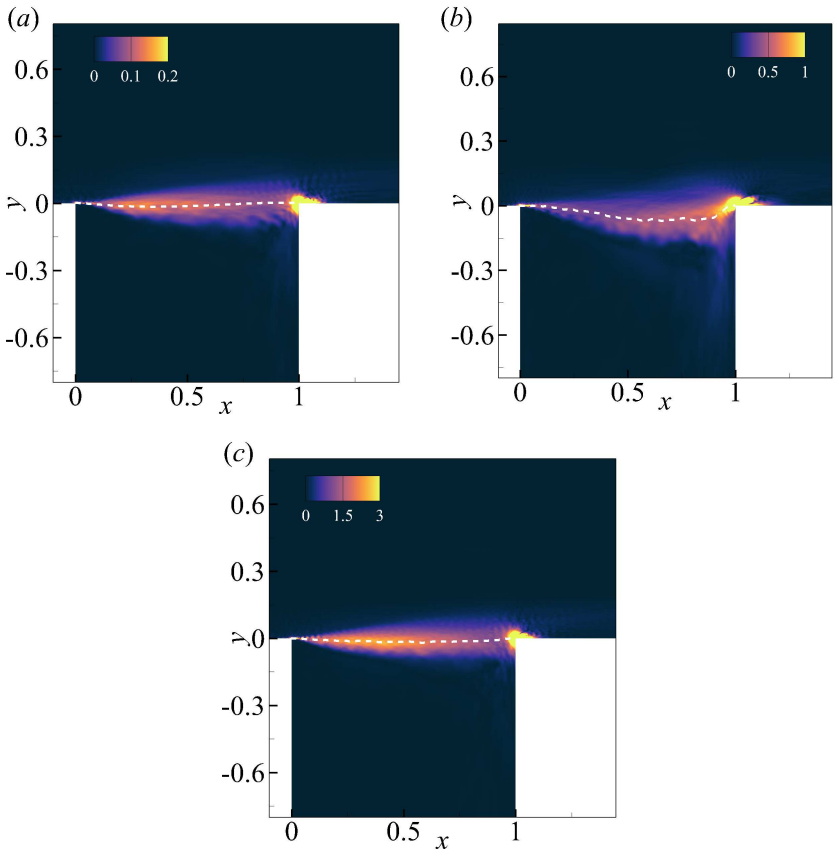

FIGURE 3.18: Contour plots of the magnitude of Fourier transform Q-Criterion, $|\Phi_Q|$ at different flow speeds: (a) $M_\infty = 0.1$, and (b) $M_\infty = 0.2$, (c) $M_\infty = 0.3$, at the respective peak frequency. Note here that the phases Φ_Q are calculated based on the phase reference of Φ_χ. The trajectory of the vortical structures is traced by monitoring the maximum value of $|Q(x,f)|$ near the cavity opening. The tracked trajectory is superimposed onto the time-averaged streamwise velocity contour plot for visual comparison.

M_∞	fL/a_∞	fL/U_∞	$\Delta\Phi_{V_H}/2\pi$	$M_c = U_c/a_\infty$	$K_c = U_c/U_\infty$
0.1	0.079	0.790	≈ 2.00	0.039	0.395
0.2	0.077	0.385	≈ 1.00	0.074	0.385
0.3	0.254	0.846	≈ 2.00	0.127	0.423

TABLE 3.1: Averaged convection speed of vortical strictures of orthogonal deep cavity at each tonal frequency calculated based the phase variation of Q-Criterion using the linear dispersion relation at three different Mach numbers.

The presented data in Table 3.1 reveals several noteworthy trends. Notably, an observation can be made that the computed convection speed ratio of the coherent vortices for each Mach number consistently falls below the hypothesized value of $K_c = 0.57$, as suggested by the well-known Rossiter's formula documented in Rossiter (1964). Instead, the calculated convection speeds of the vortices demonstrate a remarkable similarity across all examined cases, maintaining an slower average speed ratio of approximately $K_c = 0.4$. This consistency suggests the possibility of a constant averaged convection speed in orthogonal and deep cavity flows at low subsonic flow conditions, which may serve as a useful practical approximation. However,

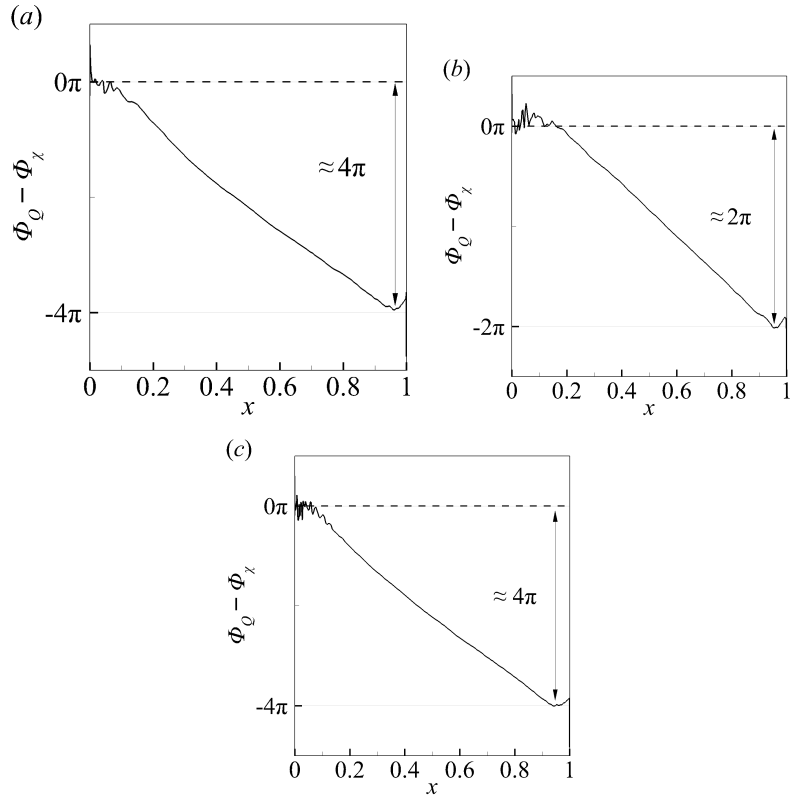

FIGURE 3.19: The streamwise phase variation of the Fourier-transformed Q-Criterion, $\Phi_Q(x,f)$, measured across the cavity opening (e.g. $y = 0$) at the respective tonal frequency for deep cavities at three different Mach numbers: (a) $M_\infty = 0.1$, and (b) $M_\infty = 0.2$, and (c) $M_\infty = 0.3$ at the respective tonal frequency. Note that the spatial variation of $\Phi_Q(x,f)$ is calculated based on the phase reference of $\Phi_\chi(x,f)$.

further investigation remains necessary to comprehend the factors influencing the observed convection speed disparities. Specifically, it is worth highlighting here that the large-scale vortex structure exhibits the slowest convection speed at $M_\infty = 0.2$. To explore the potential influence of vortex trajectory on convection speed, the local convection speed at various streamwise positions along the tracked trajectory is calculated using linear dispersion relation. Additionally, the time-averaged streamwise velocity field along the tracked trajectory is measured, as illustrated in figure 3.20. Subsequently, a comparison is made between the local convection speed and the time-averaged streamwise velocity field as a function of streamwise distance is plotted in figure 4.15.

In general, the computed local convection speed ratios demonstrate a strong alignment with the time-averaged streamwise velocity, indicating a direct influence of the spatial distribution of the time-averaged velocity on the streamwise convection speed of the coherent vortices across the cavity opening. In particular, the streamwise variation of the convection speed ratio of the coherent vortices shown in figure 4.15(a, c) yields several useful insights. For instance, it can be observed that the coherent vortices at the second hydrodynamic mode in $M_\infty = 0.1$ and $M_\infty = 0.3$ experience a similar initial deceleration, resulting in an approximate reduction of convection speed ratio to $U_c/U_\infty = 0.3$, primarily due to the separation of the shear layer near the upstream corner. Subsequently, these vortices undergo acceleration as they follow a nearly parallel trajectory, wherein the time-averaged mean flow approaches $U_\infty \approx 0.4$ just ahead of the downstream corner. This acceleration is then followed by a deceleration region as the flow impinges on the downstream corner. In contrast, the convection speed of the single large-scale

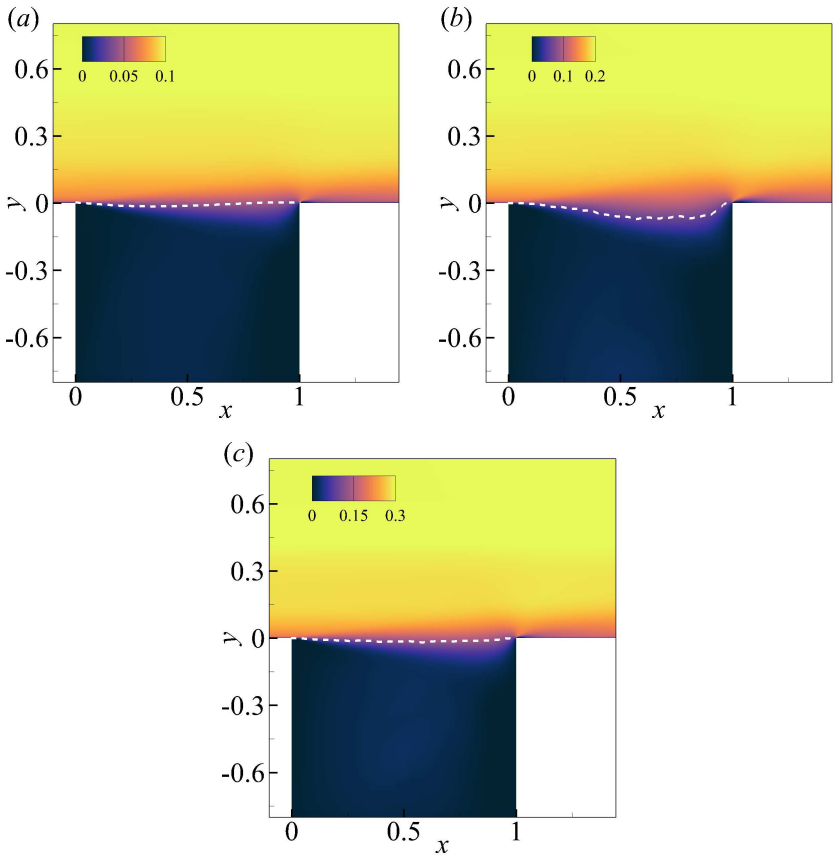

FIGURE 3.20: Contour plots of the time-averaged streamwise velocity, U at different Mach numbers: (a) $M_\infty = 0.1$, (b) $M_\infty = 0.2$, and (c) $M_\infty = 0.3$ at the respective peak frequency. The trajectory of the vortical structures is traced by monitoring the maximum value of $|Q(x,f)|$ near the cavity opening. The tracked trajectory is superimposed onto the time-averaged streamwise velocity contour plot for visual comparison.

vortex is noticeably slower, with a streamwise-averaged convection speed ratio of approximately $U_{c,avg}/U_\infty \approx 0.3$, as shown in figure 4.15(b). This reduced speed can be attributed to the absence of an acceleration region, primarily resulting from the downward trajectory of the large-scale vortex into the cavity. Hence, the convection speed of the large-scale vortex in $M_\infty = 0.2$ should, in fact, be significantly slower than the second hydrodynamic mode, thus contradicting the trend observed in Table 3.1.

On further analysis, it appears that the observed discrepancy in the calculated K_c value primarily stems from the presumption that the formation of coherent vortices occurs precisely at the upstream corner at $x = 0$ and impinge exactly on the downstream corner at $x = 1$. While the latter hypothesis is reasonably supported by the observation that coherent vortices complete an oscillation cycle upon reaching the downstream walls, the former assumption, which suggests the instantaneous formation of coherent vortices at the upstream corner at $x = 0$, warrants further investigation. To gain clarity regarding this matter, it would be beneficial to refer to Figure 3.22, which provides insight into the streamwise distribution of the cosine of the streamwise phase difference between the Q-Criterion, denoted as Φ_Q, and the acoustic force, denoted as χ, across the cavity opening. Notably, the presence of depthwise acoustic resonance induces sufficient acoustic forcing, thereby facilitating the creation of a region characterized by a constant phase near the upstream corner before the occurrence of shear layer separation (for instance, $x \leqslant 0.1$ for both the $M_\infty = 0.1$ and $M_\infty = 0.3$ cases). As a result, this region of constant phase serves as a precursor for the immediate formation of vortices near the upstream corner, thereby

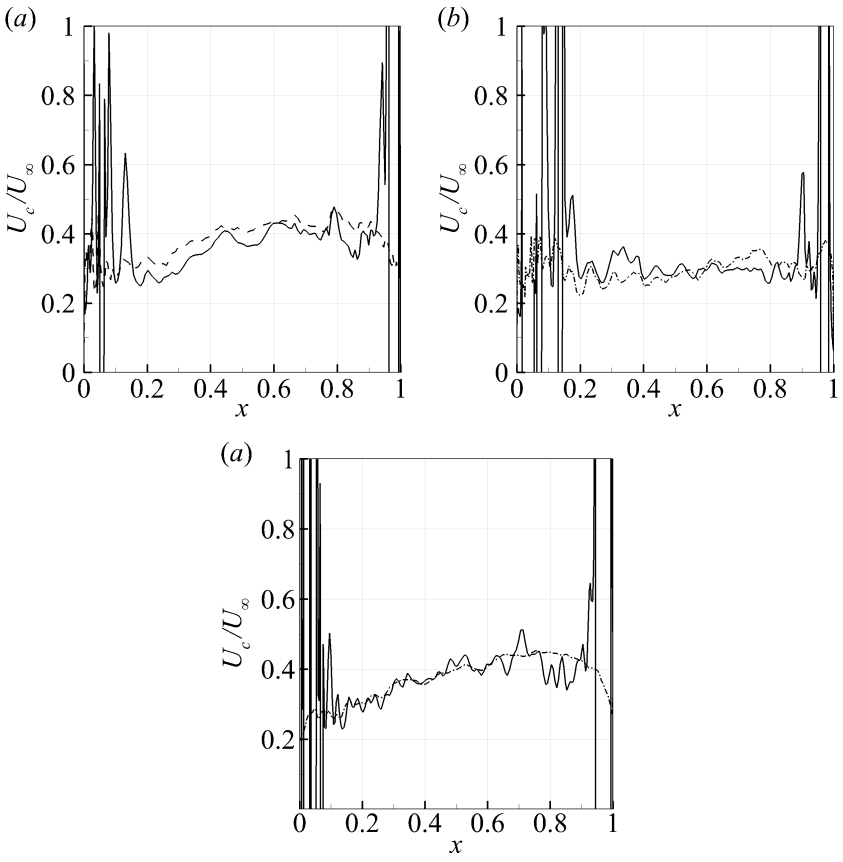

FIGURE 3.21: The local variation of the convection speed of the coherent vortices calculated using the streamwise phase variation of the Q-Criterion, Φ_Q measured across the orthogonal cavity opening in the streamwise direction at three different Mach numbers: (a) $M_\infty = 0.1$, (b) $M_\infty = 0.2$, and (c) $M_\infty = 0.3$ at the respective peak frequency. The local convection speed of the coherent vortices (——) is consistent with the respective time-averaged streamwise velocity (-···-), particularly in the region of $0.2 < x < 0.9$ before the impingement on the downstream corner. The considerable slow-down experienced by the large-scale vortical structure in $M_\infty = 0.2$ (b) illustrates the considerable variation and the influence of the time-averaged mean flow on the local convection speed of the coherent vortices.

reducing the effective streamwise travel distance required for coherent vortices to complete a full oscillation cycle. Moreover, in the case of $M_\infty = 0.2$, an even larger modulated region of constant phase is observed (e.g., $x \leqslant 0.2$), which leads to a substantial reduction in the streamwise distance required for the large-scale vortex to complete a single cycle of oscillation. In the absence of this acoustic resonance, a higher convection speed of the vortex would therefore be necessary. Consequently, the tonal oscillation observed in the $M_\infty = 0.2$ case can be attributed to the modulated region resulting from the lock-in mechanism, despite the reduced convection speed of the large-scale vortex.

Thus far, our current understanding suggests that the occurrence of cavity oscillations primarily occurs at two distinct Strouhal numbers: approximately $St \approx 0.4$ and $St \approx 0.8$, which correspond to the first and second hydrodynamic modes, respectively. However, the specific criteria that govern the transition to higher acoustic modes remain unclear. To address this knowledge gap, we conducted an eigenanalysis on the linear operator of acoustic perturbation equations (APE) to uncover the first three depthwise acoustic modes of the orthogonal and deep cavity geometry, based on the time-averaged mean flow fields derived from the LES, as illustrated in

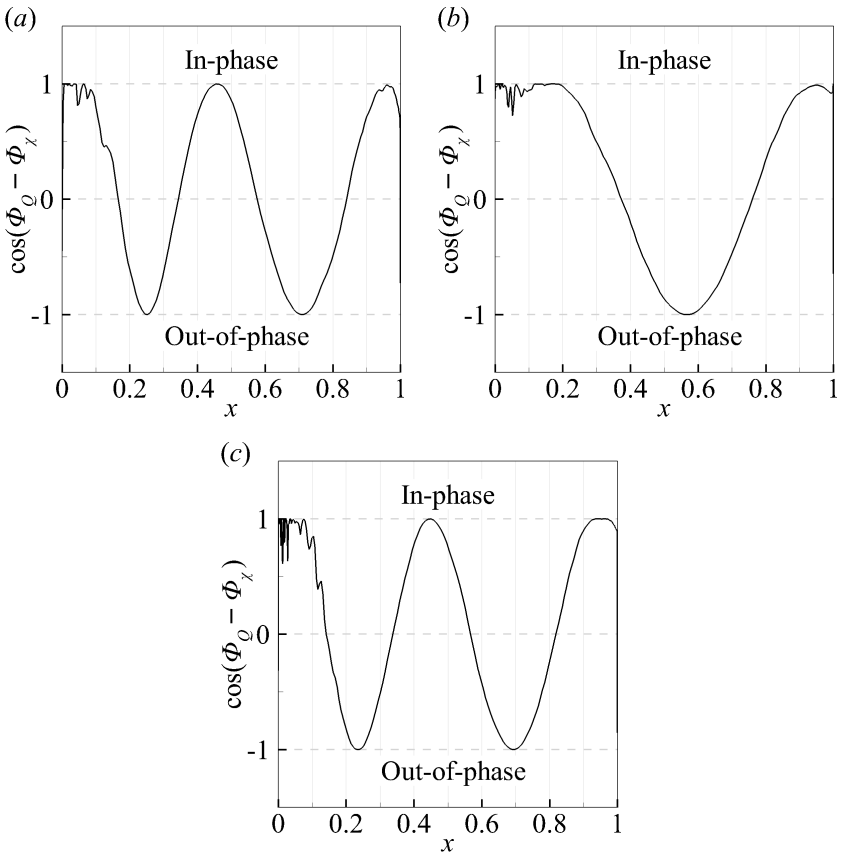

FIGURE 3.22: The unity from the cosine of the streamwise phase difference of the Q-Criterion, Φ_Q, and the acoustic force (χ) near upstream corner highlights the acoustic-coupling process in orthogonal cavity of three different Mach numbers: (a) $M_\infty = 0.1$, (b) $M_\infty = 0.2$, and (c) $M_\infty = 0.3$ at the respective peak frequency. In the most severe case, the fluid-acoustic coupling process modulates the shear layer oscillation and facilitates the formation of a region of constant phase (e.g. $x \lessapprox 0.2$ in $M_\infty = 0.2$) to reduce the effective streamwise travel distance required for the coherent vortices to complete the oscillation cycle.

Figure 3.23. The first depthwise acoustic mode, situated at a frequency of $fL/a_\infty \approx 0.08$, represents the least-damped mode (i.e., eigenvalue that is closest to the y-axis), and is insensitive to the influence of time-averaged flow fields. In contrast, the second depthwise acoustic mode is identified at a higher frequency of $fL/a_\infty \approx 0.25$ and is heavily damped (i.e., farther from the y-axis).

Equipped with the aforementioned finding, it can be postulated that the peak frequency component of the observed acoustic response in the $M_\infty = 0.2$ case primarily arises from the excitation of the least-damped fundamental acoustic mode. In particular, it is the presence of this least-damped fundamental acoustic mode that modulates the oscillation of the shear layer, thereby facilitating the subsequent formation of coherent vortex structures at the first hydrodynamic mode. Additionally, it is suggested that the presence of the fundamental acoustic mode in the $M_\infty = 0.1$ case encourages the excitation of a second hydrodynamic mode for satisfying the required phase criterion ($\Delta\Phi_Q(x, f_1) = 4\pi$). This phase criterion is necessary for completing a single oscillation cycle at the frequency fixated by the fundamental acoustic mode, while also considering the averaged vortex convection speed ratio of $K_c = U_c/U_\infty \approx 0.4$ as obtained from table 3.1. Similarly, the promotion of the second hydrodynamic mode in the cavity flow for $M_\infty = 0.3$ case is encouraged by the second acoustic mode at $fL/a_\infty \approx 0.25$ through the fluid-acoustic coupling process. Finally, it is noteworthy that the absence of a nearby acoustic mode

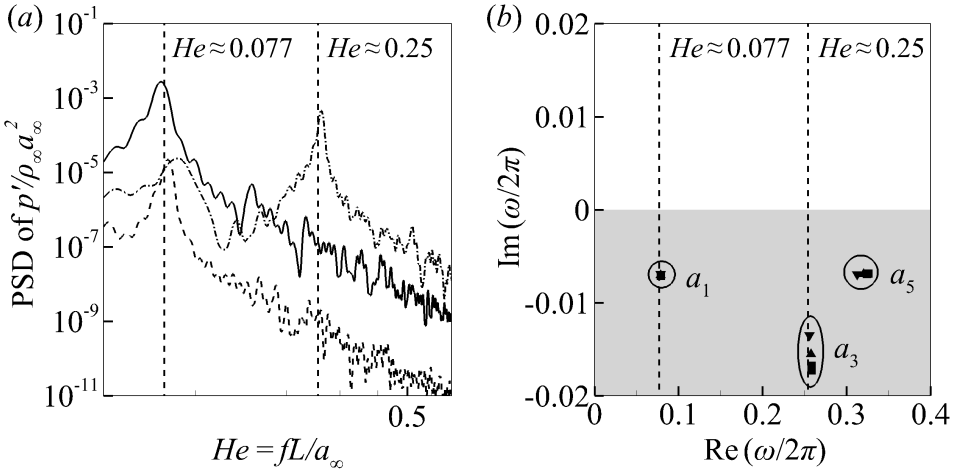

FIGURE 3.23: (*a*) PSD of pressure fluctuation, p' measured on the base surface of the deep and orthogonal cavity (*a*), for different freestream velocity, $M_\infty = 0.1$ (- - -), $M_\infty = 0.2$ (——), and $M_\infty = 0.3$ (-···-) is reproduced from figure 3.15 for direct comparison with (*b*) the first three least-damped acoustic modes obtained from the APEs at $M_\infty = 0.1$ (■), $M_\infty = 0.2$ (▲), $M_\infty = 0.3$ (▼). The vertical dashed lines (- - -) indicate the tonal frequencies observed in the current cavity configurations.

in the frequency at around $fL/a_\infty = 0.04$ and $fL/a_\infty = 0.12$ may explain the suppression of the first hydrodynamic mode in the cavity flow for the $M_\infty = 0.1$ and $M_\infty = 0.3$ cases, as previously observed in the pressure spectra.

The preceding passage extensively discusses the occurrence of tonal peaks observed in the pressure spectra at three different flow speeds. However, it is essential to gain a deeper understanding of whether the hydrodynamic modes that occur at specific Strouhal numbers (e.g., $St \approx 0.4$ and $St \approx 0.8$) can be self-sustained through streamwise feedback via pseudo-sound without the presence of depthwise acoustic resonance. To address this, a biglobal linear stability analysis of the cavity systems was performed, employing linearised Navier-Stokes equations based on time-averaged mean flow fields obtained from the LES. Two different sets of boundary conditions were applied at the cavity floor: (a) reflecting wall boundary condition and (b) anechoic non-reflecting boundary condition. Figure 3.24 demonstrates that the unstable mode obtained from the biglobal linear stability analysis with reflecting wall boundary condition agrees with the tonal peak observed in the pressure spectra in all the cases considered. Furthermore, replacing the reflecting wall boundary condition with an anechoic boundary condition at the base of the orthogonal deep cavity stabilizes the unstable mode. This observation highlights the critical role of fluid-acoustic coupling between the oscillation of the shear layer and the depthwise acoustic resonance in the deep cavity. Consequently, the self-sustained oscillation observed in orthogonal and deep cavity flows is primarily destabilized through the feedback from the depthwise acoustic resonance and not by the established view of global instability through pressure feedback from upstream propagating acoustic waves to the convective Kelvin-Helmholtz instability in the shear layer.

In addition to these insightful findings, it is also important to delve into the amplitude of cavity oscillations, as shown in the pressure spectra in Figure 3.15. Previous visualisations consistently show that fluid flows over an orthogonal and deep cavity generates highly coherent vortices. With these vortices being predominant in the subsonic flow regimes studied here, the Lamb vector (represented by $\omega \times u$) emerges as the primary noise source according to Ewert and Schröder (2003). Therefore, the spatial distribution of the magnitude of Fourier-transformed Lamb vector source term is examined near the cavity opening region at the peak frequencies

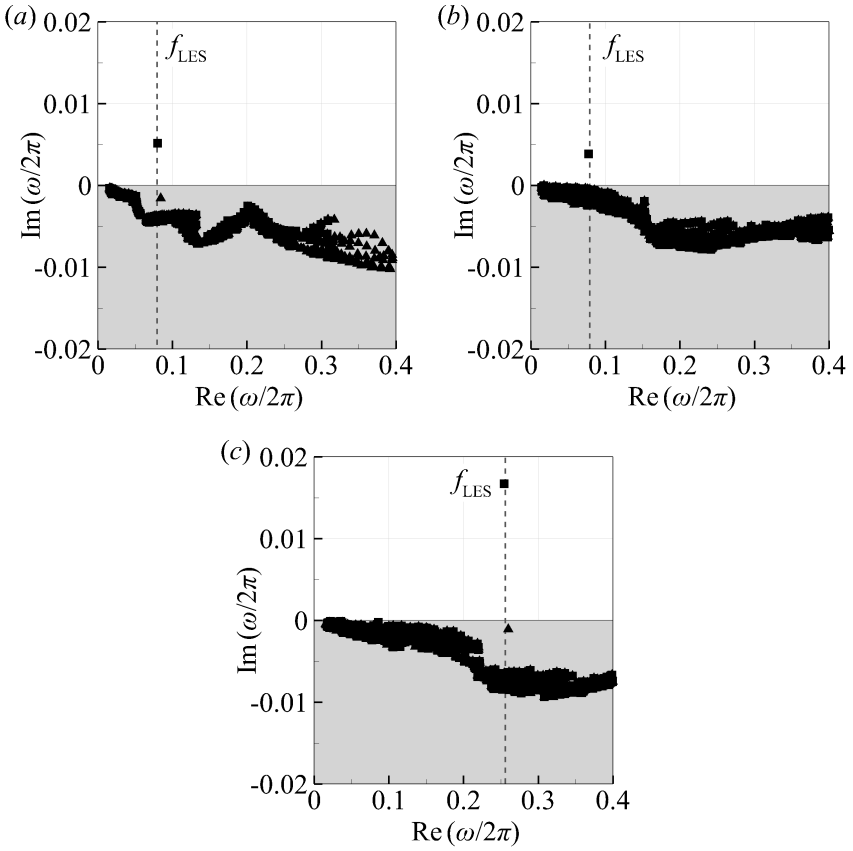

FIGURE 3.24: Eigenspectra of the linearised Navier-Stoke equations $L_{LNSE}(\bar{Q};\beta = 0)$ with acoustic resonance (■), and without acoustic resonance (▲) at $M_\infty = 0.1$ (a), $M_\infty = 0.2$ (b), $M_\infty = 0.3$ (c), respectively. The vertical dashed lines (- - -) indicate the tonal frequencies observed in the current cavity configurations.

for three different Mach number cases, as shown in Figure 3.25. The results indicate that the highest overall magnitude of the Lamb vector generated by cavity oscillation is observed in the $M_\infty = 0.3$ case. Remarkably, this finding is contrary to the peak acoustic response observed at $M_\infty = 0.2$. This discrepancy between the magnitude of Lamb vector source term and the acoustic response underscores a non-proportional direct correlation, necessitating consideration of additional analysis for clarification.

The first apparent plausible factor that leads to this discrepancy may be stemmed from a weaker amplification of the acoustic response by the third depthwise acoustic mode compared to that of the least-damped fundamental acoustic mode. It is worth recalling that the normalized pressure spectra of cavity oscillations in figure 3.15(b), showing both cases at $M_\infty = 0.1$ and $M_\infty = 0.2$, which are excited by the fundamental depthwise acoustic mode, consistently exhibit greater magnitudes than the case at $M_\infty = 0.3$ excited by the third depthwise acoustic mode. Secondly, it is suspect that the cancellation of the Lamb vector source by the opposite phase (e.g., blue and red regions) is more significant in the second hydrodynamic mode (e.g., $M_\infty = 0.1$ and $M_\infty = 0.3$), while comparably to a lesser degree in the first hydrodynamic mode (e.g., $M_\infty = 0.2$).

To validate these hypotheses, an acoustic input-output analysis was performed on the linear operator of the acoustic perturbation equations (APE) based on time-averaged flow fields obtained from the LES. The primary objective of this analysis was to obtain the acoustic amplification rate and the forcing-response mode shapes. These can be directly compute to the

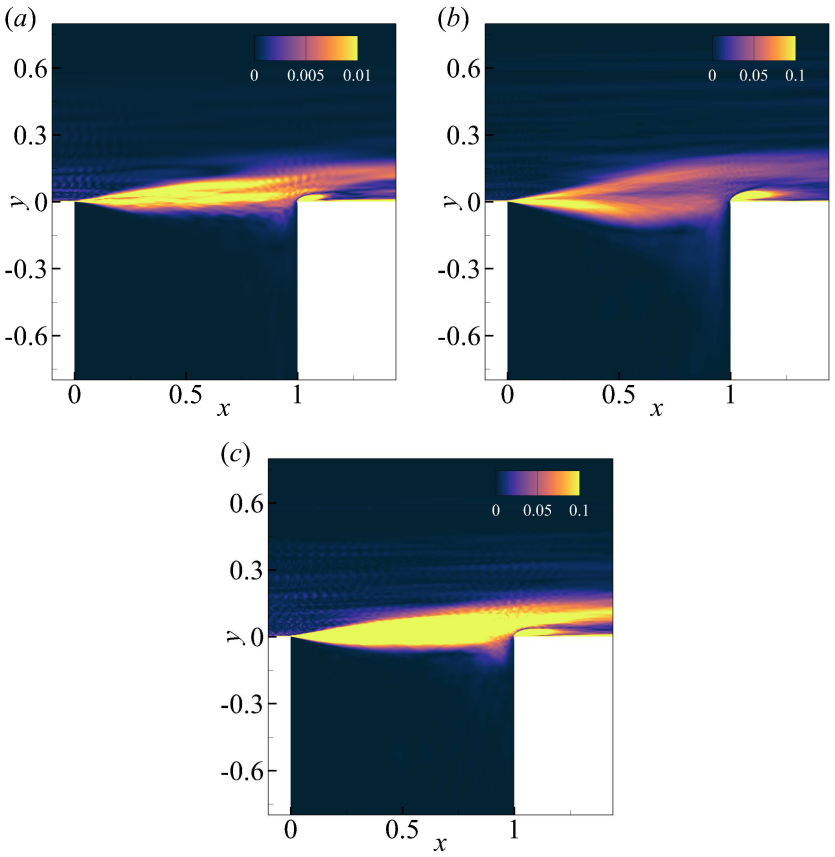

FIGURE 3.25: Contour plots of spatial variation of the magnitude of Fourier transformed Lamb vector in y-direction, $|L_y|$, at three different Mach numbers: (*a*) $M_\infty = 0.1$; (*b*) $M_\infty = 0.2$; and (*c*) $M_\infty = 0.3$, at the respective peak frequency as shown in figure 3.15.

magnitude of the acoustic response through the low-rank behaviour of the APE's linear operator, as illustrated in Figure 3.26. For a more detailed discussion on acoustic input-output analysis, readers are encouraged to consult Chapter 4. Accordingly, figure 3.28(*a*, *b*) shows the respective leading gain, σ_1 and the dot product of the optimum forcing with the Lamb vector source term obtained from the LES. Consequently, it is observed that the reduced acoustic response at $M_\infty = 0.3$ is caused directly by the reduced gain amplification due to the excitation of the damped third depthwise acoustic mode. Besides, the reduced acoustic response in the second hydrodynamic mode in both $M_\infty = 0.1$ and $M_\infty = 0.3$ cases can be explained by the reduced magnitude in the dot product of the optimum forcing and the Lamb vector source term due to a greater souce-sink cancellation, as shown in figure 3.27(*a*,*c*). Finally, the optimum acoustic response at $M_\infty = 0.2$ is facilitated by the optimum gain amplification by the first least-damped depthwise acoustic mode and the larger magnitude of the dot product of optimum forcing and the Lamb vector source term of the first hydrodynamic mode due to a lesser source-sink cancellation, as shown in figure 3.27(*b*).

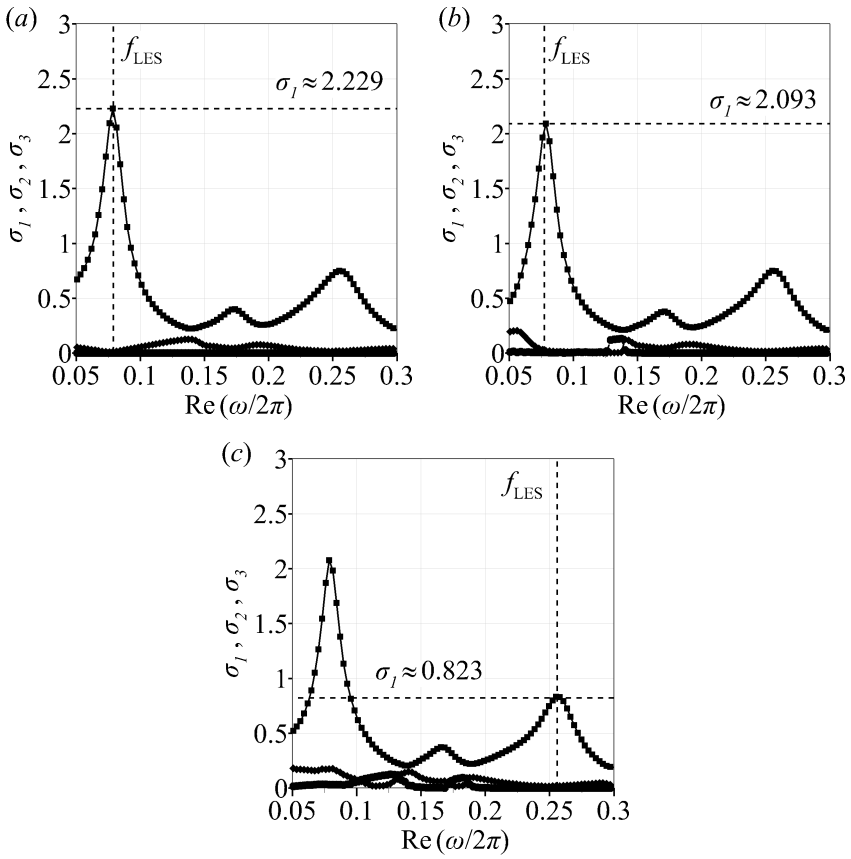

FIGURE 3.26: The low-rank behaviour of the input-output operator is visualised through the first three leading magnification rates; σ_1 (■), σ_2 (▲), and σ_3 (◆) for three different Mach numbers: (*a*) $M_\infty = 0.1$; (*b*) $M_\infty = 0.2$; and (*c*) $M_\infty = 0.3$, respectively. The vertical dashed line (- - -) indicates the tonal frequency observed in the LES, while the horizontal dashed line (- - -) represents the corresponding leading amplification rate σ_1 at that particular tonal frequency.

3.7 Summary

A detailed understanding of the physical mechanism of the aerodynamic noise generation of a deep cavity in acoustic resonance with an aspect ratio of $D/L = 2.632$ at $Re_\infty = 174{,}594$ subjected to an incoming turbulent boundary layer at a free stream velocity of $M_\infty = 0.2$ has been achieved by using a high-order accurate large-eddy simulation. The first part of the investigation concerns pressure fluctuations around the cavity that are separated into the hydrodynamic and the acoustic components using Doak's MPT. Accordingly, the decomposed acoustic pressure fluctuation illustrates the instant alteration of acoustic pressure fluctuation inside the cavity with a synchronised shear layer oscillation across the cavity opening. Furthermore, the decomposed hydrodynamic pressure field captured the formation of a large-scale low-pressure region from the small-scale low-pressure spots near the upstream corner and its eventual impingement onto the downstream corner. In addition, the Fourier transformed hydrodynamic pressure fluctuation near the cavity opening indicates that the number of vortices (e.g. hydrodynamic mode) increases following the passage frequencies, and the respective streamwise amplification at each tonal frequency across the cavity opening through the coherent vortex formation is visualised. The formation of the separation region caused by the flow reversal and the mass exchange rate across the cavity opening could also help describe the aerodynamic noise generation.

The current work studied the fluid–acoustic coupling mechanism between the separated shear layer oscillation near the upstream corner and the acoustic resonance in the cavity. It is found

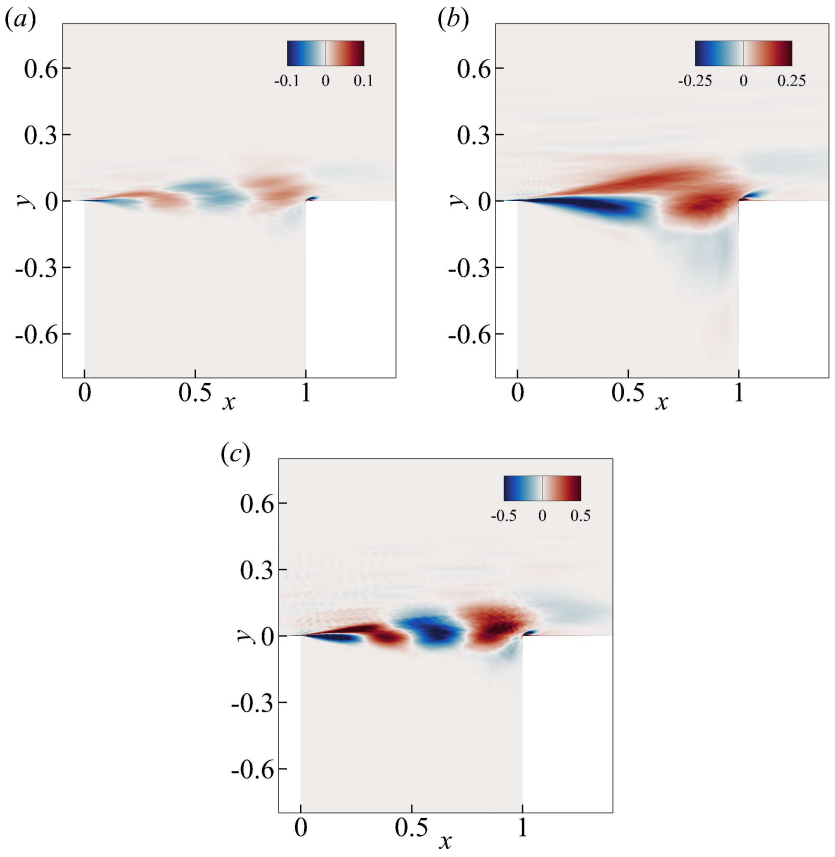

FIGURE 3.27: The spatial distribution of the real part of the component-wise multiplication between the leading optimal forcing mode, v_1, and the input forcing, $\hat{f}_\omega$, in the streamwise direction (top row of the contour plots) and the vertical direction (bottom row of the contour plots) for three different Mach numbers: (*a*) $M_\infty = 0.1$; (*b*) $M_\infty = 0.2$; and (*c*) $M_\infty = 0.3$, respectively. Note that the phase of the cycle (as shown in the contour plots) is selected such that the imaginary part of the integrated volume forcing is zero to accentuate the source-sink cancellation effect.

that the vertical velocity fluctuation is mostly in-phase with the acoustic forcing near the upstream corner, highlighting the efficient fluid-acoustic coupling process. It is observed that the non-linear interactions between the vertical velocity fluctuation at higher harmonics and the fundamental acoustic resonance are plausible. Thus, this may indicate that the birth of higher harmonics may result from the 'modulated instability wave' by the strong acoustic forcing at the fundamental frequency. The next part of the study estimated the averaged convection speed of the coherent vortices across the cavity opening, which is determined by calculating the phase variation of the Q-criterion from upstream to the downstream corner of the cavity. Finally, a semi-empirical model to predict the critical free stream velocity at which a strong fluid-acoustic coupling occurs, as a function of cavity geometry and inflow boundary-layer property, is proposed. This is particularly useful in predicting the future occurrence of flow-induced resonance in the early development stage.

Following up on this, the last part of the study investigated the influence of flow speed on fluid-acoustic resonance in an orthogonal and deep cavity. The results revealed that the self-sustained oscillation produces a varying magnitude in acoustic response and excites distinct hydrodynamic and acoustic modes at three different flow speeds. Specifically, it was reaffirmed that the most intense oscillation occurs at $M_\infty = 0.2$. The attenuated response at other speeds, especially $M_\infty = 0.3$ is directly attributed to the diminished gain amplification resulting from the

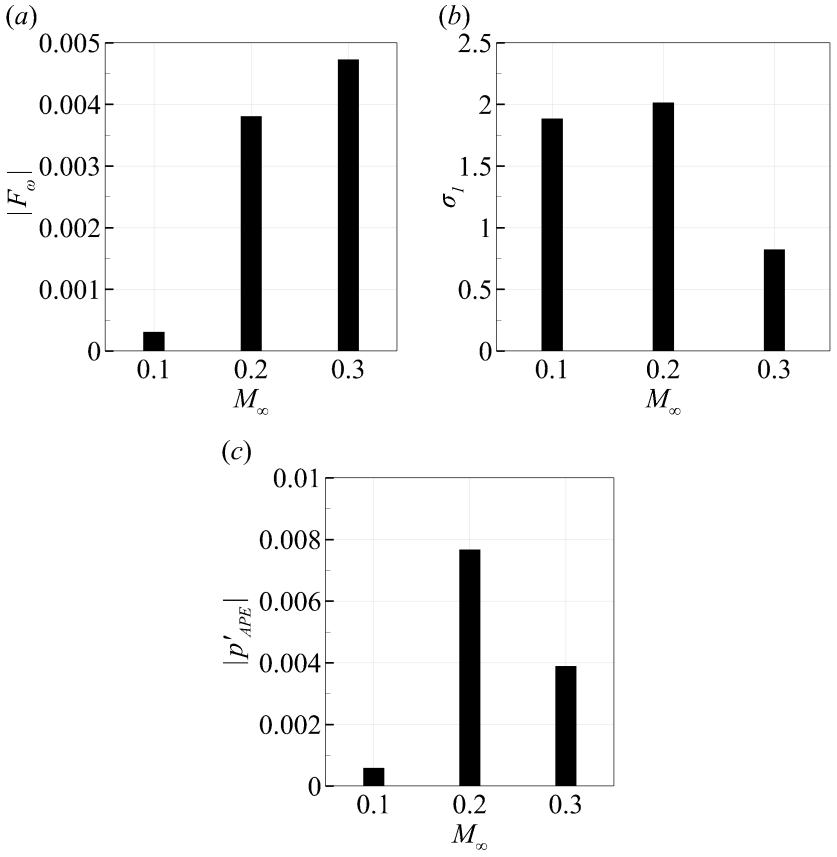

FIGURE 3.28: (*a*) The magnitude of the integrated volume forcing, represented by $|F\omega|$, and (*b*) The first leading gain, denoted as σ_1, of the input-output operator of the APEs. (*c*) The reconstructed acoustic response measured at the cavity base, $|p'_{APE}|$, is obtained from the 1-rank approximation computed using equation (4.11).

excitation of the highly damped third depthwise acoustic mode. Moreover, in both $M_\infty = 0.1$ and $M_\infty = 0.3$ cases, the reduced acoustic response can be explained by a greater source-sink cancellation of the second hydrodynamic mode. Conversely, at $M_\infty = 0.2$, the optimal acoustic response is facilitated by the highest gain amplification achieved by the least-damped depthwise fundamental acoustic mode, along with reduced source-sink cancellation of the first hydrodynamic mode. Additionally, the destabilising role of acoustic resonances in deep cavity flows is highlighted using biglobal linear stability, where it was demonstrated that the eigenmodes are effectively stabilised when an anechoic boundary condition was replaced at the bottom wall of the deep cavity.

Chapter 4

Flow-acoustic resonance in inclined and deep cavities

This section presents numerical investigations of flow-acoustic resonance in inclined and deep cavities using wall-resolved large-eddy simulations. The study focuses on cavities with an aspect ratio of $D/L = 2.632$ under three different inclination angles ($\alpha = 90^\circ$, 60°, and 30°). Additionally, two Mach numbers, 0.2 and 0.3, are considered in this section, with particular emphasis on the intriguing behaviours exhibited by inclined cavities at $M_\infty = 0.3$. A fully turbulent boundary layer generated from an independent precursor simulation is employed upstream of the cavities. The momentum thickness of the turbulent boundary layer is $\theta/L = 0.030$. The initial results from these simulations suggest a significant difference in the flow-acoustic resonance characteristics between the inclined and orthogonal cavities despite their identical aspect ratio and inflow condition used. The discrepancy is especially pronounced at $M_\infty = 0.3$, where the inclined cavities produce significantly stronger resonance, and the peak frequency ($St \approx 0.27$) is considerably lower compared to the orthogonal cavity configuration. Notably, this Strouhal number of $St \approx 0.27$ was neither accounted for by Rossiter (1964), nor was it predicted by the semi-empirical formula proposed in Chapter 3. This study employs acoustic input-output and linear stability analyses to account for the newly observed aeroacoustic behaviours. The acoustic input-output analysis reveals that the inclined cavities yield stronger acoustic responses due to the higher amplification rate of the least-damped acoustic mode and reduced source-sink cancellation of the first hydrodynamic mode. Furthermore, the linear stability analysis identifies the most unstable mode within the inclined cavity systems, pinpointing the region slightly downstream of the separation corner as particularly susceptible to hydrodynamic instabilities. Based on these observations with existing experimental evidence, we suggest that the amplified flow-acoustic resonances in inclined cavities at $St \approx 0.27$ could be linked to a low-frequency extension of the first hydrodynamic mode through the enhanced shear layer undulation when the acoustic particle displacement is comparable to the momentum thickness.

4.1 Pressure fluctuations and oscillation frequencies

The self-sustained oscillation observed in inclined and deep cavities is a fluid-resonant oscillation in which the shear layer oscillation couples with an acoustic mode of the cavity to reinforce large-scale vortical structures, thereby altering the flow field and generating highly intense acoustic pressure fluctuations. This process involves the efficient conversion of local flow energy into acoustic energy, as visualised in Figure 4.1.

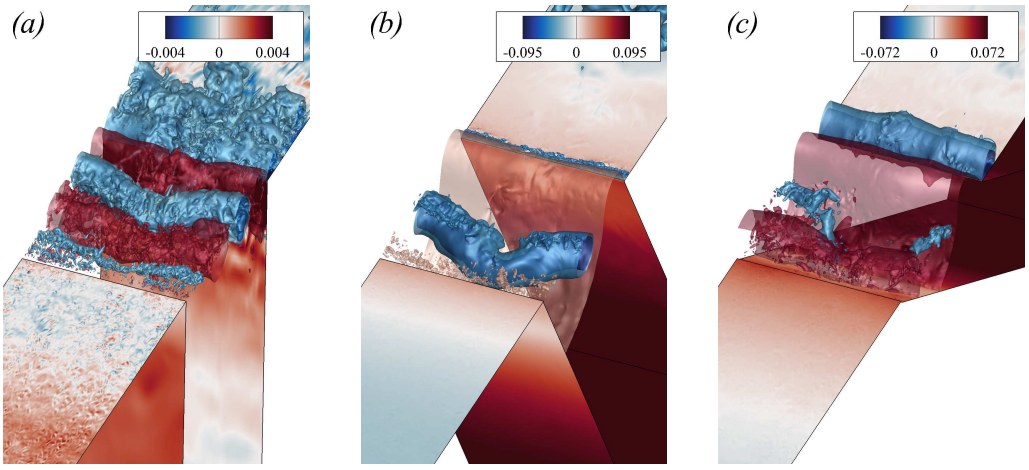

FIGURE 4.1: The large-scale vortical structures are identified through iso-contours of instantaneous pressure fluctuations. Note that the flow direction is from left to right. The surface contours of wall-pressure fluctuations reveal the prominent acoustic field emanating from deep cavities with the inclination angles of $\alpha = 90^\circ$ (a), 60° (b), and 30° (c), respectively.

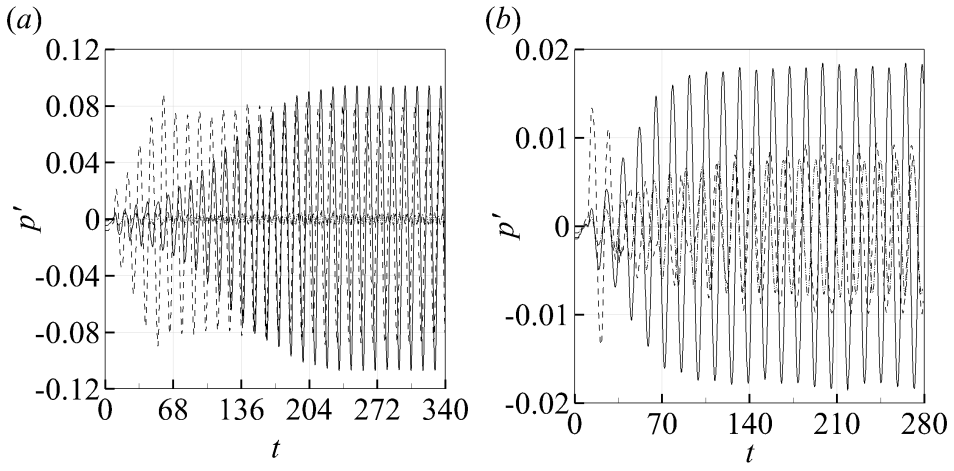

FIGURE 4.2: The spanwise-averaged time signal of the pressure fluctuations measured on the base surface of the deep cavities with the inclinations: $\alpha = 90^\circ$ (-···-), 60° (——), and 30° (- - -). The measurements were recorded at free-stream Mach numbers of $M_\infty = 0.3$ (a) and $M_\infty = 0.2$ (b), respectively.

This section investigates the aeroacoustic behaviour of wall-pressure fluctuations in deep cavities subjected to three distinct inclination angles at two specific Mach numbers, resulting in a total of six simulations. Initially, simulations are conducted at a Mach number of $M_\infty = 0.3$ for four million time steps, corresponding to 220 non-dimensional time units. Subsequent to this period, a steady-periodic state of the wall-pressure signal is achieved at the base of the cavity in all inclinations, as shown in Figure 4.2(a). Accordingly, the Fourier transform is performed on the pressure time signals using an additional non-dimensional time of approximately 740 samples (every 0.164-time unit) of the computational data over a total duration of a non-dimensional time of 120, encompassing around ten periods of the lowest fundamental frequency. The resulting time signals are approximately periodic, and any steady component is removed prior to the Fourier transform. Different windowing functions have been attempted, and the results show comparable spectrum compositions. Subsequently, the simulation procedures are repeated using a turbulent inflow dataset at a Mach number of $M_\infty = 0.2$ as discussed in Chapter 3, and the

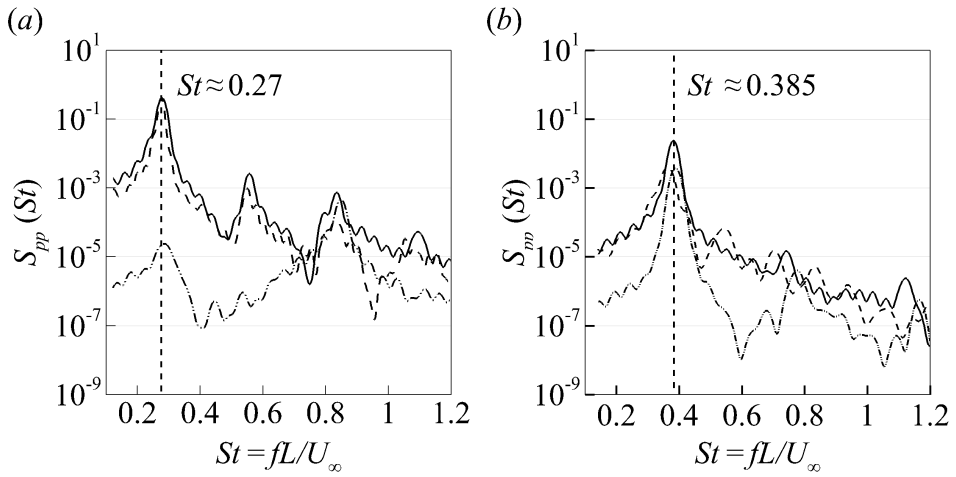

FIGURE 4.3: Power spectral density (PSD) of the spanwise-averaged time signal of wall-pressure fluctuations measured on the base surface of the deep cavities with the inclinations: $\alpha = 90^\circ$ (-···-), 60° (——), and 30° (- - -) at free-stream Mach numbers, $M_\infty = 0.3$ (a), and $M_\infty = 0.2$ (b), respectively.

corresponding time signal of the acoustic responses from each inclination is presented in Figure 4.2(b). Evidently, the pressure signals from the cavities clearly display periodic oscillations, underscoring the self-sustaining nature of inclined and deep cavity flows at both $M_\infty = 0.2$ and $M_\infty = 0.3$.

The power spectra of wall-pressure fluctuations at $M_\infty = 0.2$ are depicted in figure 4.3(b). The figure illustrates that each cavity case ($\alpha = 30^\circ$, 60°, and 90°) exhibits a primary resonance at the fundamental frequency ($St \approx 0.385$), which is closely related to the first Rossiter mode as predicted by the Rossiter semi-empirical formula proposed in Rossiter (1964). Previously, the optimal Mach number for the orthogonal cavity geometry ($D/L = 2.632$) with the inflow condition ($\theta/L = 0.0345$) was believed to be $M_\infty = 0.2$, a conclusion drawn from discussions in Chapter 3. Accordingly, this optimal condition was understood to represents a lock-in event between the Rossiter's streamwise feedback and the depthwise acoustic resonance mode. Therefore, any deviation from this Mach number was anticipated to produce a less optimal acoustic response. This assumption was indeed corroborated by the attenuated acoustic response observed in the orthogonal cavity at $M_\infty = 0.3$, as shown in figure 4.3(a). On the contrary, the oscillations in inclined cavities at $M_\infty = 0.3$ displayed an entirely unexpected behaviour. Firstly, the strongest peak frequency shifted to a lower value of $St = 0.27$ in the inclined cases ($\alpha = 30^\circ$ and 60°). It is noteworthy that previous studies on orthogonal deep cavities (Yang et al., 2009) and on closed side branches (Peters, 1993a; Ziada, 1994; Dequand et al., 2003) also reported a critical resonance occurring at $St \approx 0.27$, which do not follow the existing flow-acoustic resonance theories. More strikingly, the inclined cavities at $M_\infty = 0.3$ demonstrated a significant increase in the peak amplitude by nearly 30dB stronger than the orthogonal cavity configuration. This enhanced amplitude even surpassed that seen under what was previously deemed the "optimal" condition for orthogonal cavity at $M_\infty = 0.2$, as evident in Figure 4.3. Herein, the primary objective of this paper is to delve into the physical mechanisms underlying these unexpected and pronounced acoustic responses from the inclined cavities at $M_\infty = 0.3$.

Figure 4.4 shows snapshots of the spanwise-averaged instantaneous pressure fluctuations captured at four points in time separated by $T/4$, where $T = 1/f_p$ is the period of the oscillation at the tonal frequency observed in the pressure spectra shown in Figure 4.3(a). The snapshots illustrate how the shear layer deflection synchronises with the instantaneous pressure fluctuations in inclined and deep cavities. For brevity, the subsequent analysis will primarily focus on the time

variation of the instantaneous pressure fluctuations in the $\alpha = 60^\circ$ inclined cavity. Accordingly, valuable discussions on the visualisations presented in Figure 4.4 can be made regarding the acoustic pressure averaged over the bottom surface of the inclined cavity, which is determined as:

$$\chi(t) = \frac{1}{A_b} \int_{A_b} p'(x_b, t) \mathrm{d}A, \tag{4.1}$$

where x_b and A_b denote the Cartesian coordinates on the surface area of the cavity base, respectively.

Figure 4.4(a) shows the beginning of an oscillation cycle of χ, during which a distinct large-scale vortex is located slightly above the cavity opening as revealed by the low-pressure zone near the downstream corner. At this juncture, a nearly complete destructive interference transpires between the reflected compressive waves and the incident rarefaction acoustic waves, resulting in an acoustic pressure equilibrium within the cavity (i.e., $\chi = 0$). Subsequently, the initial downward deflection of the shear layer becomes apparent, accompanied by the emergence of individualised low-pressure regions close to the upstream corner. The former occurrence denotes the inception of constructive interference of rarefaction acoustic waves within the cavity, while the latter event signifies the generation of small-scale vortices near the upstream corner.

As the large-scale vortical structure continues its movement beyond the downstream wall, the vortex-corner interaction becomes more pronounced, generating further rarefaction waves. These waves interfere constructively with the rarefaction waves reflected off from the base of the cavity, resulting in a further reduction of the acoustic pressure fluctuations within the cavity until the acoustic pressure exerted on the cavity base reaches its minimum value, as depicted in Figure 4.4(b). Following this, a distinct low-pressure region is observed near the upstream corner from the merging of newly formed vortices with the downward deflection of the shear layer. At this point, the gradual emergence of a localised and non-negative pressure region close to the downstream corner is observed. This observation is attributed to the impeded shear layer, which indicates the onset of stagnated flows.

As the flow field is severely retarded by the downstream corner, a highly stagnated region is established, and this is accompanied by an increase in pressure fluctuations near the downstream corner, as illustrated in figure 4.4(c). At this instant, a complete destructive interference transpires between the incident compressive acoustic waves and the rarefaction waves reflected from the base of the cavity. Subsequently, recurrent constructive interferences occur within the cavity until the averaged acoustic wall-pressure χ exerted on the cavity base reaches its maximum value due to the complete constructive interference of compressive acoustic waves, as shown in figure 4.4(d). As the shear layer gradually detaches from the downstream corner, the flow stagnation lessens. A complete destructive interference ensues as the large-scale vortex convects downstream and slowly ejects out from the cavity, thereby completing a single oscillation cycle of χ.

The preceding discussions implicitly discern two distinct regions of pressure fluctuations, namely, the local hydrodynamic fluctuation near the cavity opening and the acoustic fluctuation enveloping the cavity. The difference between the two components is further elucidated by the magnitude and phase distributions of the Fourier-transformed pressure fluctuations. Accordingly, figure 4.5 reveals that the pressure field in the interior of the cavity appears to be primarily stationary (e.g. constant phase), with a maximum magnitude (e.g. a pressure node) positioned at the cavity base in all inclinations. These observations align with the inherent nature of depthwise acoustic resonances, thereby confirming that the pressure field in the interior of the cavity is primarily associated with a depthwise acoustic resonance. Furthermore, the depthwise acoustic resonances observed in this study are highly localised in the cavities and are consistent with the definition of "trapped acoustic mode" (Koch, 2005). It is worth pointing out that the presence

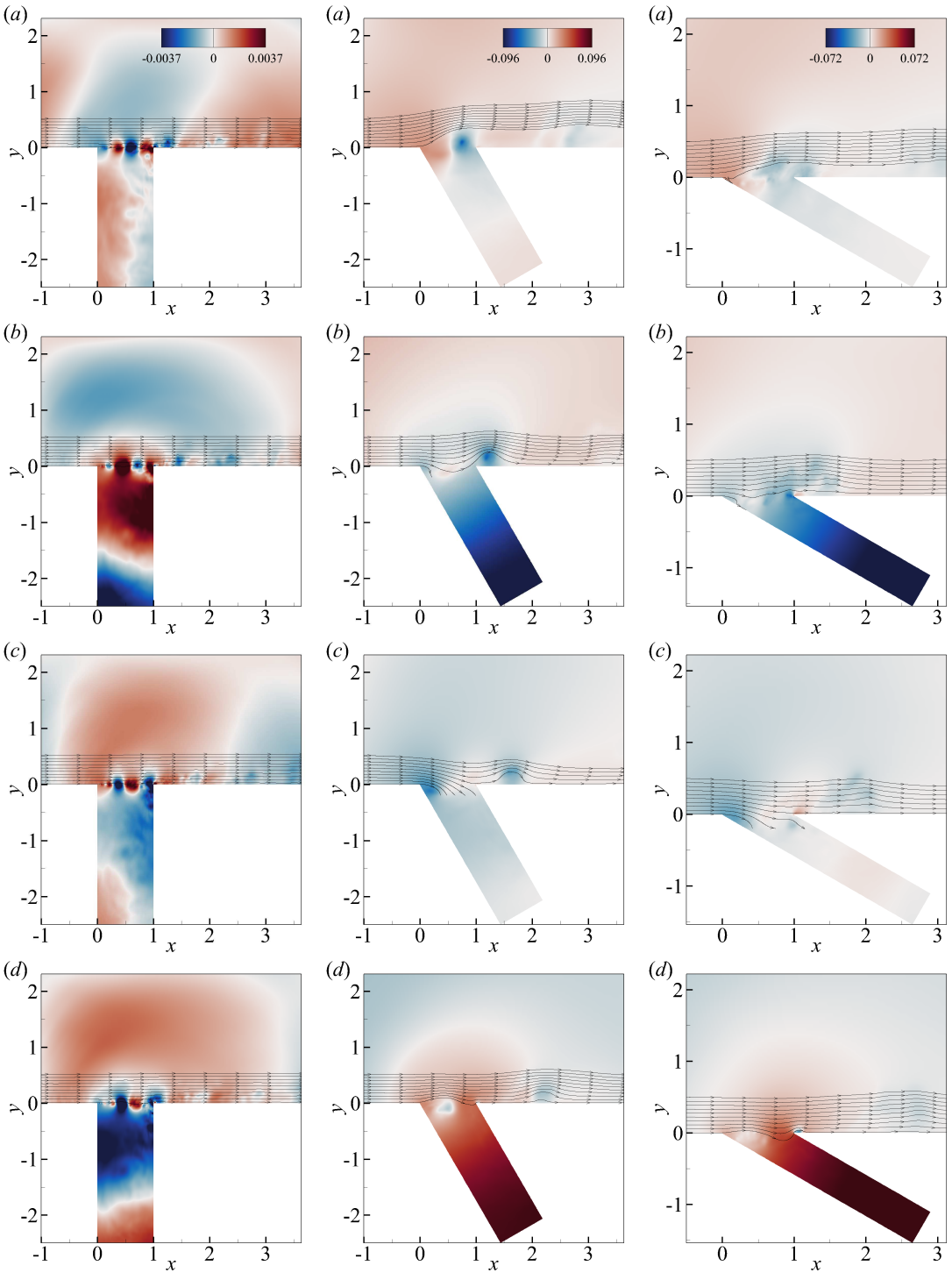

FIGURE 4.4: Snapshots of the spanwise-averaged instantaneous pressure fluctuations with superimposed streamlines to signify the shear layer undulation across the cavity opening with a time interval of $T/4$ between two successive plots from (a) to (d), where T is the period of the oscillation cycle of χ. The first, second and third columns correspond to deep cavities with the inclinations: $\alpha = 90°$, $\alpha = 60°$ and $\alpha = 30°$, respectively.

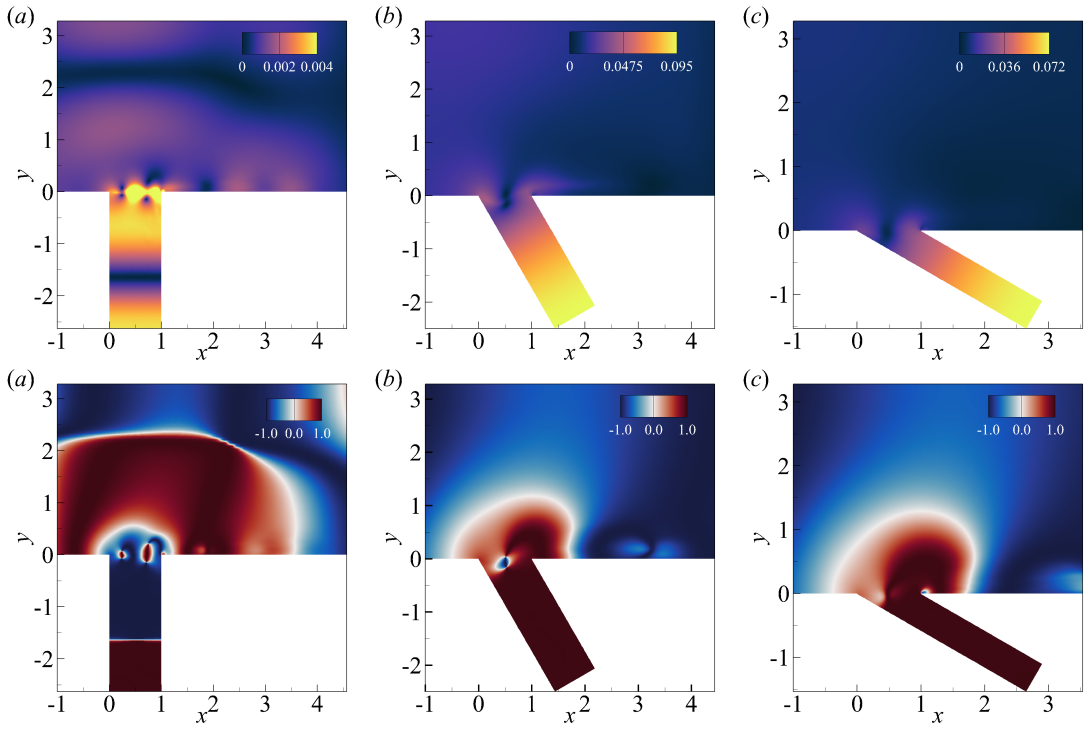

FIGURE 4.5: The spatial distribution of the Fourier-transformed pressure fluctuations at the tonal frequency for deep cavities with the inclinations: $\alpha = 90^\circ$ (a), $\alpha = 60^\circ$ (b), $\alpha = 30^\circ$ (c), respectively. The top row of the contour plots represent the magnitude, $|p'|$, while the bottom row of the contour plots represent the cosine of the phase, $\cos(\Phi_{p'}(x,f) - \Phi_\chi(x,f))$. Note that $\Phi_\chi(x,f)$ represents the phase of the Fourier transform of χ defined in (4.1).

of hydrodynamic modes can be discerned near the cavity opening by the streamwise phase shift of the pressure fluctuations due to the convective nature of the vortices.

To facilitate investigations, we decompose the pressure fluctuations around the cavity into their hydrodynamic and acoustic components using momentum potential theory (MPT) developed by Doak (1989). Essentially, Doak's MPT separates the momentum density, ρu, into rotational and irrotational components through a Helmholtz decomposition. Then, the momentum equation in terms of the hydrodynamic and acoustic components is obtained as:

$$\frac{\partial}{\partial t}(B - \nabla\psi) + \nabla \cdot \left[\frac{(B - \nabla\psi)(B - \nabla\psi)}{\rho} - \tau_{ij} \right] + \nabla p = 0. \tag{4.2}$$

By taking the divergence of (4.2), the Poisson equation for the hydrodynamic pressure fluctuations, p'_H:

$$\nabla^2 p'_H = S_H + \tilde{S_H}, \tag{4.3}$$

and the Poisson equation for the acoustic pressure fluctuations, p'_A:

$$\nabla^2 p'_A = S_A + \tilde{S_A}, \tag{4.4}$$

are derived. Accordingly, the hydrodynamic and acoustic pressure fluctuations are obtained by solving the Poisson equations in (4.3) and (4.4), respectively. The numerical implementation is described extensively in Unnikrishnan and Gaitonde (2016); Ho and Kim (2021b) and the evaluations of the linear (S_H and S_A) and the non-linear source terms ($\tilde{S_H}$ and $\tilde{S_A}$) are detailed in Unnikrishnan and Gaitonde (2020), which are not repeated here for brevity.

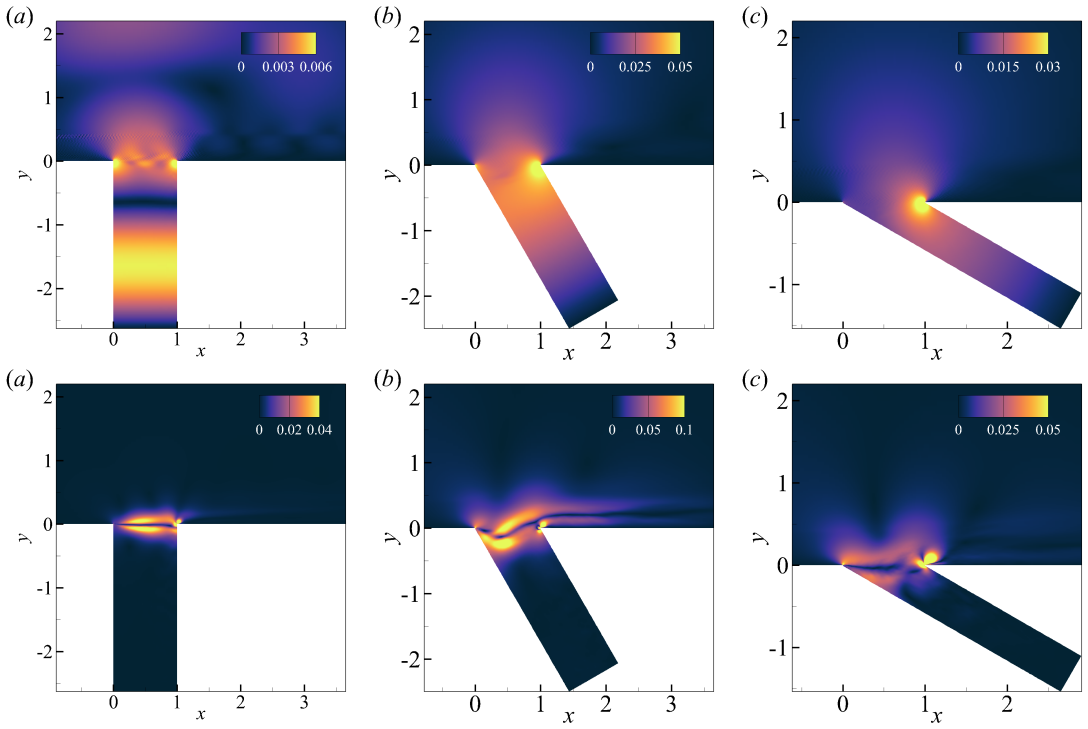

FIGURE 4.6: The top row of the contour plots represents the spatial distribution of the magnitude of decomposed Fourier-transformed pressure gradient associated with the hydrodynamic component $|\partial p_H/\partial y|(x,f)$, while the bottom row of the contour plots shows the respective acoustic component $|\partial p_A/\partial y|(x,f)$, at their respective tonal frequencies for deep cavities with the inclinations: $\alpha = 90^\circ$ (a), $\alpha = 60^\circ$ (b), $\alpha = 30^\circ$ (c), accordingly.

Figure 4.6 shows the pressure gradients in hydrodynamic and acoustic components, and their spatial distribution between orthogonal and inclined cavities exhibits striking disparities. In particular, the acoustic pressure gradient appears to be more concentrated near the downstream corner in inclined cavities, while the acoustic pressure gradient is symmetrically distributed in the orthogonal cavity. This discrepancy in the spatial distribution of the acoustic pressure gradient is a critical observation in elucidating the noise generation process, as later discussed in section 4.4. Furthermore, the difference in magnitude insinuates that the resonant acoustic field within inclined cavities may exhibit a more significant acoustic particle velocity than the orthogonal cavity. In light of this, the induced acoustic particle velocity along the cavity opening region is approximated as being proportional to the acoustic pressure gradient using isentropic Euler equations (Rienstra, 2015), as expressed by:

$$\frac{dv_a}{dt} = -\frac{1}{\rho}\frac{\partial p_a}{\partial y}, \tag{4.5}$$

where $\tilde{v}_a$ represents the estimated acoustic particle velocity and p_a is the decomposed acoustic pressure field. By considering a modal fluctuation of the acoustic pressure and spatially averaging the acoustic particle velocity across the cavity opening, we obtain an averaged acoustic particle velocity that oscillates through the cavity opening, as given by:

$$\overline{v_a} = \frac{1}{L}\int_{x=0}^{x=L} \frac{1}{2\pi f}\frac{\partial p_a}{\partial y}\,\mathrm{d}x. \tag{4.6}$$

At tonal frequencies, cavities with inclinations of ($\alpha = 90^\circ$, 60°, and 30°) exhibit an average acoustic particle velocity through the cavity opening of ($|\overline{v_a}|/U_\infty \approx 9.3\times10^{-3}$, 2.5×10^{-1} and

α	$He_{LES} = f_{LES}L/a_\infty$	$He_{APEs} = f_{APEs}L/a_\infty$	$\Delta He/He_{LES}$
30°	0.0827	0.0917	10.9%
60°	0.0827	0.0823	0.5%
90°	0.254	0.256	0.8%

TABLE 4.1: Comparison of the tonal frequencies observed in the LES and the computed acoustic modes from the APEs for deep cavities with three different inclinations. The frequency of the acoustic modes were found to closely align with the tonal frequencies from LES for all inclinations, except for the $\alpha = 30°$ inclined cavity. This discrepancy may suggest the beginning of subsidence of an acoustic resonance.

1.1×10^{-1}), respectively. In the inclined cavities, this amplitude of the acoustic field corresponds to "high pulsation levels", wherein the resonant field alters the vortex trajectory, forcing the vortex to enter and eject out from the cavity as opposed to adhering to the parallel path of the unperturbed shear layer (Peters, 1993a). Conversely, the oscillation in the orthogonal cavity is categorised by "low pulsation levels", where the subdued undulation of the shear layer and the nearly parallel trajectory of vortices may be traced back to a less efficient flow-acoustic coupling process.

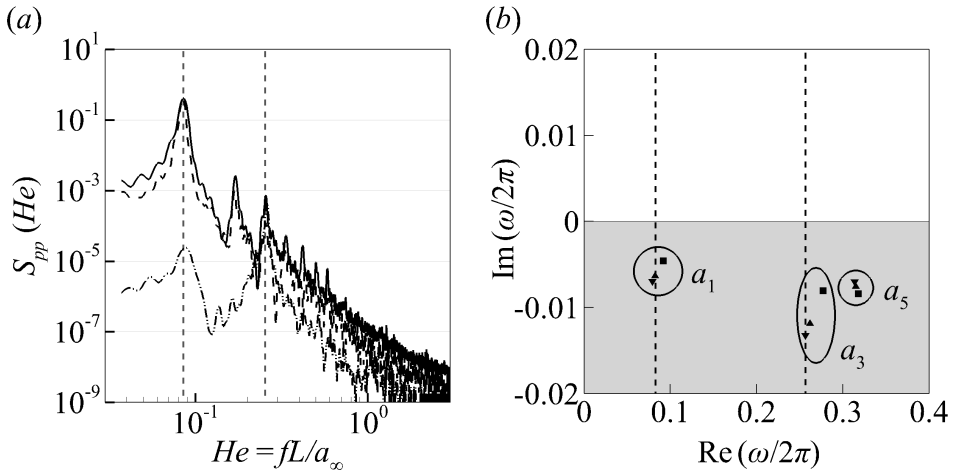

FIGURE 4.7: (*a*) Power spectral density (PSD) of the spanwise-averaged wall-pressure fluctuations with frequency expressed as Helmholtz number, He; and (*b*) First three least-damped acoustic modes obtained from the APEs. The deep cavity with the inclinations: $\alpha = 90°$ (■), 60° (▲), and 30° (▼) are represented accordingly. The vertical dashed lines (- - -) indicate the tonal frequencies observed in the current cavity configurations.

Figure 4.7(*a*) showcases a similar pressure spectrum of cavity oscillations as in figure 4.3(*a*), with the frequency here represented as the Helmholtz number, $He = fL/a_\infty$, for comparison with the first three least-damped acoustic modes of the cavities shown in figure 4.7(*b*). These acoustic modes are the eigenvalues of the linear operator of acoustic perturbation equations (APEs), as detailed in Subsection 2.4. Accordingly, the computed acoustic modes are compared with the tonal frequency of the cavity oscillations from the LES. Table 4.1 reveals that the computed acoustic modes matched closely with the tonal frequencies from the LES in all inclinations, except for the $\alpha = 30°$ inclined cavity case, where the slight discrepancy may suggest the initial acoustic resonance subsidence.

Based on this discussion, the weak resonance in the orthogonal cavity appears to be excited by the second Rossiter mode and the third depthwise acoustic mode. The other resonances,

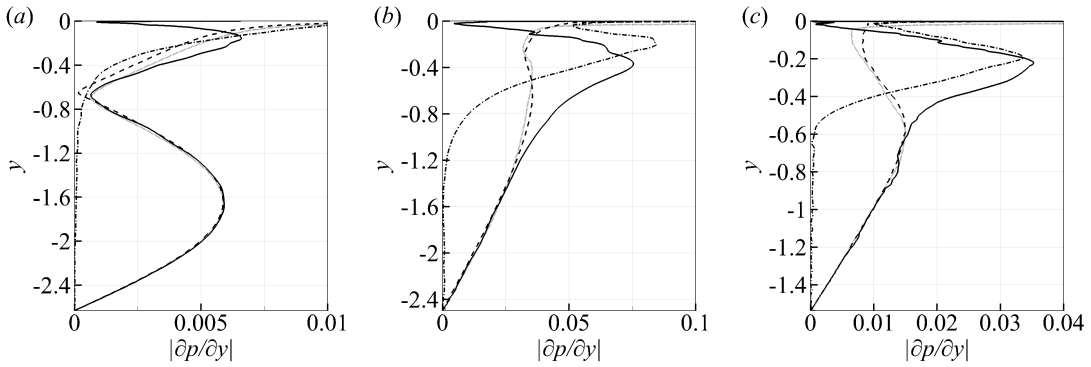

FIGURE 4.8: Depthwise variation of the magnitude of Fourier transformed pressure gradient, $|\partial p/\partial y|$ along the upstream wall for total (——), acoustic (- - -); and, hydrodynamic (-···-) pressure fluctuations, at their respective tonal frequencies for different inclinations, (*a*) $\alpha = 90^\circ$, (*b*) $\alpha = 60^\circ$, (*c*) $\alpha = 30^\circ$ at $M_\infty = 0.3$. The scaled pressure gradient of the Helmholtz acoustic resonance (·····) matches favourably with the acoustic mode shape obtained directly from the LES.

which are more robust, are excited by the first hydrodynamic mode and the first least-damped acoustic mode, where the former is indescribable by the Rossiter mechanism. Principally, we can describe that when acoustical resonating modes with a high-quality factor are available, the acoustical energy produced by the vortex shedding can accumulate in the cavity, and the induced acoustics particle velocity/displacement drives the vortex shedding process at a frequency close to the resonance frequency of the acoustic mode. The efficient fluid-acoustic coupling occurs when the first depthwise acoustic with the least damping is excited by the first hydrodynamic mode, which allows minimal radiation losses and efficient sound power production to tune the deep cavity systems to strong flow-induced oscillation in acoustic resonance.

As shown in figure 4.6, the pressure fluctuations across the flow region induced by unsteady vortex shedding at the downstream corner produce acoustic standing waves in cavities which can be described by using a one-dimensional wave approximation. Accordingly, the depthwise variations of the magnitude of Fourier transformed pressure gradient associated with the hydrodynamic and acoustic components for three different inclinations are shown in figure 4.8. In each inclination case, the acoustic wall-pressure gradient, $\partial p_A/\partial y$ along the upstream wall, shows that the amplitude increases along with the cavity depth toward the upstream corner and bears a close resemblance to a depthwise acoustic standing-wave. The direct eigenfunction (e.g. the mode shape of a nearby acoustic mode) of the linear operator of APEs matches favourably with the wavelength of the acoustic standing wave from the cavity oscillations and confirms this observation. Additionally, inclined cavity flows excite stronger oscillations compared to the orthogonal counterpart, which may occur since least damped oscillations at the cavity fundamental resonant frequency range may strengthen the overall fluid-acoustic coupling mechanism (Koch, 2005). These findings indicate the presence of acoustic resonance in the current cavity configurations. As indicated above, the oscillation frequency in the inclined cavity flows may be independent of the inclination angle. This observation implies that the acoustically forced global instability of the self-sustained oscillation in inclined cavities may be motivated by a mechanism independent of the Strouhal number.

The wall pressure gradient associated with the hydrodynamic component intensified near the cavity opening in all inclinations. Particularly, this is evident in inclined cavities where a distinct maximal at $y/L \approx 0.2$ is observed. The presence of favourable and adverse wall pressure gradients located slightly below the upstream corner may explain the efficient inward and outward deflection of the shear layer in inclined cavities, and to a lesser degree, for the orthogonal

cavity case. Based on the observation, the presence of an inclined cavity wall may facilitate the generation of a stronger vorticity field by the deflected shear layer near the upstream corner. This will be discussed in the next section.

In short, deep cavity flows with different inclinations display vastly different aeroacoustic responses in the presence of the same inflow condition. The pressure spectral reveals the tremendous increase in the magnitude of the acoustic response by a 30 dB difference from orthogonal to inclined cavities. Furthermore, the depthwise distribution of wall pressure fluctuation indicates that the acoustic resonance of different modes is sustained in all cases considered here. Particularly, the least-damped fundamental depthwise acoustic mode is sustained in inclined cavities, while the comparatively damped third depthwise acoustic mode is sustained in the orthogonal cavity. The excitation of the least-damped acoustic mode in inclined cavities minimises the radiation loss and facilitates an efficient conversion between the hydrodynamic and acoustic energy compared to the orthogonal cavity. Therefore the possibility of an intensified fluid-acoustic coupling between the shear layer and the acoustic fields in inclined cavities remains an interesting point to study. Before investigating this in more detail, it is helpful first to discuss the hydrodynamic velocity field near the cavity opening in Section 4.2, followed by the subsequent interaction with the acoustic resonance later in Section 4.3.

4.2 Hydrodynamic fields and the associated noise generation mechanisms

In this section, we will discuss the hydrodynamic fields near the cavity opening in detail. As mentioned, the location of the coherent vortical structure is crucial to the acoustic emission process. Therefore, an accurate description of the position and the path travelled by the vortical structure, which is a function of time, is essential for this investigation. Generally, the location of the vortical structure can be approximated by using the pressure minima technique, as shown in section 4.1. However, it is challenging to justify an accurate quantification of the hydrodynamic mode based on the number of discrete low-pressure spots (Ho and Kim, 2021b). To ovecome this limitation, the location of the vortical structure is identified using the equivalent Q-criterion (Bradshaw, 1981), which is given by:

$$Q = \varepsilon_{ij}\varepsilon_{ji} - \frac{1}{2}\omega_i^2 \approx -\nabla^2 \tilde{p_H}/\rho_\infty = \tilde{Q}, \tag{4.7}$$

where $\varepsilon_{ij} = \frac{1}{2}(\partial u_i/\partial x_j + \partial u_j/\partial x_i)$ represents the rate of strain, ω_i denotes the vorticity of the velocity field, and $\nabla^2 \tilde{p_H}$ is the Laplacian of the hydrodynamic pressure field. This formulation offers two advantages: firstly, equation (4.7) provides a link between the velocity gradient field and the hydrodynamic pressure field to better locate the position of the vortex. Secondly, the strain-rate and vorticity fields provide physical interpretations of the velocity field, which are useful in qualifying the following noise generation mechanism. (Naguib and Koochesfahani, 2004).

Figure 4.9 shows an oscillation cycle of χ similar to that of figure 4.4, with particular attention given to the vortex dynamics near the cavity opening region. Plotted is the Q-criterion, Q calculated from (4.7), and superimposed with streamlines to signify the shear layer oscillation near the cavity opening. Similarly, we examine the vortex dynamics in the $\alpha = 60^\circ$ inclined cavity to facilitate the following discussion. Figure 4.9(a) shows the moment when the large-scale vortex (characterised by $Q < 0$) is positioned marginally above the cavity opening line (i.e., $y > 0$), due to the maximum outflow from the cavity. Consequently, the interaction of the vorticity field with the downstream corner necessitates an imaginary mirror image of an opposite vorticity field to

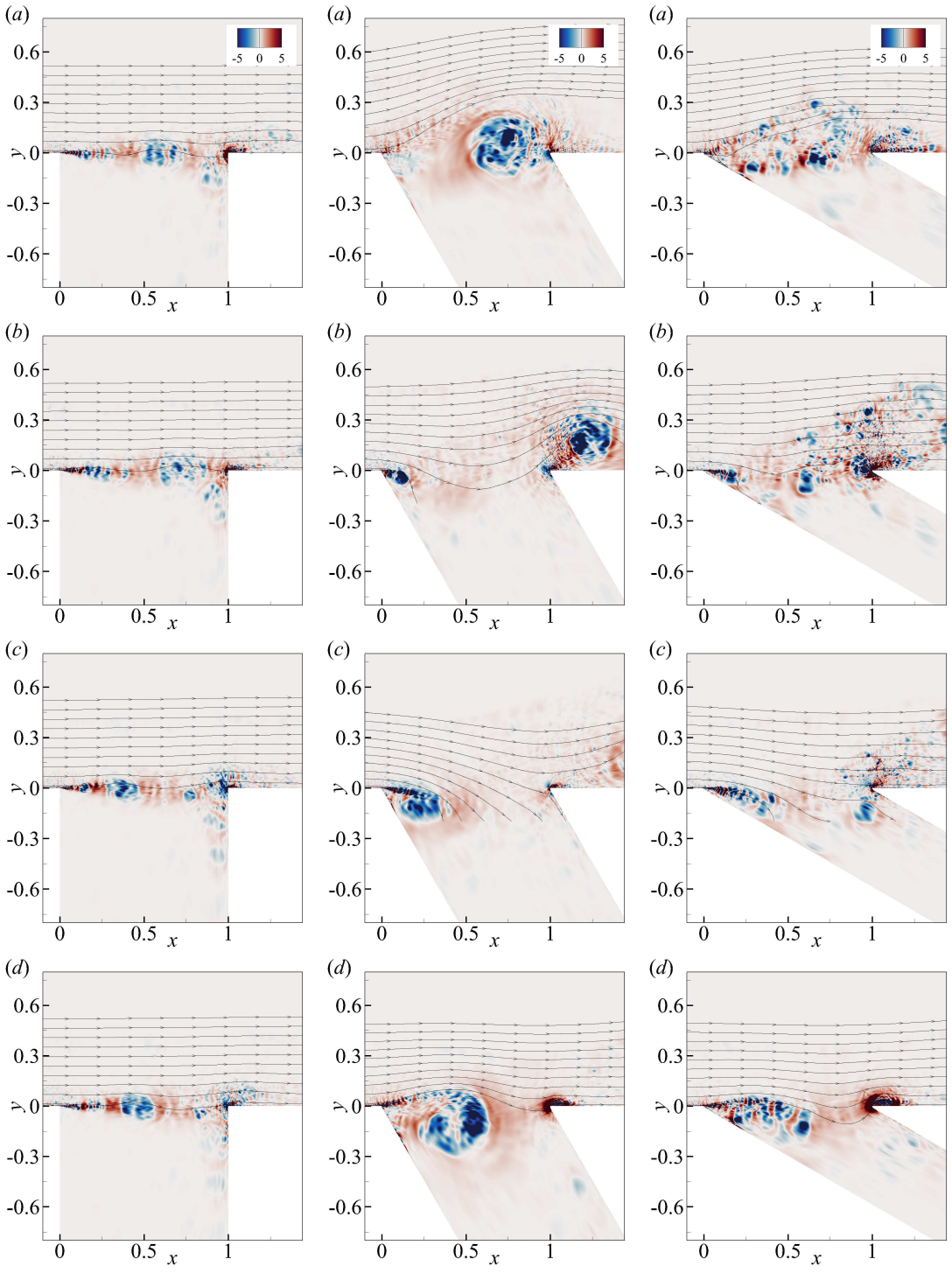

FIGURE 4.9: Snapshots of the spanwise-averaged instantaneous Q-Criterion with superimposed streamlines to signify the shear layer undulation across the cavity opening with a time interval of $T/4$ between two successive plots from (a) to (d), where T is the period of the oscillation cycle of χ. The first, second and third columns correspond to deep cavities with the inclinations: $\alpha = 90°$, $\alpha = 60°$ and $\alpha = 30°$, respectively. For the corresponding pressure fields, see figure 4.4.

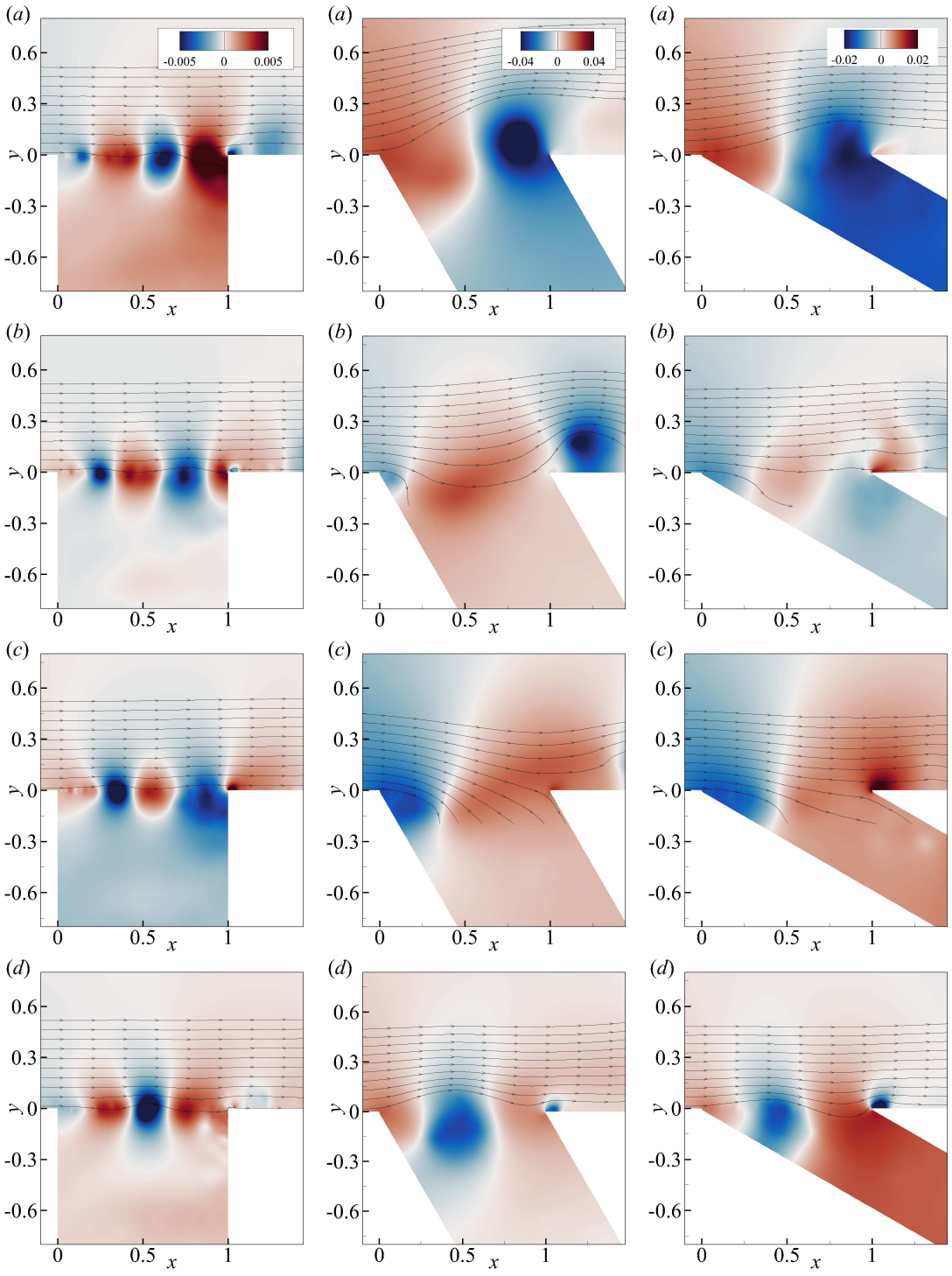

FIGURE 4.10: Snapshots of the hydrodynamic pressure fluctuation, p'_H near the cavity opening region with superimposed streamlines to signify the shear layer undulation with a time interval of $T/4$ between two successive plots from (a) to (d), where T is the period of the oscillation cycle of χ. The first, second and third columns correspond to deep cavities with the inclinations: $\alpha = 90°$, $\alpha = 60°$ and $\alpha = 30°$, at $M_\infty = 0.3$ respectively. For the corresponding pressure fields, see figure 4.4.

satisfy the no-slip boundary condition at the wall. The presence of vorticity near the wall results in a low hydrodynamic pressure field, as indicated by $\nabla^2 p_H > 0$, as shown in figure 4.10(a). This low hydrodynamic pressure field acting on the wall generates rarefaction acoustic waves, which interfere destructively with the compressive acoustic waves reflected within the cavity.

As the large-scale vortex approaches closer to the downstream corner, the vorticity field acting on the wall is amplified. Consequently, the amplified vorticity field necessitates the presence of an imaginary mirror image of a stronger opposite vorticity field, which results in the generation of additional rarefaction acoustic waves. These waves undergo constructive interference with the acoustic waves reflected from the base of the cavity until the large-scale vortex stretches and ejects completely from the cavity, as shown in figure 4.9(b). The complete ejection of the vortex is immediately followed by a rapid downward deflection of the shear layer near the upstream corner, accompanied by the emergence of small-scale vortices (e.g. low hydrodynamic pressure spots) within the separated shear layer, as shown in figure 4.10(b). These small vortices subsequently grow and merge, ultimately forming a single large-scale vortex near the upstream corner, as depicted in figure 4.9(c).

Further downward deflection of the shear layer near the downstream corner formed a region of the high strain-rate field (e.g. $Q > 0$) on the downstream wall due to stagnated flow, and a compressive hydrodynamic pressure field is generated as shown in figure 4.10(c). Furthermore, at this instant represents the maximum mass flow into the cavity. As the shear layer slowly detaches from the downstream corner, the upward deflection of the shear layer generates a strain rate field (e.g. $Q > 0$) on the front surface of the downstream corner ensuing from the upward momentum flux, as shown in the figure 4.9(d). Similarly, a low-pressure region is gradually formed near the edge of the top surface of the downstream corner due to flow separation. At the same time, the newly formed vortices near the upstream corner amalgamate to form a large-scale vortical structure (represented by $Q < 0$) through additional vortex pairings, which are visually similar to the schematic drawing of the "collective interaction" provided by Ho and Nosseir (1981).

In addition, the observed shear layer oscillation and the non-parallel trajectory of the large-scale vortex in the inclined cavity oscillation are also similar to those observed in deeper cavities within gas flows in pipes with closed side branches, as reported by Kriesels et al. (1995). Drawing from this observation, we suggest that the deflection of the shear layer near the upstream corner is primarily controlled by the forcing generated by the time-varying mass flow rate passing through the cavity opening. Accordingly, the mass forcing through the cavity opening, denoted as $d\dot{m}/dt$, is decomposed into solenoidal and irrotational components by performing an integration of the rate of change of vertical momentum-density across the cavity opening in the streamwise direction, such as:

$$\frac{d\dot{m}_A}{dt}(t) = -\frac{1}{dt}\int_0^L \nabla\psi_A(x, y=0, t)\, dx, \tag{4.8a}$$

$$\frac{d\dot{m}_H}{dt}(t) = \frac{1}{dt}\int_0^L B_y(x, y=0, t)\, dx. \tag{4.8b}$$

Figure 4.11(a, b) shows the solenoidal component, dB_y/dt, induced by the large-scale convective vortex. It is characterised by a highly localised spatial distribution, in contrast to the uniformly distributed irrotational component, $d\nabla\psi_A/dt$, which is induced by the depthwise acoustic resonance. Additionally, the deflection of the shear layer near the upstream corner is quantified by monitoring the vertical coordinate of the streamtrace near the location where $x = 0.2$. Figure 4.11(c) displays the time variation of the vertical coordinate of the streamtrace near the upstream corner. The results reveal that the deflection of the shear layer is closely synchronised with the irrotational component of the mass forcing induced by the depthwise acoustic

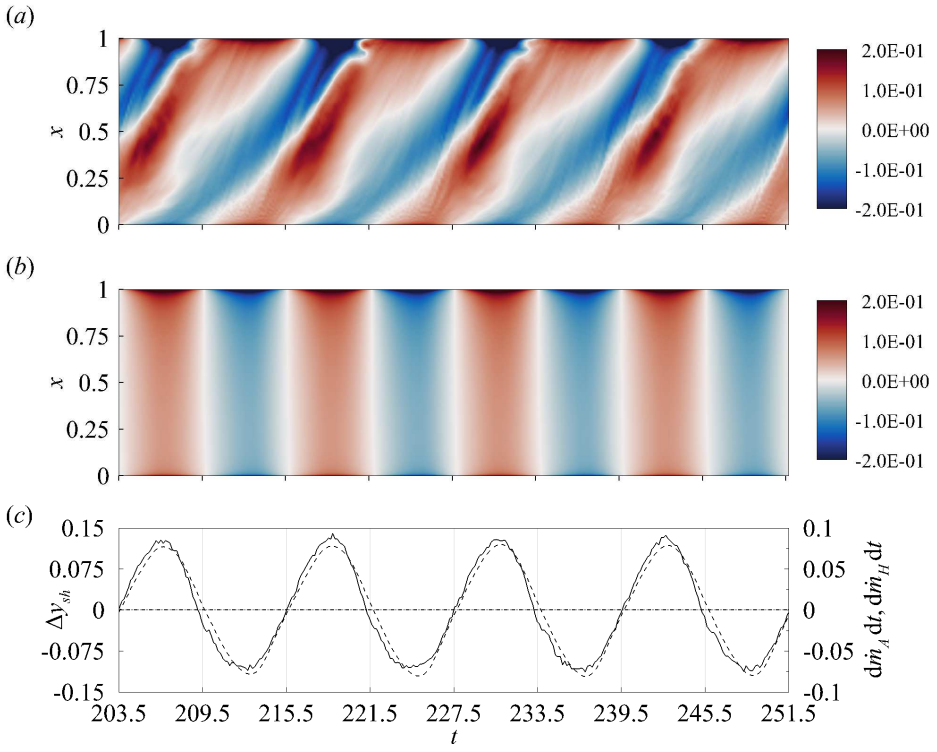

FIGURE 4.11: The space-time contour plots of (a) the solenoidal (hydrodynamic) component; (b) the irrotational (acoustic) component, of the rate of change of vertical momentum-density, $\partial(\rho v)/\partial t$ across the cavity opening (e.g. $y/L = 0$); and, (c) the time variation of integrated vertical momentum-density rates across the cavity opening associated with acoustic (- - -), hydrodynamic (-···-) fields, and y-coordinate of the shear layer oscillation measured near the upstream corner at $x = 0.2$ (——) for the $\alpha = 60^\circ$ inclined and deep cavity.

resonance. This finding highlights the dominant influence of the spatially coherent depthwise acoustic resonance on the shear layer oscillation. Therefore, it is plausible to suggest that the shear layer oscillation could be mainly controlled by the spatially coherent irrotational component of the vertical momentum-density induced by the depthwise acoustic resonance.

4.3 Fluid–acoustic coupling mechanism and convection speed of coherent vortical structures

In Section 4.1, it is evident that the fundamental resonant frequency with a mode shape similar to a one-quarter wave is presented in the cavity. Therefore, it bears the question of whether an effective coupling mechanism exists between the shear layer and the acoustic resonance to facilitate this formation. As mentioned, past investigations have indicated the acoustic resonance has a deterministic role on shear layer oscillation, particularly near the receptivity of the shear layer (e.g. upstream corner). Therefore, a better understanding of the phase relationship between the region of maximum receptivity of the shear layer and the acoustic resonance is crucial in this investigation. One plausible way to achieve this is to invoke the one-dimensional plane wave approximation, whereby the standing-wave induces acoustic particle velocity primarily in the vertical direction. This approximation is justified for the current cavity configuration based on our previous observation in Section 4.1, that the acoustic pressure field bears a close resemblance to a one-quarter vertical standing-wave.

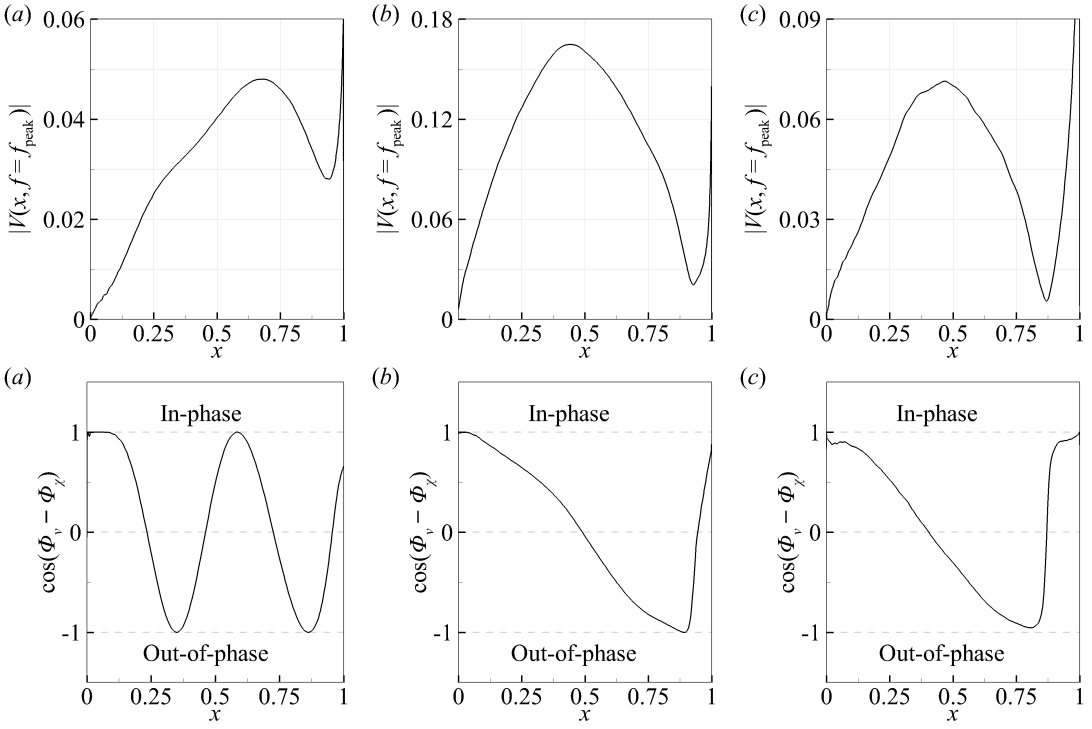

FIGURE 4.12: Streamwise variation of the magnitude (first row) and cosine of phase (second row) of the Fourier transformed decomposed vertical velocity fluctuations, $V(x,f)$ across the cavity opening (e.g. $y/L = 0$) for $\alpha = 90^\circ$ orthogonal cavity (a), $\alpha = 60^\circ$ inclined cavity (b), and $\alpha = 30^\circ$ inclined cavity (c) at $M_\infty = 0.3$.

Accordingly, Fourier transform is performed on the space-time vertical velocity fluctuation across the cavity opening and the respective magnitude, $|V(x,f)|$ and phase, $\Phi_v(x,f)$ at the tonal frequencies are plotted in figure 4.12. In the orthogonal deep cavity, the streamwise amplification follows almost a linear fashion reaching up to $x/L \approx 0.75$ before reducing to a local minimum and rising to a concentrated peak near the downstream corner. Similarly, the streamwise amplification in inclined cavity flows reaches a maximum of around $x/L \approx 0.5$ before reducing to a local minimum and rising to a concentrated peak near the downstream corner. Based on the visualisation of the vortex dynamics and the shear layer oscillation, it is reasonable to suggest that the former reduction is caused by the destructive interference of the induced downwash velocity by the coherent vortices and the upwash generated by the shear layer oscillation. The latter concentrated peak near the downstream corner is caused by the vortex-wall interaction, which intensified considerably in inclined cavities. Particularly, it is worth highlighting that the location at which the minimum velocity fluctuation (e.g. $x/L \approx 0.85$) is the furthermost away from the downstream corner in $\alpha = 30^\circ$ inclined cavity case, suggesting the greatest vortex-wall interaction. In addition, the cosine of the phase difference, $\cos[\Phi_v(x,f_1) - \Phi_\chi(x,f_1)]$ as shown in figure 4.12(a, b) reveals a region of acoustic modulation where the velocity fluctuation near the upstream corner remains highly synchronised with the averaged acoustic wall-pressure fluctuation at the cavity base, χ. This indicates the obvious point that the depthwise acoustic resonance highly controls the vertical velocity oscillation in shear layer separation. Therefore, there is strong evidence of the fluid-acoustic process due to the perfect synchronisation near the upstream corner between the vertical velocity fluctuation and the acoustic forcing generated by the resonance. Furthermore, the formation of coherent vortices that are highly in-phase with the acoustic forcing near the upstream region (e.g., $\cos[\Phi_Q(x,f_p) - \Phi_\chi(x,f_p)] = 1$), as shown in figure 4.13, further reconfirm this fluid-acoustic coupling process.

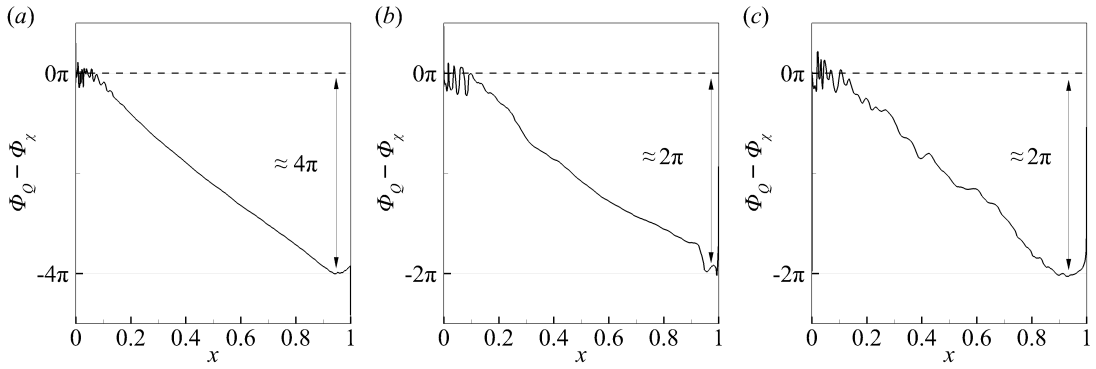

FIGURE 4.13: The streamwise phase variation of the Fourier-transformed Q-Criterion, $\Phi_Q(x,f)$, measured across the cavity opening (e.g. $y = 0$) at the respective tonal frequency for deep cavities with inclinations: $\alpha = 90°$, $\alpha = 60°$ and $\alpha = 30°$, respectively. Note that the spatial variation of $\Phi_Q(x,f)$ is calculated based on the phase reference of $\Phi_\chi(x,f)$.

Based on the work of Rockwell and Naudascher (1979); Knisely and Rockwell (1982); Rockwell (1983); Tuna and Rockwell (2014), it has been established that a self-sustained oscillation of an n hydrodynamic mode requires a phase criterion of (e.g. $\Delta\Phi_Q(x,f_p) = 2\pi n$). This study reaffirms this phase criterion, as shown in figure 4.13. Subsequently, the average convection speed, U_c, is calculated using linear dispersion relation based on the streamwise phase variation of the Q-Criterion.

α	fL/a_∞	$\Delta\Phi_{V_H}/2\pi$	$M_c = U_c/a_\infty$	$K_c = U_c/U_\infty$
30°	0.0828	≈ 1.00	0.0828	0.276
60°	0.0828	≈ 1.00	0.0828	0.276
90°	0.2548	≈ 1.00	0.1274	0.424

TABLE 4.2: Average convection speed ratio, $K_c = U_c/U_\infty$, of the vortical structures at each tonal frequency is calculated based on the streamwise phase variation of the Q-Criterion using the linear dispersion relation, considering the free-stream Mach number of $M_\infty = 0.3$ for deep cavities with inclinations: $\alpha = 90°$, $\alpha = 60°$ and $\alpha = 30°$, respectively.

Table 4.2 reveals a significant disparity in the averaged convection speed ratio in orthogonal and inclined cavities, with the latter demonstrating a slower convection speed despite employing the identical inflow condition. Figure 4.14 clearly depicts this difference by comparing the magnitude of the Fourier-transformed Q-Criterion, $|Q|$, with the time-averaged streamwise velocity, $\bar{u}$. Accordingly, it is found that the tracked trajectory of the coherent vortices display an almost horizontal trajectory along the cavity opening in the orthogonal cavity. However, in the case of inclined cavities, the large-scale vortex structure descends deeper into the cavity and subsequently experiences a reduced streamwise velocity before its eventual ejection. Therefore, these discrepancies in the vortex trajectory yield two important observations.

Firstly, the coherent vortices in the orthogonal cavity (with a $St \approx 0.85$) traverse the cavity opening at a faster average convection speed due to their nearly parallel trajectory. Secondly, the large-scale vortical structure in inclined cavities (with a $St \approx 0.27$) convects at a slower average convection speed due to its downward trajectory into the interior of the cavity. Furthermore, the large discrepancy between the local convection speed and the time-averaged streamwise velocity implies significant unsteady influence is exerted by the acoustic resonant field on the large-scale vortex convection, as shown in figure 4.15. Consequently, these findings emphasise and possibly explain the potential relationship between the convection speed of the coherent

vortices (determined by their trajectory) and the Strouhal number of the cavity oscillation. These factors are crucial when predicting the frequency of cavity oscillations using a semi-empirical formula that requires an estimation of the averaged convection speed.

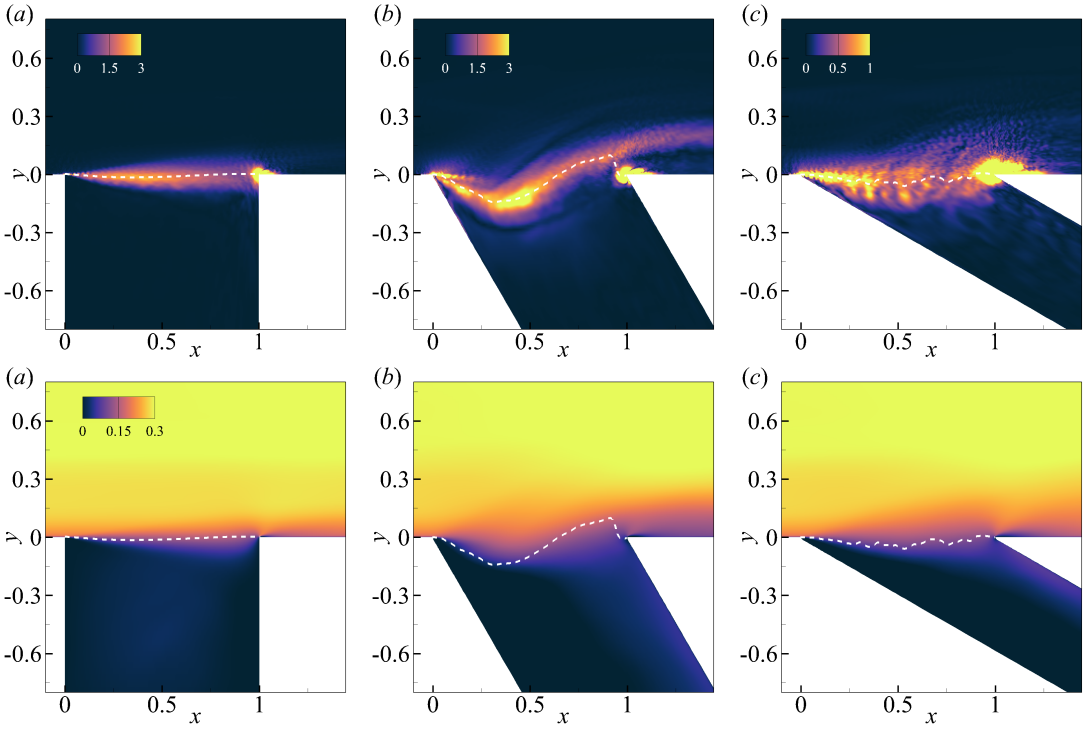

FIGURE 4.14: The top row of the contour plots represents the spatial distribution of the magnitude of the Fourier-transformed Q-Criterion, $|Q(x,f)|$, while the bottom row of the contour plots showcases the spatial distribution of the time-averaged streamwise velocity. The inclinations are shown in (a) $\alpha = 90°$, (b) $\alpha = 60°$, and (c) $\alpha = 30°$, respectively. The trajectory of the vortical structures is traced by monitoring the maximum value of $|Q(x,f)|$ near the cavity opening. The tracked trajectory is superimposed onto the time-averaged streamwise velocity contour plot for visual comparison.

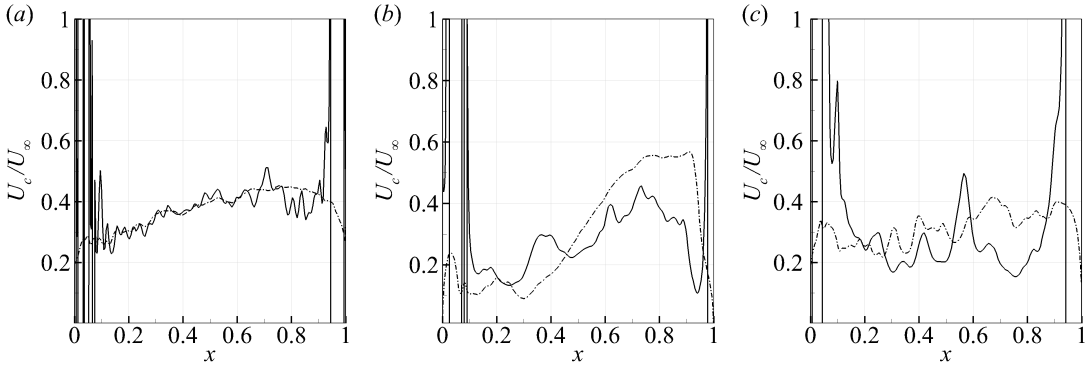

FIGURE 4.15: The local variation of the convection speed of the coherent vortices calculated using the streamwise phase variation of the Q-Criterion, Φ_Q measured across the orthogonal cavity opening in the streamwise direction at three different inclinations: $\alpha = 90°$ (a), $\alpha = 60°$ (b), and $\alpha = 30°$ for $M_\infty = 0.3$ at the respective peak frequency. The local convection speed of the coherent vortices (——) is largely inconsistent with the respective time-averaged streamwise velocity (-···-), particularly in the region of $0.2 \leq x \leq 0.8$ before the impingement on the downstream corner.

4.4 Aeroacoustic sources and noise generations

Section 4.2 presented findings showing how the depthwise acoustic resonance in inclined cavities primarily controls the synchronised deflection of the shear layer near the upstream corner. This physical phenomenon enables the generation of vorticity that, when combined with resonant acoustic fields, results in a dominant noise source according to the Vortex Sound Theory (Howe, 2003). The relationship between vortex shedding and sound generation has been established in the seminal work by Howe (1998). In particular, an essential aspect of this relationship is the calculation of the instantaneous acoustic source power, Π, which can be estimated using the following approximation:

$$\Pi \approx -\rho_\infty \iint_x (\omega \times u) \cdot u_a \, dx, \tag{4.9}$$

where ω is the vorticity vector and u_a refers to the acoustic particle velocity vector. The triple-dot product $((\omega \times u) \cdot u_a)$ provides quantitative insight into the local energy transfer between the hydrodynamic and acoustic fields. Precisely, the integrand captures the transfer of acoustic energy to hydrodynamic energy (e.g. $(\omega \times u) \cdot u_a > 0$) and vice-versa. Consequently, the self-sustained oscillations can only occur if the integral in (4.9) yields a positive value throughout an acoustic cycle. Therefore, this condition, in turn, necessitates a favourable phase relationship between the Lamb vector, $(\omega \times u)$, and the acoustic field, u_a. In the ensuing discussion, we present the temporal evolution of the Lamb vector within the acoustic velocity to elucidate this energy exchange mechanism.

Figure 4.16 shows the temporal evolution of the Lamb vector and the acoustic particle velocity field within the inclined cavity at an inclination angle of $\alpha = 30^\circ$ in a single acoustic cycle. Particularly, figure 4.16(*a-b*) illustrates the first half of the acoustic cycle, that is the acoustic absorption phase, during which the hydrodynamic instabilities in the shear layer absorb the acoustic energy, resulting in the formation of a coherent vortex structure. Moreover, the residual vorticity near the downstream corner, originating from the previous cycle, is observed to absorb a non-negligible amount of acoustic energy. Subsequently, figure 4.16(*c-d*) depicts the second half of the acoustic cycle, that is the acoustic production phase, wherein the generated vorticity is now in-phase with the acoustic particle velocity field until its eventual ejection from the cavity in the same direction as the acoustic particle velocity. Conversely, figure 4.17 shows the respective acoustic production and absorption cycle in the $\alpha = 60^\circ$ inclined cavity, which shares considerable similarities with the $\alpha = 30^\circ$ inclined cavity. However, two noticeable differences can be identified between the two cases. Firstly, the vortex structure in the $\alpha = 60^\circ$ inclined cavity exhibits an enhanced spanwise coherence, contributing to a more significant Lamb vector. Furthermore, the diminished residual vorticity near the downstream corner reduces the absorption of acoustic energy. Therefore, the greater coherence of vorticity and the decreased acoustic absorption potentially explain the stronger acoustic response observed in the $\alpha = 60^\circ$ inclined cavity.

The preceding discussion based on Vortex Sound Theory provides an acceptable explanation for the intensified acoustic response observed in the inclined cavity at an inclination of $\alpha = 60^\circ$. To probe further into the intrinsic mechanism of noise generation within the cavity flow system, an acoustic input-output analysis (as outlined in Subsection 2.4) is conducted. The central aim is to establish a direct quantitative link between the Lamb vector and the magnitude of the acoustic response by uncovering the corresponding amplification rates and forcing-response mode shapes of the input-output operator of the APEs. Accordingly, figure 4.18 showcases the first three leading amplification rates of the input-output operator across varying frequencies. It is apparent that the first leading amplification rate significantly surpasses the second and third

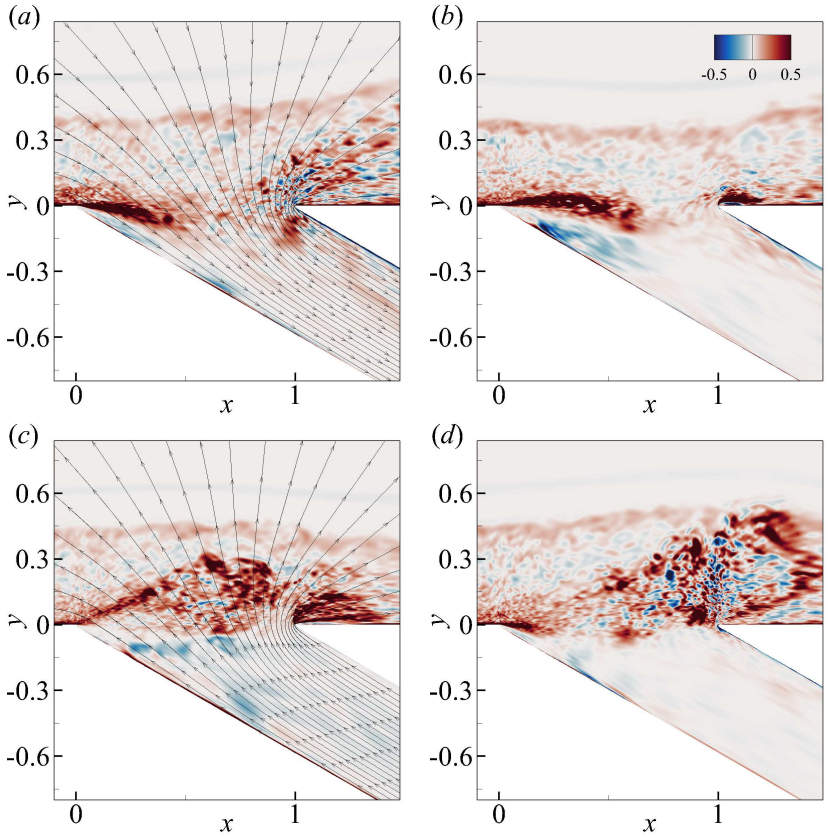

FIGURE 4.16: The time evolution of the Lamb vector ($\omega \times u$) in the vertical direction is examined for a single acoustic cycle for the $\alpha = 30^{\circ}$ inclined cavity. The contour plots capture two key time instants: (a) when the instantaneous acoustic source power, Π, reaches its maximum, and (c) when it reaches its minimum. The contour plots (b,d) indicate the time junctures when the instantaneous acoustic source power becomes zero (e.g. $\Pi = 0$). Here, the superimposed streamline represents the instantaneous acoustic particle velocity field.

leading amplification rates at the tonal frequencies in all inclinations. This key observation underscores the low-rank behaviour of the cavity oscillations investigated in this study. This low-rank behaviour, therefore, enables a rank-1 approximation of the input-output operator of APEs, wherein the first rank sufficiently describes the acoustic response of the cavity system, such as:

$$R_{\tilde{q},\omega} = U\Sigma V^{*} = \sum \sigma_i u_i v_i \approx \sigma_1 u_1 v_1. \tag{4.10}$$

In this formulation, u_1 and v_1 represent the leading optimal forcing and response mode, while σ_1 specifies the gain of the leading forcing-response pair. Thus, this facilitates a quantitative link between the input forcing, $\hat{f}_{\omega}$, (e.g. Lamb vector) and the corresponding output acoustic field quantities, $\hat{q}_{\omega}$, (e.g. acoustic pressure) which can be represented such as:

$$\hat{q}_{\omega} = R_{\tilde{q},\omega}\hat{f}_{\omega} \approx \sigma_1 u_1 v_1 \cdot \hat{f}_{\omega} = \sigma_1 u_1 F_{\omega}. \tag{4.11}$$

Accordingly, figure 4.19 shows the spatial distribution of the magnitude of the reconstructed acoustic pressure field for cavities with all inclinations, computed based on the first-rank approximation. Notably, the reconstructed acoustic pressure fields exhibit favourable agreements with those directly obtained from the LES. This notable finding substantiates the assertion that the first-rank reconstruction of the acoustic pressure field adequately reproduces the results obtained for cavities with all inclinations from the present LES.

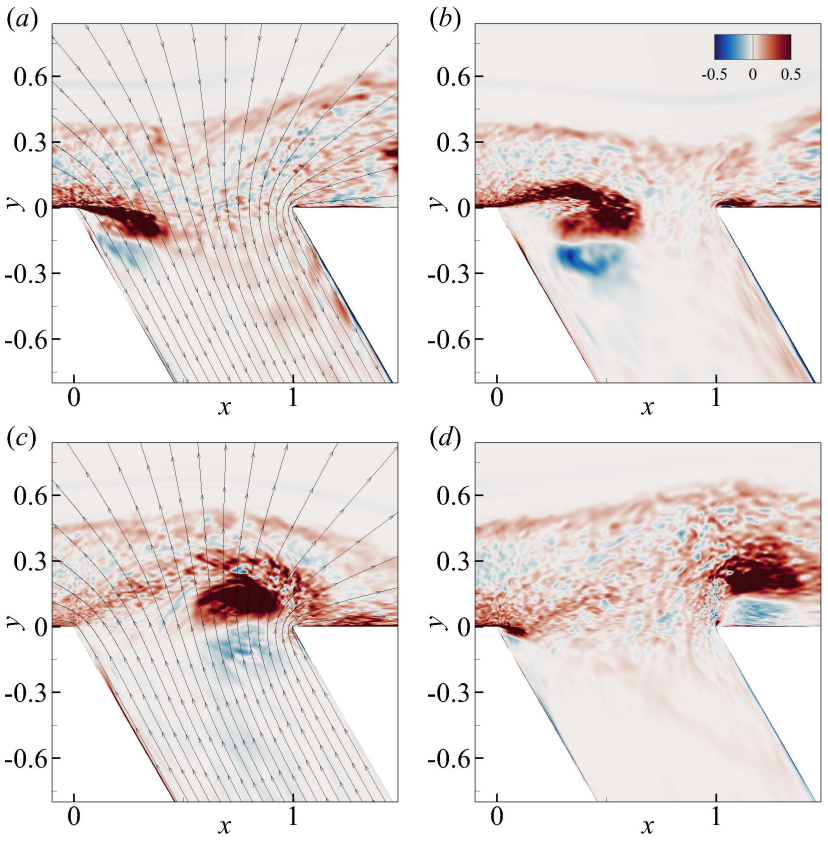

FIGURE 4.17: The time evolution of the Lamb vector ($\omega \times u$) in the vertical direction is examined for a single acoustic cycle for the $\alpha = 60^\circ$ inclined cavity. The contour plots capture two key time instants: (a) when the instantaneous acoustic source power, Π, reaches its maximum, and (c) when it reaches its minimum. The contour plots (b,d) indicate the time junctures when the instantaneous acoustic source power becomes zero (e.g. $\Pi = 0$). Here, the superimposed streamline represents the instantaneous acoustic particle velocity field.

Figure 4.20(a, b) compares the integrated volume forcing, F_ω, and the leading gain, σ_1, from the input-output operator of the APEs for cavities with all inclinations. Upon closer examination, we observe distinct characteristics that contribute to the variations in the acoustic response among the cavity cases. Namely, the diminished acoustic response of the orthogonal cavity can be attributed to two main factors: the reduced amplification of the leading gain and the pronounced source-sink cancellation. Specifically, the reduced amplification of the leading gain in the orthogonal cavity can be linked to the excitation of the third depthwise acoustic mode, which is heavily damped. Furthermore, the pronounced source-sink cancellation observed in the orthogonal cavity is primarily caused by the excitation of the second hydrodynamic mode. In particular, this mode consists of multiple vortices that exhibit strong interactions between the source and sink regions, leading to destructive interference and decreased integrated volume forcing, as visualised in figure 4.21(a). Therefore, the acoustic response in the orthogonal cavity is reduced.

In contrast, the inclined cavities exhibit stronger acoustic responses due to two crucial factors. Firstly, the first least-damped depthwise acoustic mode in these inclined cavities has a higher amplification rate than that of observed in the orthogonal cavity. Secondly, the inclined cavities experience a reduced source-sink cancellation due to the weaker interaction between the source and sink regions produced by the single large-scale vortex structure, as visualised in figure 4.21(b,c). The reduced source-sink cancellation enhances the integrated volume forcing and

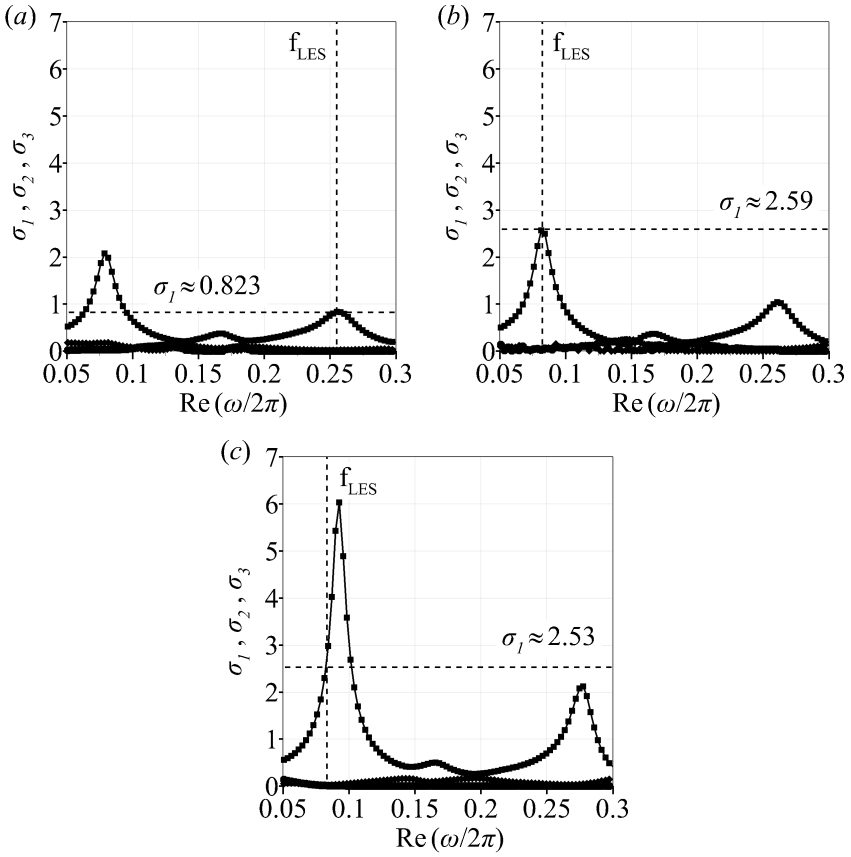

FIGURE 4.18: The low-rank behaviour of the input-output operator is visualised through the first three leading magnification rates; σ_1 (■), σ_2 (▲), and σ_3 (◆) for deep cavities with inclinations: $\alpha = 90^\circ$ (*a*), $\alpha = 60^\circ$ (*b*), and $\alpha = 30^\circ$ (*c*), respectively. The vertical dashed line (- - -) indicates the tonal frequency observed in the LES, while the horizontal dashed line (- - -) represents the corresponding leading amplification rate σ_1 at that particular tonal frequency.

produces a stronger acoustic response. These important factors produce the contrasting acoustic responses between the orthogonal and inclined cavities, as shown in figure 4.20(*c*). In addition, it is worth mentioning that the acoustic amplification rate at $\alpha = 30^\circ$ inclined cavity is much higher, as shown in figure 4.18, which is stipulated to be associated with an efficient scattering from the sharper downstream corner as compared to the orthogonal cavity configuration. This may explain the observation of the comparable acoustic response of inclined cavities, despite the fact that the tonal frequency peak observed in the LES differs from that of the acoustic resonance frequency predicted by the APEs in $\alpha = 30^\circ$ inclined cavity.

4.5 Stability, receptivity and sensitivity of cavity systems

In Section 4.4, the least-damped acoustic modes of the deep cavity geometries were identified through the direct computation of the least unstable mode of the APEs. In this section, the stability, receptivity, and sensitivity of the cavity systems are further investigated by performing computations of the direct and adjoint instability modes using the linearised Navier-Stokes equations. Through this analysis, the mode shape of the instability is characterised, and the localised region that is most receptive and sensitive to external forcings can be identified. Specifically, bi-global linear stability analyses are conducted based on the time-averaged mean flow fields

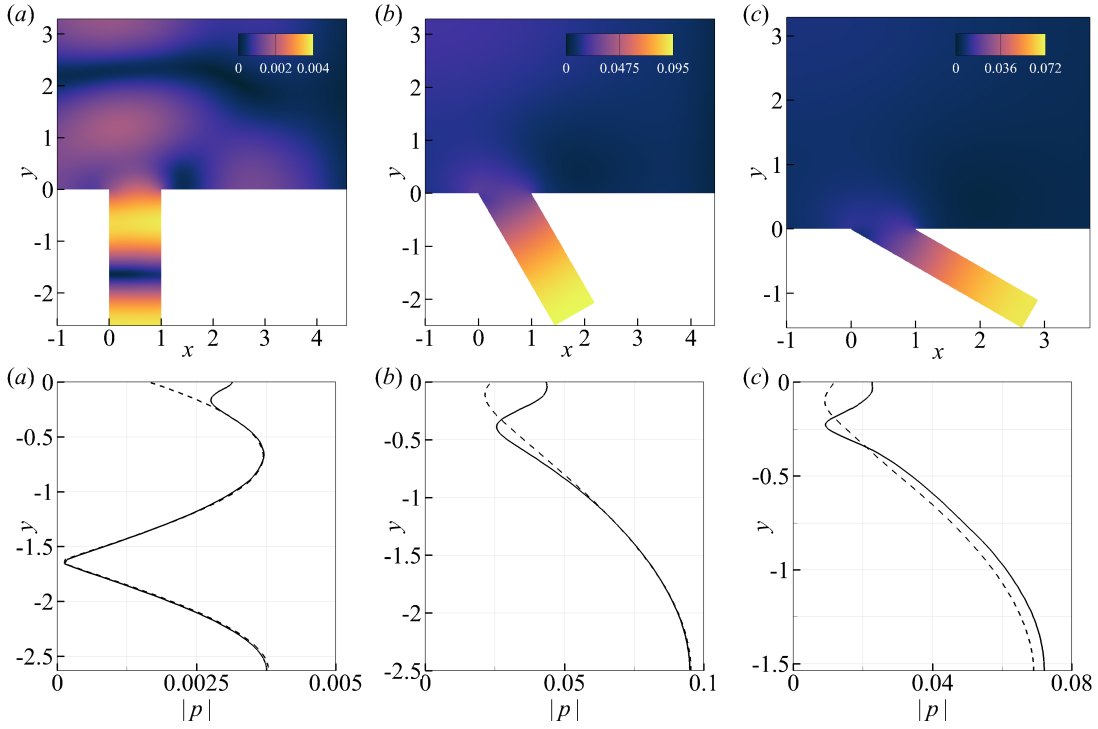

FIGURE 4.19: The first row of the contour plots shows the spatial distribution of the magnitude of the reconstructed acoustic pressure field for cavities with inclinations: $\alpha = 30^\circ$ (*a*), $\alpha = 60^\circ$ (*b*), and $\alpha = 90^\circ$ (*c*), respectively. The second row of line plots demonstrates that the depthwise distribution of wall-pressure fluctuations measured along the upstream cavity wall from the LES (——), compared favourably with the reconstructed acoustic pressure field from the rank-1 approximation of the APEs (- - -).

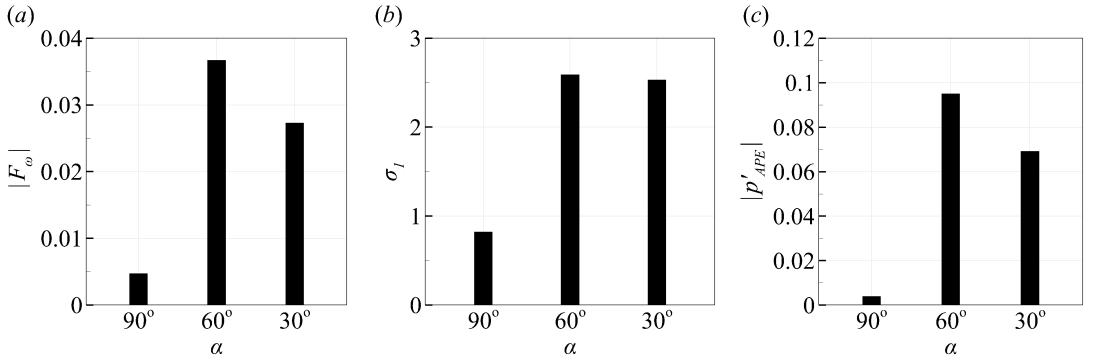

FIGURE 4.20: (*a*) The magnitude of the integrated volume forcing, represented by $|F\omega|$, and (*b*) The first leading gain, denoted as σ_1, of the input-output operator of the APEs. (*c*) The reconstructed acoustic response measured at the cavity base, $|p'_{APE}|$, is obtained from the 1-rank approximation computed using equation (4.11).

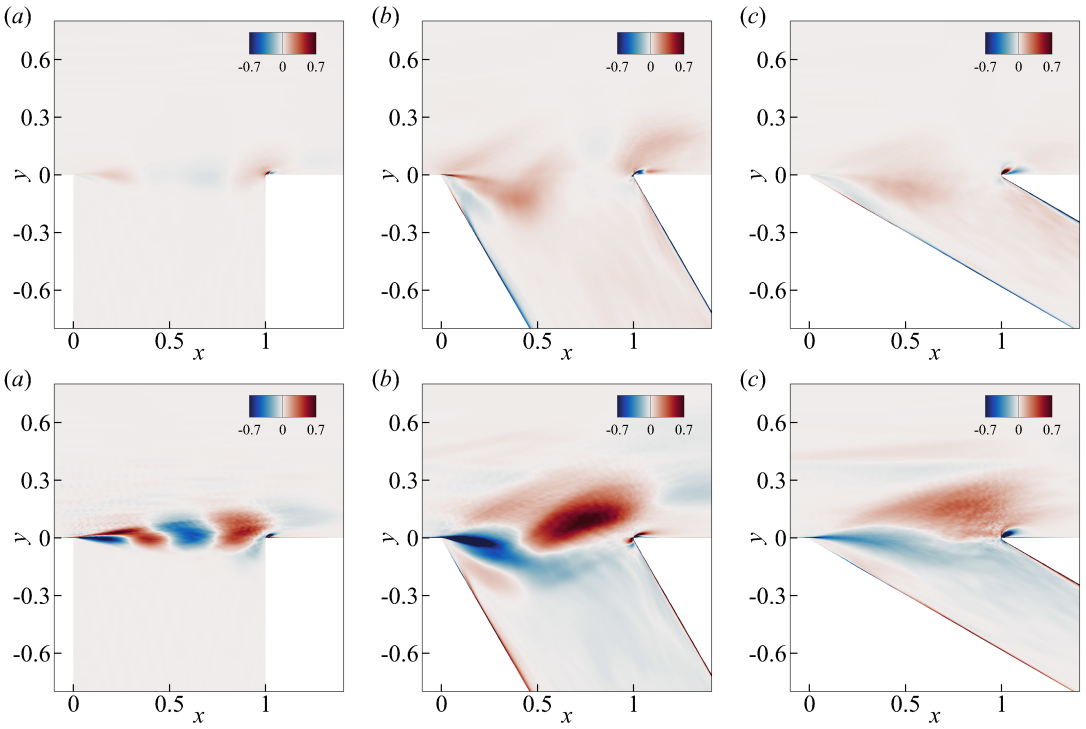

FIGURE 4.21: The spatial distribution of the real part of the component-wise multiplication between the leading optimal forcing mode, v_1, and the input forcing, $\hat{f}_\omega$, in the streamwise direction (top row of the contour plots) and the vertical direction (bottom row of the contour plots) for deep cavities with inclinations: $\alpha = 90^\circ$ (*a*), $\alpha = 60^\circ$ (*b*), and $\alpha = 30^\circ$ (*c*), respectively. Note that the phase of the cycle (as shown in the contour plots) is selected such that the imaginary part of the integrated volume forcing is zero to accentuate the source-sink cancellation effect.

obtained from the LES. Figure 4.22 presents the results of the bi-global linear stability analysis, showing the frequency (real part) and growth rate (imaginary part) of the leading unstable mode obtained from the eigenspace of the linear operator for inclined and deep cavities. The comparison revealed that the frequency of the leading unstable mode closely matched the tonal peak frequency observed in the LES for cavities with all inclinations. This suggests that the aeroacoustic phenomena discussed in the previous sections can be attributed to unstable global modes. Furthermore, we examined the spatial distribution of the amplitude of the direct modes, represented as $|\widehat{p}|$, and compared them to those obtained from the LES. Remarkably, the results exhibited a close resemblance, providing further support to the subsequent discussion presented in this section.

Figure 4.23 shows the spatial distribution of the disturbance (direct eigenfunction) and the receptivity (adjoint eigenfunction) of the vertical momentum. It is observed that the amplification of disturbances along the cavity opening captures the progressive strengthening of the vortex as it convects downstream. In contrast, the receptivity of the vertical momentum is predominantly localised near the upstream corner of the cavity. Physically, this adjoint global mode suggests that the optimal region in space, where the acoustic forcing has the most substantial effect on the dynamics of the unstable global mode, is located near the upstream separation corner. This finding is consistent with the results of a study on a orthogonal deep cavity conducted by Boujo et al. (2018).

However, the substantial spatial discrepancy between the direct and adjoint fields demonstrates the non-normality of the linearised Navier-Stokes equations (Trefethen et al., 1993;

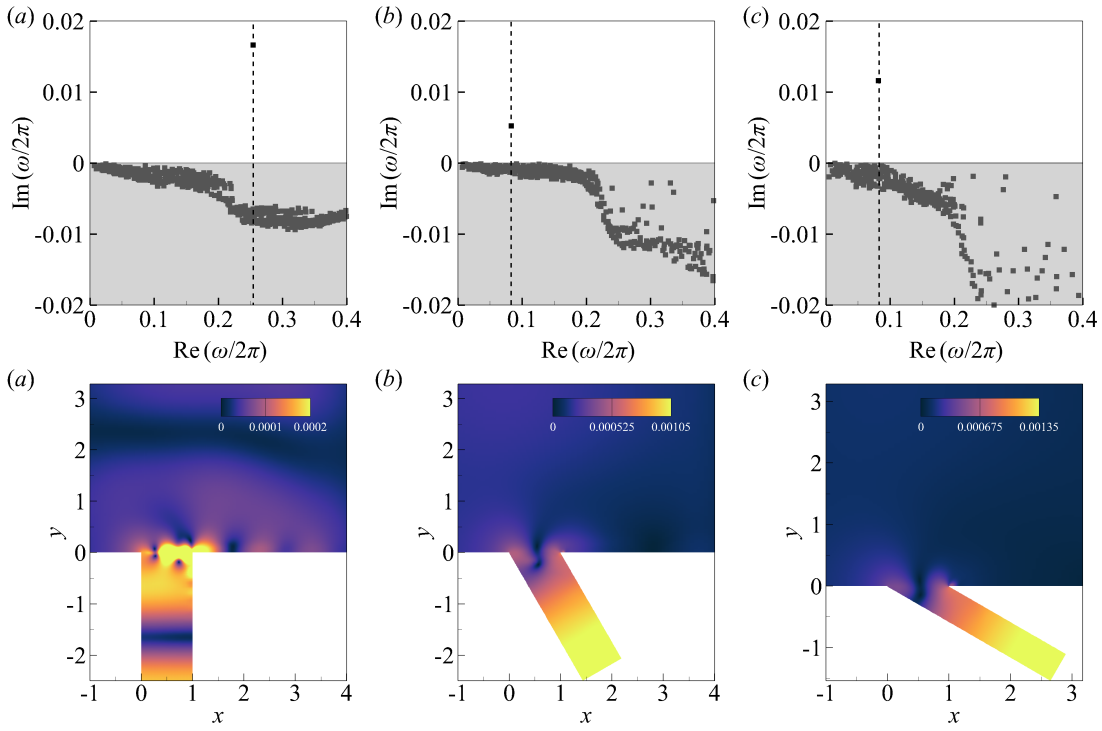

FIGURE 4.22: The top row of the scatter plots shows the eigenspectra of the linearised Navier-Stokes equations $L(\bar{Q};\beta = 0)$ for deep cavities with the inclinations: $\alpha = 90^\circ$ (*a*), $\alpha = 60^\circ$ (*b*), and $\alpha = 30^\circ$ (*c*), respectively. The vertical dashed line (- - -) indicates the tonal frequency observed in the LES. The bottom row of the contour plots presents the corresponding magnitude of the pressure disturbance, $|(\widehat{p})|$, which exhibits favourable agreement with those obtained directly from the LES. Refer to figure 4.5 for the comparison.

Chomaz et al., 1991; Giannetti and Luchini, 2007). Consequently, analysing the instability process that sustains the cavity oscillation based exclusively on stability and receptivity analyses is inadequate. To address this limitation, we employ the concept of a stability core, analogous to a "wake-maker", which examines the spatial region where a modification can induce the most significant change in the eigenvalue due to localised feedbacks (Giannetti and Luchini, 2007). Specifically, we investigate the structural sensitivity of the eigenvalue, whereby the changes in the frequency and growth rate of the eigenvalue of the global mode are determined by evaluating the real and imaginary parts of the sensitivity tensor denoted as S, as discussed in subsection 2.3.

Accordingly, the stability core is identified by analysing the imaginary component of the structural sensitivity tensor. The findings, illustrated in the top row of the contour plots in figure 4.24, show that the imaginary component of S by additional feedback associated with the streamwise momentum feedback is predominantly distributed near the upstream corner of the cavity opening (e.g., $x/L \approx 0.2$). This observation signifies that the application of positive streamwise momentum feedback in this critical region has the potential to effectively destabilise the flow (e.g., $\delta\omega_i > 0$). In contrast, the bottom row of the contour plots in figure 4.24 demonstrate that introducing positive vertical momentum feedback to instigate flow instabilities is less effective near the upstream corner of the cavity opening in all cavity cases. Therefore, the results suggest that the instabilities are most effectively destabilised by the positive feedback of a streamwise momentum at the localised region slightly downstream from the separation corner of the cavity. This region represents the area where the flow is most susceptible to hydrodynamic instabilities, providing a theoretical underpinning for previous successful efforts to suppress cavity oscillations using active or passive flow control near the upstream separation corner (III et al., 2008;

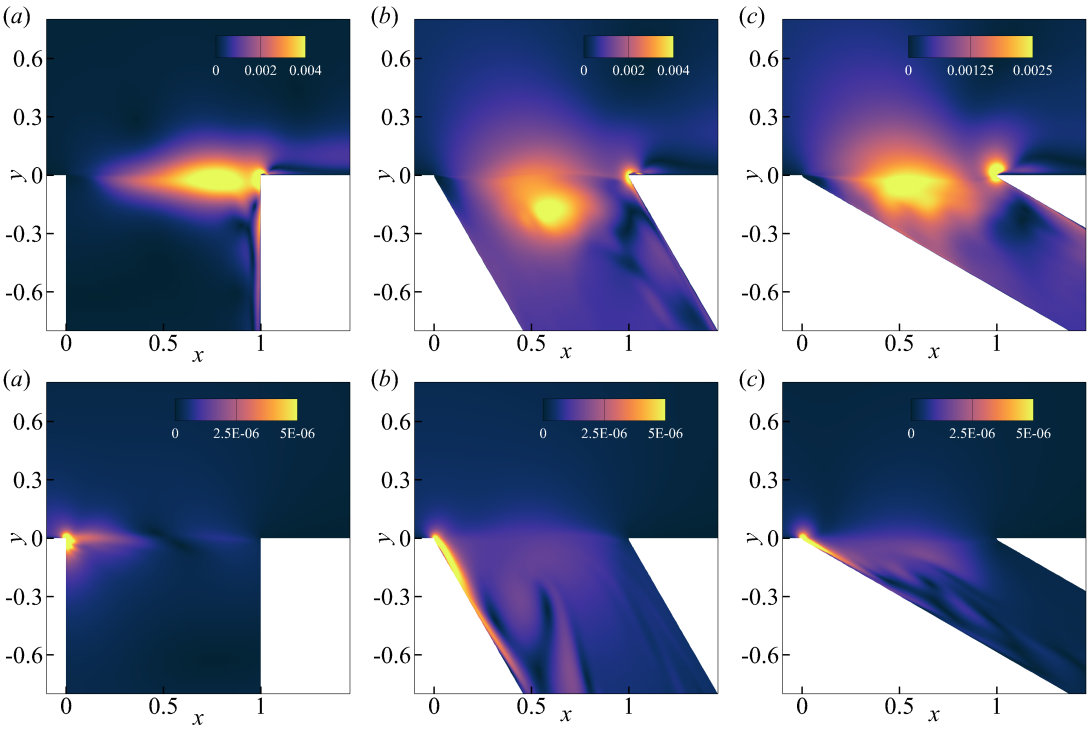

FIGURE 4.23: The top row of the contour plots shows the magnitude of the vertical momentum disturbance, $|(\widehat{\rho v})|$, while the bottom row of the contour plots presents the vertical momentum receptivity, $|(\widehat{\rho v})^{+}|$, of the most unstable mode for deep cavities with the inclinations: $\alpha = 90^{\circ}$ (a), $\alpha = 60^{\circ}$ (b), and $\alpha = 30^{\circ}$, respectively. The difference in spatial distribution between the direct (disturbance) and adjoint (receptivity) modes highlights the non-normality of the linearised Navier-Stokes equations.

Lawson and Barakos, 2011; Saddington et al., 2016).

However, an important question inspired by Rockwell and Naudascher (1978) remains unanswered: Can the unstable mode observed at specific Strouhal numbers in the current LES results (e.g., $St \approx 0.27$ in inclined cavities and $St \approx 0.85$ in the orthogonal cavity) be self-sustained solely through streamwise feedback via pseudo-sound (Ffowcs, 1969), without the presence of the acoustic resonance? To address this question, we conducted structural sensitivity analyses of pressure perturbations by overlapping the direct and adjoint pressure modes. Figure 4.25 reveals that the positive value of the imaginary component of S is predominantly distributed in the interior of the cavity, thereby indicating that the pressure feedback is primarily associated with the depthwise acoustic resonance. Therefore, this finding indicates that introducing a positive acoustic pressure feedback in the interior of the cavity is important in destabilising the unstable mode. Similarly, it can also be suggested that the unstable mode may be stabilised if the acoustic pressure feedback produced by the acoustic resonance is suppressed. This observation indirectly emphasises the critical role of depthwise acoustic resonance in destabilising the flow and enabling self-sustained oscillations in inclined and deep cavities. Therefore, it can be reasoned that the hydrodynamic feedback via pseudo-sound solely without the acoustic resonance may be insufficient to sustain the unstable cavity modes observed in this study.

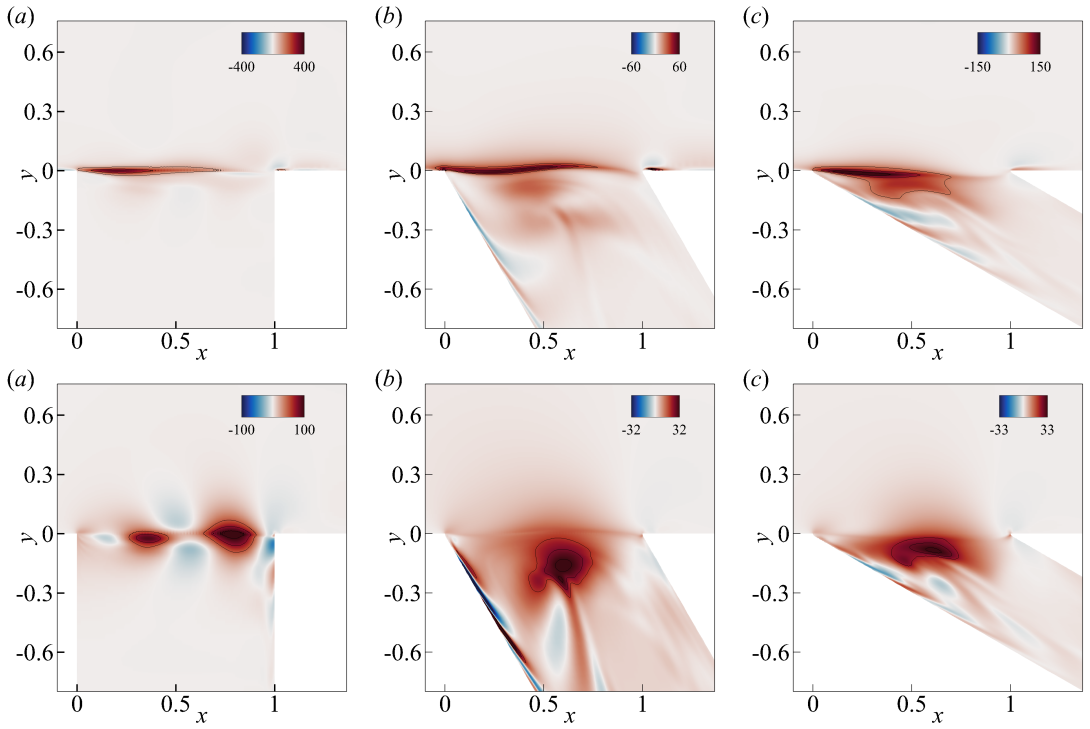

FIGURE 4.24: The imaginary part of the structural sensitivity, S identifies the region of the flow where introducing δL perturbation by additional positive feedback associated with the streamwise momentum feedback (first row of the contour plots), and the vertical momentum feedback (second row of the contour plots) has the greatest destabilising effect on the deep cavity flows with the inclinations: $\alpha = 90^\circ$ (a), $\alpha = 60^\circ$ (b), and $\alpha = 30^\circ$, respectively.

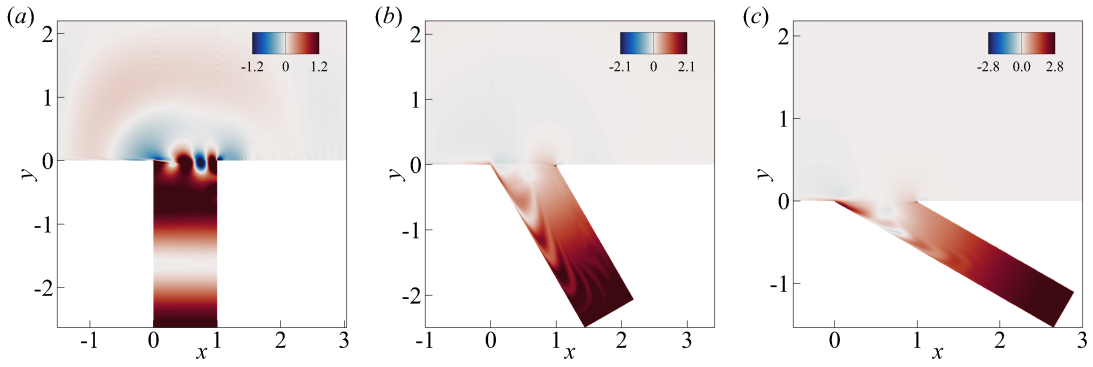

FIGURE 4.25: The imaginary part of the structural sensitivity, S identifies the region of the flow where introducing δL perturbation by additional positive pressure feedback has the greatest destabilising effect on the deep cavity flows with the inclinations: $\alpha = 90^\circ$ (a), $\alpha = 60^\circ$ (b), and $\alpha = 30^\circ$, respectively.

4.6 The critical oscillation at $St \approx 0.27$

The preceding discussions thus far have focused on elucidating the aeroacoustics of cavity oscillations, with limited attention given to the influence of incoming flow properties. To address this, we utilise the insights gained from receptivity and sensitivity analyses to quantify the impact of the acoustic forcing near the upstream corner of the cavity on the cavity oscillation frequency. In particular, the impact of the acoustic forcing is quantified by evaluating the peak acoustic particle displacement resulting from the depthwise acoustic resonance, as expressed by the following

equation:

$$\theta_a = \frac{|\hat{p}|}{\rho_\infty \omega a_\infty}. \tag{4.12}$$

Here, $|\hat{p}|$ represents the magnitude of the Fourier-transformed pressure fluctuations measured at the cavity bottom, while ω denotes the angular frequency corresponding to the tonal peak frequency observed in the pressure spectra of the LES results. According to Bagwell (2006), the occurrence of lock-in oscillation requires an acoustic particle displacement on the order of the momentum thickness. To investigate the validity of this criterion, we conduct a comparative study by contrasting our current LES results with prior experimental data on deep cavity flows.

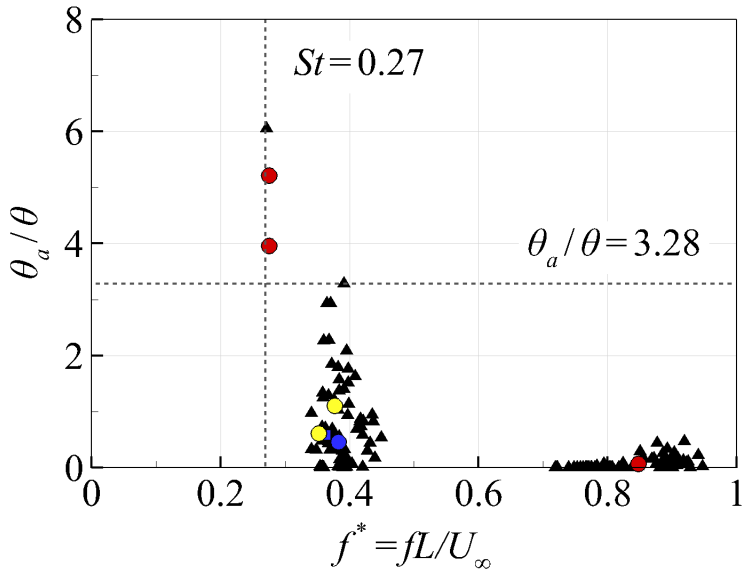

FIGURE 4.26: The scatter plot shows the ratio of acoustic particle displacement, denoted as θ_a, calculated using equation (4.12), to the momentum thickness of the approaching boundary layer, denoted as θ, measured at $x = -0.2$ at three distinct deep cavity flow regimes. The symbols in the plot represent data from various studies: Yang et al. (2009) (▲), Forestier et al. (2003) (■), Ho and Kim (2021b) (●), as well as results obtained from current LES at $M_\infty = 0.2$ (●) and $M_\infty = 0.3$ (●), respectively. The horizontal line in the scatter plot suggests the minimum value of θ_a/θ that is considered plausible for the intensified self-sustained resonance in deep cavity flows at the frequency of $St \approx 0.27$.

Figure 4.26 presents the acoustic particle displacement to momentum thickness ratio at the three distinct self-sustained resonance regimes. It is demonstrated that the self-sustained resonance in the current orthogonal cavity case at $M_\infty = 0.3$ closely resides at the third resonance regime (e.g. $St \approx 0.85$), belonging to the second hydrodynamic mode and is characterised by a relatively small acoustic particle displacement to momentum thickness ratio. Additionally, none of the oscillations in the inclined cavities at $M_\infty = 0.3$ was found to correspond to the second interval (e.g., $St \approx 0.385$), which, as reported by Ho and Kim (2021b), is closely associated with the first hydrodynamic mode. However, a prior investigation conducted on an orthogonal deep cavity configuration by Yang et al. (2009) revealed an oscillation with a frequency of approximately $St \approx 0.27$, remarkably coinciding with the frequency of the intensified self-sustained resonances observed in our present inclined cavity flows. Furthermore, it was observed that this self-sustained resonances necessitates an acoustic particle displacement to momentum thickness ratio surpassing a minimum threshold of $|\theta_a|/\theta > 3.28$. Based on these observations with existing experimental evidence, we suggest that the amplified flow-acoustic resonances in inclined cavities at $St \approx 0.27$ could be linked to a low-frequency extension of the first hydrodynamic

mode ($St \approx 0.385$) through the enhanced shear layer undulation when the acoustic particle displacement is comparable to the momentum thickness.

4.7 Summary

In conclusion, this chapter presented numerical investigations of flow-acoustic resonance in inclined and deep cavities using wall-resolved large-eddy simulations. The study focused on cavity configuration with an aspect ratio of $D/L = 2.632$ under three distinct inclination angles ($\alpha = 90^\circ$, 60°, and 30°) and at two different Mach numbers ($M_\infty = 0.2$ and 0.3), amounting to a total of six unique simulations. The initial finding of this study revealed distinct periodic oscillations in inclined cavities at both $M_\infty = 0.2$ and $M_\infty = 0.3$, providing strong evidence for the intrinsic self-sustaining nature exhibited by flows within inclined and deep cavities. However, despite their identical aspect ratio, the simulations demonstrated significant differences in the flow behaviour between inclined and orthogonal cavities.

Initially, the power spectra analysis of wall-pressure fluctuations at $M_\infty = 0.2$ revealed a primary resonance closely associated with the fundamental frequency ($St \approx 0.385$) for all inclination angles ($\alpha = 30^\circ$, 60°, and 90°). These frequencies are closely predicted by the Rossiter formula, indicative of the oscillations are excited by the first Rossiter mode. However, the self-sustained oscillations in inclined cavities at $M_\infty = 0.3$ exhibited an entirely unexpected behaviour. Firstly, the strongest peak frequency shifted to a lower value of $St = 0.27$ in the inclined cases ($\alpha = 30^\circ$ and 60°), contrasting with existing flow-acoustic resonance theories. Secondly, the inclined cavities at $M_\infty = 0.3$ demonstrated a significant increase in the peak amplitude by nearly 30dB stronger than the orthogonal cavity configuration. This observed amplitude even surpassed that seen under what was previously deemed the "optimal" condition for orthogonal cavity at $M_\infty = 0.2$. Herein, the primary objective of this paper is to delve into the physical mechanisms underlying these unexpected and pronounced acoustic responses from the inclined cavities at $M_\infty = 0.3$.

This study employed acoustic input-output and linear stability analyses to investigate the mechanism of noise generation in inclined cavity flows. The acoustic input-output analysis revealed that inclined cavities exhibited stronger acoustic responses due to the higher amplification rate of the least-damped depthwise acoustic mode and the reduced source-sink cancellation. Furthermore, the orthogonal cavity experienced an attenuated acoustic response primarily due to the significant source-sink cancellation occurring in the second hydrodynamic mode and the lower amplification rate resulting from the excitation of a heavily damped third acoustic mode. Furthermore, linear stability analyses identified the most unstable mode within the cavity systems, pinpointing the region slightly downstream of the separation corner as particularly susceptible to hydrodynamic instabilities. Sensitivity analysis demonstrated that streamwise momentum feedback effectively destabilised the flow near the upstream corner and confirmed the destabilising influence of least-damped acoustic modes on flow-acoustic resonances. Based on these observations with existing experimental evidence, we suggest that the amplified flow-acoustic resonances in inclined cavities at $St \approx 0.27$ could be linked to a low-frequency extension of the first hydrodynamic mode through the enhanced shear layer undulation when the acoustic particle displacement is comparable to the momentum thickness.

Chapter 5

Conclusions and future work

5.1 Summary of findings

The phenomenon of flow-acoustic resonance in inclined and deep cavity flows poses significant challenges in various engineering applications due to its efficient conversion of hydrodynamic and acoustic energy. This complex process involves the interaction of shear layers, which develop near the upstream corner as a result of flow separation, with acoustic waves supported by nearly-trapped acoustic modes within the deep cavities. As a result of this interplay, powerful acoustic waves radiate into the far field, and local hydrodynamic fluctuations induce dynamic loading, potentially leading to mechanical failures of nearby components. Therefore, minimizing the aerodynamic noise generated by this fluid-acoustic resonance is crucial, considering its detrimental implications. Previous research on deep cavity flows has offered invaluable experimental evidence, particularly regarding the lock-on phenomenon, a distinctive feature of deep cavity flows. Although numerous experimental and numerical studies have been conducted, a systematic study elucidating the noise generation and amplification mechanisms inherent in inclined and deep cavity turbulent flows is still lacking. To address this gap, this research offers a comprehensive quantitative analysis of the aeroacoustics of inclined and deep cavity flows. For this purpose, this research employed high-fidelity numerical simulations of the 3D compressible Navier-Stokes equations with realistic turbulent inflows generated using wall-resolved precursor channel simulations that compared favourably with existing DNS solutions. Through this approach, the study provided in-depth numerical investigations into the aeroacoustics of inclined and deep cavity flows.

In the first part of the thesis, a comprehensive understanding of the aerodynamic noise generation mechanism in a deep cavity with an aspect ratio of $D/L = 2.632$ at $Re_\infty = 174,594$, subjected to a turbulent boundary layer at a free stream velocity of $M_\infty = 0.2$, has been achieved. The study initially focused on pressure fluctuations around the cavity, which were decomposed between hydrodynamic and acoustic components using Doak's Momentum Potential Theory. The analysis of the decomposed acoustic pressure fluctuations unveiled momentary changes in the acoustic pressure within the cavity, synchronized with oscillations in the shear layer over the cavity opening. Subsequently, the research delved deeper into elucidating the intricate coupling mechanism between the separated shear layer oscillations near the upstream corner and the acoustic resonance within the cavity. A significant emphasis was placed on discerning the efficient fluid-acoustic coupling process, where it was observed that vertical velocity fluctuations were predominantly in-phase with the acoustic forcing near the upstream corner. Furthermore, the study uncovered the potential origins of higher harmonics, resulting from the 'modulated instability wave' influenced by the acoustic forcing at the fundamental frequency. Convection

speeds of coherent vortices were analyzed, leading to the proposal of a semi-empirical model designed to predict the critical free stream velocity required for strong fluid-acoustic coupling based on the inflow boundary-layer properties. In addition, the research delved into the influence of flow velocity on fluid-acoustic resonance in orthogonal and deep cavity. The investigation revealed that self-sustained oscillations exhibited distinct acoustic responses at different flow velocities, with the most pronounced amplification occurring at $M_\infty = 0.2$. The results also underscored the reduced amplification at speeds such as $M_\infty = 0.3$, attributable to the excitation of a highly-damped third depthwise acoustic mode. Conversely, in cases like $M_\infty = 0.1$ and $M_\infty = 0.3$, an attenuated acoustic response was explained by the predominant source-sink cancellation of the second hydrodynamic mode. Contrarily, the optimal acoustic response at $M_\infty = 0.2$ was facilitated by the maximum amplification of the least-damped depthwise fundamental acoustic mode and reduced source-sink cancellation of the first hydrodynamic mode. Lastly, this research highlighted the destabilizing impact of acoustic resonances in deep cavity flows, as evidenced by the biglobal linear stability analysis.

In the second part of the thesis, a series of numerical investigations were performed to explore flow-acoustic resonance within inclined and deep cavities. These investigations focused on inclined and deep cavities with a fixed aspect ratio of D/L = 2.632. The study considered three different inclination angles ($\alpha = 30^\circ$, 60°, and 90°) and two distinct Mach numbers ($M_\infty = 0.2$ and 0.3). The six unique deep cavity simulations showed pronounced periodic oscillation at both Mach numbers, highlighting the self-sustaining nature of flows in these cavity configurations. Despite identical aspect ratios, significant flow behaviour disparities between inclined and orthogonal cavities emerged. Initially, the power spectra of wall-pressure fluctuation at $M_\infty = 0.2$ showed a primary resonance at the fundamental frequency ($St \approx 0.385$) for all inclination angles, aligning with the Rossiter formula prediction. However, inclined cavities at $M_\infty = 0.3$ revealed totally unexpected behaviours. Firstly, the strongest peak frequency shifted to a lower value of $St = 0.27$ in the inclined cases ($\alpha = 30^\circ$ and 60°). More strikingly, the inclined cavities at $M_\infty = 0.3$ demonstrated a significant increase in the peak amplitude by nearly 30dB stronger than the orthogonal counterpart. This enhanced amplitude even surpassed that seen under what was previously deemed the "optimal" condition at $M_\infty = 0.2$. The study aimed to unravel the underlying physical mechanisms responsible for these pronounced acoustic responses. Utilizing acoustic input-output and linear stability analyses, it was revealed that inclined cavities exhibited enhanced acoustic responses due to higher amplification rates of least-damped depthwise acoustic modes and reduced source-sink cancellation of the hydrodynamic mode. In contrast, the orthogonal cavity displayed an attenuated responses, primarily due to significant source-sink cancellation of the second hydrodynamic mode and lower amplification rate from exciting heavily damped third acoustic modes. Subsequently, the analysis identified the region downstream of the separation corner as particularly susceptible to hydrodynamic instabilities. Sensitivity analysis affirmed the destabilizing impact of least-damped acoustic modes on flow-acoustic resonances and the destabilization of flows near upstream corners through streamwise momentum feedback. Drawing upon these observations and existing experimental evidence, we suggest that the amplified flow-acoustic resonances in inclined cavities at $St \approx 0.27$ are linked to a low-frequency extension of the first hydrodynamic mode through the enhanced shear layer undulation when the acoustic particle displacement is comparable to the momentum thickness.

5.2 Future work arising from this study

This work offers a multitude of promising avenues for further exploration. The essence of this thesis lies in investigating the fundamental physics of the aeroacoustics of deep cavity flows through simplified rectangular deep and inclined cavity configurations. In particular, a comprehensive understanding of the underlying noise generation and amplification mechanisms in simplified orthogonal and inclined deep cavity configurations at low subsonic flows is provided in this thesis. However, it is essential to progress towards more realistic geometries that accurately emulate practical situations. To this end, pursuing realistic configurations includes examining deep cylindrical cavity geometries with varying inclinations at transonic flow regimes. Furthermore, the work presented here considers a periodic boundary condition in the spanwise direction. It may be interesting to incorporate a viscous nonslip wall boundary condition in the spanwise direction to understand better the spanwise wall effects on the formation and the coherence of the vortical structures in deep cavity flows. Finally, the work presented here highlighted the importance of the fluid-acoustic coupling process in the inclined and orthogonal deep cavity flows. Therefore, future progress on active or passive flow control techniques with special attention to the upstream corner and cavity floor to suppress coherent vortex formation before the separation of the shear layer will be another promising avenue for further exploration.

References

K. K. Ahuja and J. Mendoza. Effects of cavity dimensions, boundary layer, and temperature on cavity noise with emphasis on benchmark data to validate computational aeroacoustic codes, Final Report Contract NAS1-19061, Task 13. NASA Contractor Report. 1995.

A. A. Aleksentsev, A. N. Sazhenkov, and S. V. Sukhinin. Acoustic resonance phenomena in air bleed channels in aviation engines. *Journal of Applied Mechanics and Technical Physics*, 57 (6):971–978, 2016.

K. Aly and S. Ziada. Effect of mean flow on the trapped modes of internal cavities. *Journal of Fluids and Structures*, 33:70–84, August 2012.

D. Arthurs and S. Ziada. Flow-excited acoustic resonances of coaxial side-branches in an annular duct. *Journal of Fluids and Structures*, 25(1):42–59, 2009.

N. Arya and A. De. Effect of vortex and entropy sources in sound generation for compressible cavity flow. *Physics of Fluids*, 33(4):046107, April 2021.

T. G. Bagwell. CFD Simulation of Flow Tones From Grazing Flow Past a Deep Cavity. Noise Control and Acoustics:105–114, 11 2006.

P. J. W. Block. Noise response of cavities of varying dimensions at subsonic speeds, NASA-TN-D-8351, NASA, Washington, D.C. 1976.

E. Boujo, M. Bauerheim, and N. Noiray. Saturation of a turbulent mixing layer over a cavity: response to harmonic forcing around mean flows. *Journal of Fluid Mechanics*, 853:386–418, August 2018.

C. Bourquard, A. Faure-Beaulieu, and N. Noiray. Whistling of deep cavities subject to turbulent grazing flow: intermittently unstable aeroacoustic feedback. *Journal of Fluid Mechanics*, 909:A19, 2021.

P. Bradshaw. A note on poisson's equation for pressure in a turbulent flow. *Physics of Fluids*, 24(4):777, 1981.

R. Bravo, S. Ziada, and M. Dokainish. Aeroacoustic response of an annular duct with coaxial closed side branches. In *11th AIAA/CEAS Aeroacoustics Conference*, page 3019, 2005.

G. A. Bres and T. Colonius. Three-dimensional instabilities in compressible flow over open cavities. *Journal of Fluid Mechanics*, 599:309–339, 2008.

J. C. Bruggeman. *Flow induced pulsations in pipe systems*. PhD thesis, Department of Applied Physics, 1987.

J. C. Bruggeman, A. Hirschberg, M. E. H. van Dongen, A. P. J. Wijnands, and J. Gorter. Flow induced pulsations in gas transport systems: Analysis of the influence of closed side branches. *Journal of Fluids Engineering*, 111(4):484–491, December 1989.

J. C. Bruggeman, A. Hirschberg, M. E. H. Van Dongen, A. P. J. Wijnands, and J. Gorter. Self-sustained aero-acoustic pulsations in gas transport systems: experimental study of the influence of closed side branches. *Journal of sound and vibration*, 150(3):371–393, 1991.

I. P. Castro, J. W. Kim, A. Stroh, and H. C. Lim. Channel flow with large longitudinal ribs. *Journal of Fluid Mechanics*, 915:A92, 2021.

Z. Chen and N.A. Adams. Mode interactions of a high-subsonic deep cavity. *Physics of Fluids*, 29(5), 2017.

J. M. Chomaz. Global instabilities in spatially developing flows: non-normality and nonlinearity. *Annu. Rev. Fluid Mech.*, 37:357–392, 2005.

J. M Chomaz, P. Huerre, and L. G. Redekopp. A frequency selection criterion in spatially developing flows. *Studies in applied mathematics*, 84(2):119–144, 1991.

V. Citro, F. Giannetti, L. Brandt, and P. Luchini. Linear three-dimensional global and asymptotic stability analysis of incompressible open cavity flow. *Journal of Fluid Mechanics*, 768:113–140, 2015.

J. T. Coffman and M. D. Bernstein. Failure of safety valves due to flow-induced vibration. *Journal of Pressure Vessel Technology*, 102(1):112–118, February 1980.

N. Curle. The influence of solid boundaries upon aerodynamics sound. *Proc. R. Soc. Lond. A*, 231:505–514, 1955.

X. Dai, X.D. Jin, and X.F. Sun. Flow-excited acoustic resonance of a helmholtz resonator: Discrete vortex model compared to experiments. *Physics of Fluids*, 27(5):057102, May 2015.

E. Degregori and J. W. Kim. Mitigation of transonic shock buffet on a supercritical airfoil through wavy leading edges. *Physics of Fluids*, 33(2), 2021.

Department of Transport. UK aviation forecasts. tech. rep. 2013.

S. Dequand, S. J. Hulshoff, and A. Hirschberg. Self-sustained oscillations in a closed side branch system. *Journal of Sound and Vibration*, 265(2):359–386, aug 2003.

P. E. Doak. Momentum potential theory of energy flux carried by momentum fluctuations. *Journal of Sound and Vibration*, 131(1):67–90, 1989. ISSN 0022-460X.

Y. Duan, W. Koch, C. M. Linton, and M. McIVER. Complex resonances and trapped modes in ducted domains. *Journal of Fluid Mechanics*, 571:119–147, 2007.

L. F. East. Aerodynamically induced resonance in rectangular cavities. *Journal of Sound and Vibration*, 3(3):277–287, May 1966.

S. A. Elder. Forced oscillations of a separated shear layer with application to cavity flow-tone effects. *The Journal of the Acoustical Society of America*, 67(3):774–781, 1980.

D. Erickson and W. Durgin. Tone generation by flow past deep wall cavities. In *25th AIAA Aerospace Sciences Meeting*. American Institute of Aeronautics and Astronautics, March 1987.

D. Erickson, W. Durgin, C. F. Maguire III, and M. J. Moeller. Shear layer coupling with side-branch resonators. In *ASME Winter Annual Meeting: Anaheim, CA*, page 43, 1986.

R. Ewert and W. Schröder. Acoustic perturbation equations based on flow decomposition via source filtering. *Journal of Computational Physics*, 188(2):365–398, July 2003.

J. E. Williams Ffowcs. Hydrodynamic noise. *Annual Review of Fluid Mechanics*, 1(1):197–222, 1969.

N. Forestier, L. Jacquin, and P. Geffroy. The mixing layer over a deep cavity at high-subsonic speed. *Journal of Fluid Mechanics*, 475:101–145, January 2003.

D. Galbally, G. García, J. Hernando, J. de Dios Sánchez, and M. Barral. Analysis of pressure oscillations and safety relief valve vibrations in the main steam system of a boiling water reactor. *Nuclear Engineering and Design*, 293:258–271, 2015.

M. B. R. Gelot and J. W. Kim. Effect of serrated trailing edges on aerofoil tonal noise. *Journal of Fluid Mechanics*, 904:A30, 2020.

F. Giannetti and P. Luchini. Structural sensitivity of the first instability of the cylinder wake. *Journal of Fluid Mechanics*, 581:167–197, May 2007.

X. Gloerfelt. Cavity noise. *VKI lecture series*, 3, 2009.

M. E. Goldstein. *Aeroacoustics*. McGraw-Hill, 1976.

H. R. Graf and W. W. Durgin. Measurement of the nonsteady flow field in the opening of a resonating cavity excited by grazing flow. *Journal of Fluids and Structures*, 7(4):387–400, May 1993.

M. Hanna and A. Mohany. Aeroacoustics and shear layer characteristics of confined cavities subject to low mach number flow. *Journal of Fluids and Structures*, 121:103949, 2023.

M. E. Hassan, L. Keirsbulck, and L. Labraga. Aero-acoustic oscillations inside large deep cavities at low sub-sonic speeds. *Journal of Fluids Engineering*, 131(1), 2007.

S. Hein and W. Koch. Acoustic resonances and trapped modes in pipes and tunnels. *Journal of Fluid Mechanics*, 605:401–428, may 2008.

C. M. Ho and L. S. Huang. Subharmonics and vortex merging in mixing layers. *Journal of Fluid Mechanics*, 119:443–473, 1982.

C. M. Ho and N. S. Nosseir. Dynamics of an impinging jet. part 1. the feedback phenomenon. *Journal of Fluid Mechanics*, 105(-1):119, April 1981.

Y. W. Ho and J. W. Kim. Flow-acoustic resonance in inclined and deep cavities. *Under review in Physical Review Fluids*.

Y. W. Ho and J. W. Kim. A wall-resolved large-eddy simulation of deep cavity flow in acoustic resonance. *Journal of Fluid Mechanics*, 917, April 2021a.

Y. W. Ho and J. W. Kim. A wall-resolved large-eddy simulation of deep cavity flow in acoustic resonance. *Journal of Fluid Mechanics*, 917, 2021b.

Y. W. Ho and J. W. Kim. Wall-resolved large-eddy simulations of inclined deep cavity flows in acoustic resonance. In *28th AIAA/CEAS Aeroacoustics Conference*. American Institute of Aeronautics and Astronautics, June 2022.

M. S. Howe. *Acoustics of fluid-structure interactions*. Cambridge University Press, 1998.

M. S. Howe. *Theory of vortex sound*. Cambridge University Press, 2002.

M. S. Howe. *Theory of Vortex Sound*. Cambridge Texts in Applied Mathematics. Cambridge University Press, 2003.

L. N. Cattafesta III, S. Garg, M. Choudhari, and F. Li. Active control of flow-induced cavity resonance. In *28th Fluid Dynamics Conference*. American Institute of Aeronautics and Astronautics, June 1997.

L. N Cattafesta III, Q. Song, D. R. Williams, C. W. Rowley, and F. S. Alvi. Active control of flow-induced cavity oscillations. *Progress in Aerospace Sciences*, 44(7-8):479–502, 2008.

K. Karamcheti. Acoustic radiation from two-dimensional rectangular cut-outs in aerodynamic surfaces. *NACA TN*, 3487, 1955.

J. W. Kim. Optimised boundary compact finite difference schemes for computational aeroacoustics. *J. Comput. Phys.*, 225:995–1019, 2007.

J. W. Kim. Quasi-disjoint pentadiagonal matrix systems for the parallelization of compact finite-difference schemes and filters. *J. Comput. Phys.*, 241:168–194, 2013.

J. W. Kim and D.J. Lee. Generalized characteristic boundary conditions for computational aeroacoustics. *AIAA J.*, 38(11):2040–2049, 2000.

J. W. Kim and D.J. Lee. Generalized characteristic boundary conditions for computational aeroacoustics, part 2. *AIAA J.*, 42(1):47–55, 2004.

J. W. Kim and P.J. Morris. Computation of subsonic inviscid flow past a cone using high-order schemes. *AIAA J.*, 40(10):1961–1968, 2002.

J. W. Kim, A.S.H. Lau, and N.D. Sandham. CAA boundary conditions for airfoil noise due to high-frequency gusts. *Proc. Eng.*, 6:244–253, 2010a.

J. W. Kim, A.S.H. Lau, and N.D. Sandham. Proposed boundary conditions for gust-airfoil interaction noise. *AIAA J.*, 48(11):2705–2709, 2010b.

C. Knisely and D. Rockwell. Self-sustained low-frequency components in an impinging shear layer. *Journal of Fluid Mechanics*, 116:157–186, March 1982.

W. Koch. Acoustic resonances in rectangular open cavities. *AIAA Journal*, 43(11):2342–2349, November 2005.

P. C. Kriesels, M. C. A. M. Peters, A. Hirschberg, A. P. J. Wijnands, A. Iafrati, G. Riccardi, R. Piva, and J. C. Bruggeman. High amplitude vortex-induced pulsations in a gas transport system. *Journal of Sound and Vibration*, 184(2):343–368, 1995.

L. Larchevêque, P. Sagaut, I. Mary, O. Labbé, and P. Comte. Large-eddy simulation of a compressible flow past a deep cavity. *Physics of Fluids*, 15(1):193–210, January 2003.

S. J. Lawson and G. N. Barakos. Review of numerical simulations for high-speed, turbulent cavity flows. *Progress in Aerospace Sciences*, 47(3):186–216, April 2011.

M. K. Lee and R. D. Moser. Direct numerical simulation of turbulent channel flow up to $Re_\phi \approx$ 5200. *Journal of Fluid Mechanics*, page 395–415, 2015.

M. J. Lighthill. On sound generated aerodynamically i. general theory. *Proceedings of the Royal Society of London. Series A. Mathematical and Physical Sciences*, 211(1107):564–587, 1952.

Q. Liu, F. Gómez, and V. Theofilis. Linear instability analysis of low-incompressible flow over a long rectangular finite-span open cavity. *Journal of Fluid Mechanics*, 799:R2, 2016.

Q. Liu, Y. Sun, C.A Yeh, L.S Ukeiley, L.N Cattafesta, and K. Taira. Unsteady control of supersonic turbulent cavity flow based on resolvent analysis. *Journal of Fluid Mechanics*, 925, August 2021.

A. Lozano-Durán and J. Jiménez. Effect of the computational domain on direct simulations of turbulent channels up to $Re_\tau = 4200$. *Physics of Fluids*, 26, January 2014.

P. Luchini and A. Bottaro. Adjoint equations in stability analysis. *Annual Review of Fluid Mechanics*, 46(1):493–517, January 2014.

R. L. Ma, P. E. Slaboch, and S. C. Morris. Fluid mechanics of the flow-excited helmholtz resonator. *Journal of Fluid Mechanics*, 623:1, 2009.

S. F. McGrath and D. J. Olinger. Control of pressure oscillations in deep cavities excited by grazing flow. *Journal of Aircraft*, 33(1):29–36, January 1996.

B. J. McKeon and A. S. Sharma. A critical-layer framework for turbulent pipe flow. *Journal of Fluid Mechanics*, 658:336–382, 2010.

F. Meseguer-Garrido, J. De Vicente, E. Valero, and V. Theofilis. On linear instability mechanisms in incompressible open cavity flow. *Journal of Fluid Mechanics*, 752:219–236, 2014.

A. Michalke. The instability of free shear layers. *Progress in Aerospace Sciences*, 12:213–216, January 1972.

S. C. Morris. Shear-layer instabilities: particle image velocimetry measurements and implications for acoustics. *Annual Review of Fluid Mechanics*, 43:529–550, 2011.

T. Y. Na and Y. P. Lu. Turbulent flow development characteristics in channel inlets. *Applied Scientific Research*, 27(1):425–439, 1973.

A. M. Naguib and M. M. Koochesfahani. On wall-pressure sources associated with the unsteady separation in a vortex-ring/wall interaction. *Physics of Fluids*, 16(7):2613–2622, July 2004.

P. A. Nelson, N. A. Halliwell, and P. E. Doak. Fluid dynamics of a flow excited resonance, part ii: Flow acoustic interaction. *Journal of sound and vibration*, 91(3):375–402, 1983.

P Oshkai, M Geveci, D Rockwell, and M Pollack. Imaging of acoustically coupled oscillations due to flow past a shallow cavity: effect of cavity length scale. *Journal of fluids and structures*, 20(2):277–308, 2005.

P. Oshkai, T. Yan, A. Velikorodny, and S. VanCaeseele. Acoustic power calculation in deep cavity flows: A semiempirical approach. *Journal of Fluids Engineering*, 130(5), May 2008.

C. Paruchuri. *Aerofoil geometry effects on turbulence interaction noise*. PhD thesis, University of Southampton, April 2017.

T. Pedergnana, C. Bourquard, A. Faure-Beaulieu, and N. Noiray. Modeling the nonlinear aeroacoustic response of a harmonically forced side branch aperture under turbulent grazing flow. *Physical Review Fluids*, 6(2):023903, 2021.

R. Pérez-Torró and J. W. Kim. A large-eddy simulation on a deep-stalled aerofoil with a wavy leading edge. *Journal of Fluid Mechanics*, 813:23–52, January 2017.

C. Perrot-Minot, E. Mignot, R. Perkins, D. Lopez, and N. Riviere. Vortex shedding frequency in open-channel lateral cavity. *Journal of Fluid Mechanics*, 892, April 2020.

M. C. A. M. Peters. *Aeroacoustic sources in internal flows*. Eindhoven University of Technology, 1993a.

M. C. A. M. Peters. *Aeroacoustic sources in internal flows*. Eindhoven University of Technology Eindhoven, Netherlands, 1993b.

H. E. Plumblee, J. S. Gibson, and L. W. Lassiter. A theoretical and experimental investigation of the acoustic response of cavities in an aerodynamic flow. Technical report, Lockheed Aircraft Corp Marietta GA, 1962.

A. R. Proenca. *Aeroacoustics of isolated and installed jets under static and in-flight conditions*. PhD thesis, University of Southampton, March 2018.

S. W. Rienstra. Fundamentals of duct acoustics. *Von Karman Institute Lecture Notes*, 2015.

D. Rockwell. Oscillations of impinging shear layers. *AIAA Journal*, 21(5):645–664, May 1983.

D. Rockwell and E. Naudascher. Review—self-sustaining oscillations of flow past cavities. *Journal of Fluids Engineering*, 100(2):152–165, June 1978.

D. Rockwell and E. Naudascher. Self-sustained oscillations of impinging free shear layers. *Annual Review of Fluid Mechanics*, 11(1):67–94, January 1979.

J.E. Rossiter. Wind tunnel experiments on the flow over rectangular cavities at subsonic and transonic speeds. Technical report, Ministry of Aviation; Royal Aircraft Establishment; RAE Farnborough, 1964.

C. W. Rowley and D. R. Williams. Dynamics and control of high-reynolds-number flow over open cavities. *Annu. Rev. Fluid Mech.*, 38:251–276, 2006.

C. W. Rowley, T. Colonius, and A. J. Basu. On self-sustained oscillations in two-dimensional compressible flow over rectangular cavities. *Journal of Fluid Mechanics*, 455:315–346, 2002.

A. Saddington, V. Thangamani, and K. Knowles. Comparison of passive flow control methods for a cavity in transonic flow. *Journal of Aircraft*, 53(5):1439–1447, 2016.

E. Salt, S. Mohamed, D. Arthurs, and S. Ziada. Aeroacoustic sources generated by flow–sound interaction in a t-junction. *Journal of Fluids and Structures*, 51:116–131, 2014.

P. Sampath and K. P. Sinhamahapatra. Numerical analysis of characteristic features of shallow and deep cavity in supersonic flow. *International Journal of Computational Fluid Dynamics*, 30(3):231–255, 2016.

P. J. Schmid. Nonmodal stability theory. *Annual Review of Fluid Mechanics*, 39(1):129–162, January 2007.

P. J. Schmid and L. Brandt. Analysis of Fluid Systems: Stability, Receptivity, Sensitivity: Lecture notes from the FLOW-NORDITA Summer School on Advanced Instability Methods for Complex Flows, Stockholm, Sweden, 2013. *Applied Mechanics Reviews*, 66(2), 03 2014. ISSN 0003-6900.

D. B. Spalding. A single formula for the "law of the wall". *Journal of Applied Mechanics*, 28 (3):455–458, September 1961.

G. W. Stewart. A krylov–schur algorithm for large eigenproblems. *SIAM Journal on Matrix Analysis and Applications*, 23(3):601–614, January 2002.

Y. Sun, K. Taira, L.N. Cattafesta, and L.S. Ukeiley. Biglobal instabilities of compressible open-cavity flows. *Journal of Fluid Mechanics*, 826:270–301, 2017.

C. K. W. Tam. Excitation of instability waves in a two-dimensional shear layer by sound. *Journal of Fluid Mechanics*, 89(2):357–371, 1978.

Y. P. Tang and D. Rockwell. Instantaneous pressure fields at a corner associated with vortex impingement. *Journal of Fluid Mechanics*, 126:187–204, January 1983.

V Theofilis. Globally unstable basic flows in open cavities. In *6th Aeroacoustics Conference and Exhibit*, page 1965, 2000.

V. Theofilis. Global linear instability. *Annual Review of Fluid Mechanics*, 43(1):319–352, January 2011.

K. W. Thompson. Time dependent boundary conditions for hyperbolic systems. *Journal of Computational Physics*, 68(1):1–24, January 1987.

K. W. Thompson. Time-dependent boundary conditions for hyperbolic systems, II. *Journal of Computational Physics*, 89(2):439–461, August 1990.

B. Thornber and D. Drikakis. Implicit large eddy simulation of a deep cavity using high-resolution methods. In *46th AIAA Aerospace Sciences Meeting and Exhibit*. American Institute of Aeronautics and Astronautics, January 2008.

E. Tinar and D. Rockwell. Generation of locked-on flow tones: Effect of damping. *Journal of Fluids and Structures*, 44:129–144, January 2014a.

E. Tinar and D. Rockwell. Generation of locked-on flow tones: Effect of damping. *Journal of Fluids and Structures*, 44:129–144, 2014b.

D. Tonon, A. Hirschberg, and J. Golliard S. Ziada. Aeroacoustics of pipe systems with closed branches. *International Journal of Aeroacoustics*, 10(2-3):201–275, 2011.

L. N. Trefethen, A. E. Trefethen, S. C. Reddy, and T. A. Driscoll. Hydrodynamic stability without eigenvalues. *Science*, 261(5121):578–584, 1993.

B. A. Tuna and D. Rockwell. Self-sustained oscillations of shallow flow past sequential cavities. *Journal of Fluid Mechanics*, 758:655–685, October 2014.

J. M. Turner. *Aerodynamic noise from undulated leading edge aerofoils*. PhD thesis, University of Southampton, March 2019.

J. M. Turner and J. W. Kim. Aeroacoustic source mechanisms of a wavy leading edge undergoing vortical disturbances. *J. Fluid Mech.*, 811:582–611, 2017.

J. M. Turner and J. W. Kim. On the universal trends in the noise reduction due to wavy leading edges in aerofoil–vortex interaction. *Journal of Fluid Mechanics*, 871:186–211, May 2019.

J. M. Turner and J. W. Kim. Effect of spanwise domain size on direct numerical simulations of airfoil noise during flow separation and stall. *Physics of Fluids*, 32(6), 2020.

S. Unnikrishnan and D. V. Gaitonde. Acoustic, hydrodynamic and thermal modes in a supersonic cold jet. *Journal of Fluid Mechanics*, 800:387–432, 2016.

S. Unnikrishnan and D. V. Gaitonde. A pressure decomposition framework for aeroacoustic analysis of turbulent jets. *European Journal of Mechanics - B/Fluids*, 81:41–61, 2020. ISSN 0997-7546.

A. Velikorodny, T. Yan, and P. Oshkai. Quantitative imaging of acoustically coupled flows over symmetrically located side branches. *Experiments in fluids*, 48:245–263, 2010.

P. Wang, H. Ma, Y. Deng, and Y. Liu. Influence of vortex-excited acoustic resonance on flow dynamics in channel with coaxial side-branches. *Physics of Fluids*, 30(9), 2018.

F. M. White. Viscous fluid flow 2nd edition mcgraw-hill. *New York*, 1991.

J. E. Ffowcs Williams and D. L. Hawkings. Sound generation by turbulence and surfaces in arbitrary motion. *Philosophical Transactions of the Royal Society of London. Series A, Mathematical and Physical Sciences*, 264(1151):321–342, 1969.

World Health Organization. Burden of disease from environmental noise: Quantification of healthy life years lost in europe. https://www.euro.who.int/__data/assets/pdf_file/0008/136466/e94888.pdf, 2011. [Accessed 31-Aug-2022].

S. Yamouni, D. Sipp, and L. Jacquin. Interaction between feedback aeroacoustic and acoustic resonance mechanisms in a cavity flow: a global stability analysis. *Journal of Fluid Mechanics*, 717:134–165, 2013a.

S. Yamouni, D. Sipp, and L. Jacquin. Interaction between feedback aeroacoustic and acoustic resonance mechanisms in a cavity flow: a global stability analysis. *Journal of Fluid Mechanics*, 717:134–165, 2013b.

Y. Yang, D. Rockwell, K.L.F. Cody, and M. Pollack. Generation of tones due to flow past a deep cavity: Effect of streamwise length. *Journal of Fluids and Structures*, 25(2):364–388, February 2009.

S. Ziada. A flow visualization study of flow-acoustic coupling at the mouth of a resonant side-branch. *Journal of Fluids and Structures*, 8(4):391–416, 1994.

S. Ziada. Flow-excited acoustic resonance in industry. *Journal of Pressure Vessel Technology*, 132(1), 2010.

S. Ziada and P. Lafon. Flow-excited acoustic resonance excitation mechanism, design guidelines, and counter measures. *Applied Mechanics Reviews*, 66(1), 2014.

S. Ziada and S. Shine. Strouhal numbers of flow-excited acoustic resonance of closed side branches. *Journal of Fluids and Structures*, 13(1):127–142, 1999a. ISSN 0889-9746.

S. Ziada and S. Shine. Strouhal numbers of flow-excited acoustic resonance of closed side branches. *Journal of fluids and structures*, 13(1):127–142, 1999b.

S. Ziada, A. Oengören, and A. Vogel. Acoustic resonance in the inlet scroll of a turbocompressor. *Journal of Fluids and structures*, 16(3):361–373, 2002.